HYDRODYNAMICS ANALYSIS OF AIR SUPPORTED VESSELS

NAN XIE

Thesis submitted to the Faculty of Engineering
University of Strathclyde, for the Degree of Doctor of Philosophy

Department of Naval Architecture and Marine Engineering
University of Strathclyde

January 2012

Declaration

I hereby declare that this dissertation and all material contained here in is a record of work carried out in the Department of Naval Architecture and Marine Engineering of University of Strathclyde during the period from June 2002 to March 2011. The dissertation is original in content except where otherwise indicated.

January 2012

Nan Xie

Summary

In recent years, the Air Supported Vessels (ASVs) has received some interest due to increasing oil prices and the stricter regulations on emissions. The ASVs have the potential of reducing fuel consumption with less drag by adopting air cavity underneath its hull surface. Research so far has been mainly focused on the mechanism and effectiveness of the air cavity for drag reduction, i.e., the resistance in calm water condition. Other hydrodynamic performances of the ASVs are rarely studied.

In this thesis, it is attempted to address some of the other hydrodynamic problems for the ASV, namely, wash wave field, motion response in waves and the stability. New mathematical models have been proposed to tackle these problems. The models cover the steady flow, frequency domain analysis (seakeeping) and time domain analysis (the dynamic stability). Emphases are placed on numerical calculation of the flow field generated by the excess pressure inside the cavity.

Although the analytic expressions of the potential flow field by a pressure patch moving on the free surface are well known, the numerical calculations remain challenging. The singularities and highly oscillatory behaviour of the velocity potentials and the free surface elevations will cause numerical instability problem. In this study, new numerical schemes are proposed and the irregularities have been successfully removed.

A number of case studies have been carried out to verify the proposed mathematical models and numerical methods. Satisfactory agreements have been found as far as there are other computations or measurements for comparison; or reasonable results are obtained. It is expected that the mathematical model, the numerical methods and tools established in the present study can be a supplementary means for developing the ASV at both design and operational stages.

Acknowledgements

I would like to express sincerely my gratitude to Professor Dracos Vassalos for offering me the opportunity to study under his supervision for this degree. His guidance, insight, version and critical thinking in the topics treated in this work have been invaluable. This study would have not been completed without his continuous support.

My thanks are extended to many colleagues in the Department for their friendship, advice and assistance. Dr. Andrzej Jasionowski has been kind to provide access of PROTEUS for calculation of the hydrodynamic coefficients. I am grateful to Prof. Shan Huang, Prof. Osman Turan, Dr. Georgios Mermiris, who have been very kind to review draft of the thesis and offered their valuable comments. Mrs. Thelma Will has been very helpful with the administrative details of the preparation and submission of my thesis. I am truly thankful for her support.

Thanks to Dr. Xiaoming Cheng of Nobel Denton Ltd, U.K., and Professor Lawrence Doctors of University of South Wales, Australia, for their valuable discussions on study of the 3D planing hydrodynamic problem.

I am indebted to Professor Apostolos Papanikolaou of NTUA and Dr. Phillip Sayer of University of Strathclyde for serving in the panel of my viva.

Finally, I would like to thank my wife, Huihui, and son, Cheng, for their company, love and support during the course of this study.

Publication List

The following papers have been published during the present Ph. D. study, and they form part of this thesis:

Xie N, Jasionowski, A., Vassalos, D., 2004, A numerical method for predicting wash waves of SES, Journal of Ship Mechanics, 8(6), pp31-44.

Xie, N., Jasionowski, A., Vassalos, D., 2004, Evaluation of wash waves of the air lifted catamaran, Proceedings of the 9th International Conference on Practical Design of Ships and Other Floating Structures, Germany, Vol. 2, pp672-678.

Xie, N., Vassalos, D., Jasionowski, A., 2005, A study of hydrodynamics of three dimensional planing surface, Ocean Engineering, 32(13), pp1539-1555.

Xie, N., Vassalos, D., Jasionowski, A., Sayer, P., 2008, A seakeeping analysis method for the air lifted vessel, Ocean Engineering, 35(14-15), pp1512-1520.

Vassalos, D., Xie, N., Jasionowski, A., Konovessis, D., 2008, Stability and safety analysis of the air lifted catamaran, Journal of Ships and Offshore Structures, 3(2), pp91-98.

Xie, N., Vassalos, D., 2011, A study of hydrodynamics of planing flat catamaran and prismatic hulls, International Shipbuilding Progress, 58 (2-3), pp115-139.

List of Contents

Nomenclature

a	length of a rectangular pressure patch
A	parameter of wave spectra
A_c	cushion area of a demi-hull
A_L	escape area at stern of cushion
$A_{i,j}$	$i, j = 1, 2, \ldots, 6$, added mass of the vessel
A_{L0}	outflow opening area at equilibrium condition
A_{Lw}	cushion opening area due to incident wave
b	beam of a rectangular pressure patch
B	parameter of wave spectra
B_c	cushion beam
B_T	width of outflow opening at stern
$B_{i,j}$	$i, j = 1, 2, \ldots, 6$, damping coefficient of the vessel
b_{pi}	$i = 3,5$ coefficients for pressure and motion coupling equation
b_{pp}	coefficient for pressure and motion coupling equation
c_d	drag coefficient
C_L	lift coefficient
c_n	flow coefficient
c_p	pressure coefficient
c_w	coefficient of wave-making resistance
$C_{i,j}$	$i, j = 1, 2, \ldots, 6$, restoring coefficients
c_{pi}	$i = 3,5$ coefficients for pressure and motion coupling equation
c_{pp}	coefficient for pressure and motion coupling equation
d	mean draught, draft at chine for prismatic planing hull
D	turning diameter

D_m	main deck depth
D_{ji}	influence coefficients
E	wave energy
E_1	exponential integral
F_b	beam based Froude number
F_g	gravity force/moment component
F_l	$l = 1, 2$, function
F_L	lift force
f_m	$m = 1,2,...,8$, function
f_n	length Froude number of a rectangular pressure patch
F_n	length Froude number for ships
$\mathbf{F_H}$	hydrodynamic force/moment vector
$\mathbf{F_P}$	force/moment vector due to cushion pressure
$\mathbf{F_R}$	hydrostatic force/moment vector
$\mathbf{F}_s$	hydrodynamic steady force/moment vector
$\mathbf{F}_t$	total force/moment
$\mathbf{F}_w$	wave exciting force/moment vector
$\mathbf{F}^0$	steady force/moment
$f_{i,m}$	$i = 0,1,...,6;\ m = 1,2,...,8$, function
F_{wj}	$j = 3,4,5$, wave exciting force/moments
F_{wp}	right hand side term in the pressure and motion coupling equation
g	acceleration due to gravity
G_j	$j = 1, 2$, function
$g_{i,m}$	$i = 0,1,...,6;\ m = 1,2,...,8$, function
h	draft at stern for prismatic planing hull
H_j	transom profile
H_m	maximum wave height of wash wave
h_{ji}	impulse response function

h_{ς}	impulse response function for free surface elevation due to pressure
H_{ς}	transfer function of free surface elevation due to pressure
$H_{1/3}$	significant wave height
I_{jj}	$j = 4,5$, craft mass inertia moment for roll and pitch
I_x	roll inertia moment
I_z	yaw inertia moment
J_{im}	$i = 0,1,...,6,\ m = 1,2,...,8$, terms of the free surface elevation
K	roll turning moment, number of Kutta panels
k_i	$i = 0,1,2,3,4$, wave numbers, coefficients of control law
KG	height of centre of gravity from keel
l	cushion length
L	craft length
L_A	appendage lift
L_C	chine water line length
L_H	hull hydrodynamic lift
L_K	keel water line length
l_{cp}	location of pressure centre from stern
L_{cp}	non-dimensional location of pressure centre from stern
L_{OA}	overall ship length
m	mass, index
$\mathbf{M}$	mass/inertia matrix
N	yaw turning moment, number of panels
$\mathbf{n}$	normal vector of vessel hull
n_f	number of inflow fan system
p	pressure, roll angle rate
P	time-varying part of cushion pressure
$\tilde{P}$	complex amplitude of cushion pressure
p_a	atmospheric pressure
p_c	cushion pressure

P_l	pressure in cushion chambers
P_0	pressure in cushion chamber at equilibrium condition
$\tilde{P}_l$	complex amplitude of pressure in cushion chambers
p_s	steady hydrodynamic pressure
p_w	unsteady hydrodynamic pressure
$\mathbf{q}$	craft motion responses
Q_{in}	inflow rate of fan system
Q_{out}	outflow rate
r	yaw angle rate in manoeuvring
$\mathbf{r}$	point position vector
R	turning radius
R_w	wave-making resistance
RMS	root mean square of the motion responses
s	project area
S_0	mean wetted hull surface
S_c	cushion area
s_m	$m = 1,2,...,8$, variables
S_p	distance between central planes of the demi-hulls for a catamaran
$S(t)$	instantaneous wetted hull surface
S_ς	wave spectrum
S_{jk}	$j,k = 0,1$, moments of cushion area
S_{yy}	water plane moment
t	time
T	draft, kinetic energy
T_{01}	average wave period
t_{jm}	$j = 1,2,3,4; m = 1,2,...,8$, function
T_{off}	draft of vessel at off-cushion mode
T_{on}	draft of vessel at on-cushion mode
TL	turning level (m)

u	variable of functions, longitudinal velocity
U	craft speed
u_c	upper limit of the infinite integrals
v	lateral velocity
V	cushion volume
$\mathbf{V}$	velocity on hull surface
V_0	cushion volume at equilibrium condition
v_p	escape volume
$\tilde{v}_p$	non-dimensional escape volume
V_r	relative velocity
v_w	cushion pumping volume due to incident wave
$\tilde{v}_p$	non-dimensional escape volume
$\mathbf{w}$	velocity of the steady flow
X	longitudinal manoeuvring force
x, y, z	coordinates
X_{AP}	appendage force
x_c, y_c	centre of cushion area
x_{cp}	coordinate of pressure centre
x_m, y_m	location of maximum wave height
Y	lateral manoeuvring force
z	heave
Z_0	gap of the stern opening
z_g	height of centre of gravity
Z_{AP}	appendage force
$\hat{z}$	hull offset

Greek Symbols

α	escape area, angle of attack
$\boldsymbol{\alpha}$	displacement vector

$\tilde{\alpha}$	non-dimensional escape area
α_p	escape area due to cushion pressure
$\tilde{\alpha}_p$	non-dimensional escape area due to cushion pressure
β	heading angle, dead-rise angle
γ	ratio of specific heats for gas, Euler's constant, flap orientation, also a variable
δ	nozzle deflecting angle, variable
δ_{ji}	delta function ($\delta_{ji} = 1$ when $j = i$; $\delta_{ji} = 0$ when $j \neq i$)
φ	heeling angle, velocity potential
ϕ	roll motion of the craft, velocity potential
Φ	velocity potential
Φ_s	velocity potential of steady flow
ϕ_D	velocity potential of the diffraction wave
ϕ_I	velocity potential of incident wave
ϕ_j	$j = 0,1,...,7$, complex velocity potentials in space
ϕ_p	perturbation velocity potential for unsteady flow
ϕ_R	velocity potential of the radiation waves
ϕ_s	disturbance velocity potential of steady flow
ϕ_u	velocity potential for unsteady flow
ϕ_∞	velocity potential of uniform incoming flow
μ	added mass for section of slender body
θ	pitch motion, also a angular variable
$\boldsymbol{\theta}$	vessel rotating vector
θ_c	cut off angular variable
ρ	water density
ρ_a	atmospheric air density
ρ_0	density of air at equilibrium condition
σ	encounter frequency
τ	reduced frequency, time
ξ	coordinates

ξ	translation motion vector
η	coordinates
η_k	complex amplitudes of motion response
λ	wave length
ς	wave surface elevation
ς_1	local wash wave
ς_2	non-local wash wave
ς_a	amplitude of incident wave
ς_p	free surface elevation due to cushion pressure
$\tilde{\varsigma}_p$	non-dimensional free surface elevation
ς_s	free surface of steady flow
ς_u	free surface of unsteady flow
ς_w	incident wave elevation
ω	wave frequency
ψ	function, yaw angle
Π	pressure distribution
Π_0	pressure
Ω	cushion surface
Σ	hull surface
$\forall$	displacement volume
Δ	displacement of vessel
$\Im_j$	$j=1,3,5$, right hand side of the differential equations for pressure, heave and pitch motions
I_j	$j=1,2,4,5,6$, integral
Ξ_j	$j=1,2$, function

List of Acronyms

ACS	Air Cavity Ship
ACV	Air Cushion Vehicle
ALV	Air Lifted Vessel
ASV	Air Supported Vessel
CFD	Computational Fluid Dynamics
HSC	High Speed Craft
RANSE	Reynolds-Averaged Nevier-Stokes Equations
SES	Surface Effect Ship

Chapter 1 Introduction

In recent years, improving the competitiveness, safety and security of shipping has becoming a major objective of maritime transportation. Increasing fuel prices and strong environmental concerns (regulations and cargo carrier demands) have changed the competitive landscape. To meet the changing commercial market and economic environments, new vessel designs will be required with more flexibility in their design and will be more energy efficient and cost effective to operate. Key drivers for enhanced ship technologies include advanced ship design and propulsion technologies and operation system and processes. There are a number of emerging technologies and techniques becoming available for use on-board ship, which will support improved efficiency and quality of maritime transport services (reliability, safety, security and environmental performance).

A ship can be considered to be efficient if it is profitable, environmentally compatible and if it complies with safety, health and environment policy. There are several methods of adapting a vessel’s hull to improve performance, reduce fuel consumption and lower emissions such as changing the hull shape, dimensions, displacement and block coefficient to reduce the vessel’s resistance of a ship.

The concept of drag reduction by supplying air under the ship’s bottom was proposed in the 19th century by the famous scientists Froude and Laval. However, many attempts to implement this idea in practice have failed because this process is not as straightforward as it seems. Deep physical understanding of multiphase flow is required to achieve a positive outcome. The Research Institute in St Petersburg contributed significantly in 1960’s. Potential benefits of air injection under ship hulls without flexible seals have always been of interest to the shipbuilding community worldwide. However, until the last decade or so, development attempts were not serious enough to achieve convincing results. In recent years, R&D activity in this field was significantly increased in Europe, USA, Japan, Korea, Australia and China.

Because of the commercial nature of these projects, reliable data is not yet available to judge for certain the progress in air cavity technology.

The resistance of a ship is conventionally decomposed into the following three components: the wave-making resistance, the frictional drag and the viscous form drag. For high-speed craft, wind drag should also be considered, but this will not discussed in the present study. The Air Cavity Ship (ACS) concept is based on successful usage of bottom ventilation (artificial cavitation). Air is supplied underneath a special profile, so that a steady air layer is generated which separates a part of the bottom from contact with water. Compared to conventional displacement hulls, Air Cavity Ship (ACS) with captured air plenums has potentials in reducing frictional resistance because the wetted area of the vessel is significantly reduced. For ship with a low speed, the frictional drag is a major part of the total resistance, while the power spent on the cavity maintaining the air flow is less than 3% of the total propulsive power of a vessel. The potential reduction of the total resistance and power saving are significant.

The high-speed version of the Air Cavity Ship (here we call it as the Air Supported Vessel, ASV) also has potentials for resistance reduction and power saving. In this case, the wetted hull area is reduced by three effects: first is the air cavity underneath the hull; secondly, the excess pressure inside the cushion is higher than that of an ACS at low speed, this pressure force will lift the hull upwards, and reduce the wetted hull area. Thirdly, the forward part of the rigid hull is specifically designed as a planing surface. When the vessel is at a high-speed, the planing surface will generate dynamic lift and reduce the wetted hull area even further. The total frictional resistance is reduced with a higher excess cushion pressure but the fan power is increased instead. In addition the wave-making resistance due to cushion pressure increase but at small rates fairly constant for a certain range of speed. Together with a moderate residual resistance, the total resistance of the ASV is reduced and a power saving can be reached.

A schematic arrangement of the air cavities for low speed displacement ships and high-speed planing crafts is illustrated in Figure 1.1 (Matvvev, 2009). A recess is made on the hull bottom that accommodates the air cavities. The air is injected into the front part of the cavities and leaks from the cavity trail. Several cavities may be arranged for slower ships.

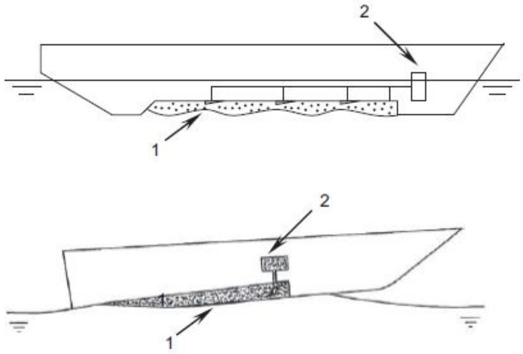

Figure 1.1 Hulls with air cavities: (top) displacement, (beow) planing hull. (1) air cavity; (2) air blower [Matveev, 2009]

Harley Shipbuilding in the USA (Harley, 1996) and SES Europe in Norway (Tudem, 2002) have developed the air supported platform called the ‘Air Lifted Vessel’ (ALV), which is essentially a catamaran with air cushion similar to that of an SES but the hulls have planing sections in front of the bottom recess and no flexible seals are used. Another characteristic feature of the ALV is the longitudinal keels on the sides of the cavity that prevent air from escaping. The reported resistance reduction is around 25% based on tank testing (Allenstrom et al. 2001, 2003). The ASV could also be a mono-hull (Gokeay et al., 2004).

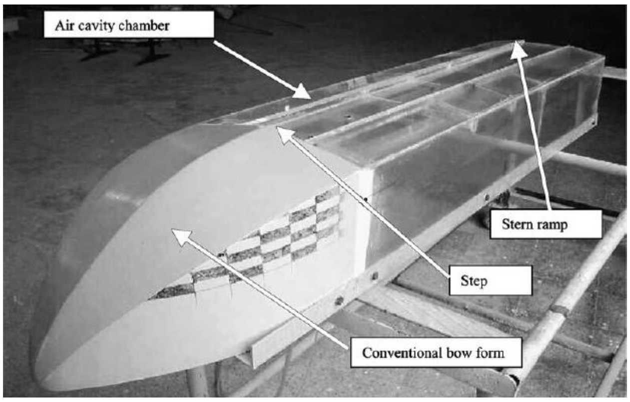

Figure 1.2 Mono-hull of ASV (Gokeay et al., 2004)

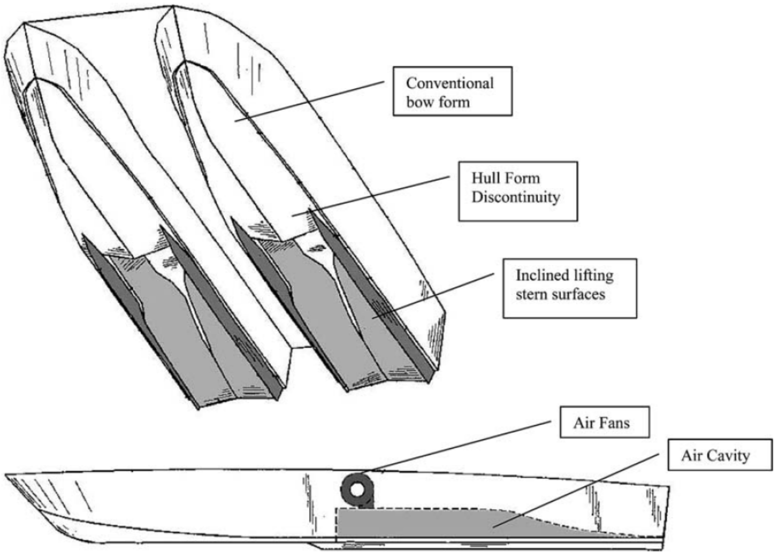

Figure 1.3 The hull form of the Air Supported Vessel by Harley (1996)

A similar and more familiar concept is the surface effect ship (SES), where air is also pumped under the ship’s bottom. Such a vessel usually has flexible bow and stern skirts enclosing the space between the two thin side-hulls. The air cushion vehicle (ACV) also uses the compressed air under hull to support the vessel’s weight, but it has no permanently submerged hull at speed (Faltinsen, 2005).

Although the principle of the ASV seems similar to that of an SES, there are significant differences. First, there are no flexible seals on an ASV. The air layer is contained by solid hull parts, which not only prevent air leakage from the cushion, but also influence the air cavity characteristics. Secondly, the air flow rate needed to support the air cushion on an ASV is about ten times less than on an SES. Therefore, an ASV is a much more economical means of transportation.

Another popular concept is drag reduction achieved by using micro-bubbles (Fukuda et al., 2000). It is normally easier from the technical side to create a bubbly flow instead of large stable air cavities, but the overall effectiveness of this idea is still under investigation. Air bubble motion usually includes a random component, and some bubbles may stick to the hull. These effects can even augment the effective roughness of a hull surface and lead to an increase in drag.

The most distinguish feature of the ASV from conventional ship is the air cavity induced flow. The disturbed flow could be steady (in case of the calm water resistance problem) and unsteady (e.g., for ship travelling in waves). Also, part of the flow is disturbed by the rigid part of the hull. Theoretical and numerical analyses of the flows and hull form optimization are aimed at creating effective approach to ASV design.

Most of the studies on the air cavity ship so far have been focused on hydrodynamics in calm water, which is the resistance problem of the vessel in still water (see, for example, Gokcay et al., 2004, Matveev, 2007, Matveev et al. 2009). As part of the process of developing an ASV, the design tools should cover other performances as well. The ship should travel on a wave condition. Ship motions in waves will affect performance of the air cavity on the drag reduction considerably. On the other hand, ship motion in a seaway has implications on its performances, such as sea sickness of the crew members and passengers and effectiveness of equipment on board as well.

One of the particular concerns for ASV is so called wash wake effect. The wash wave of a high-speed craft could be potentially damaging to the environment of the shore lines, dangerous to swimmers in the tourist attractions and potential impact on marine wildlife habitats. Significant problems related to wash in the marine environment have been reported. High-speed craft operators have to undertake a risk assessment with respect to wash in order to get an operational permit in some countries (e.g., Denmark, U.K.). Low wake wash is becoming one of the key objectives of HSC design. In any case, an efficient and reliable numerical method for predicting the wake wash wave of the ASV is desirable.

Marine accidents may result tragic consequence. International developments pertaining to high speed craft acknowledge the necessary of improvements of marine safety standards for high speed craft in order to maintain the highest practical level of safety. However, the continuous update of stability rules and regulations for advanced high speed vessels is greatly influenced by the fact that there are many different types of high speed vehicles, and many different alternative design solutions within each category, so a meaningful way to set safety and operational standard is to use performance based criteria and safety levels to which any type of craft must verify compliance. The design feature of the ASV requires a close look at its stability issues, both static and dynamic.

The present study attempts to address some of the hydrodynamic characteristics of the ASV, in particular, the ASV catamaran. Chapter 2 presents the aim of the thesis and Chapter 3 describes the approach adopted. A critical review of the relevant researches is given in Chapter 4. The boundary value problems to describe the steady and unsteady potential flows around the vessel are presented in Chapter 5. Forces, moments and equations of motions of the vessel are also derived in this chapter. Chapter 6 deals with the three dimensional steady flow of a pressure distribution moving on the free surface. Emphasis is placed on the numerical solutions for rectangular pressure patch, which is the elementary solution of the problem. The singularity and highly oscillatory behaviour is properly handled. Chapter 7 is the case studies for the steady potential flow problem: prediction of 3D hydrodynamic pressure distribution of flat plate planing hull, flat plate planing catamaran hull and prismatic planing hull. Chapter 8 is the case study of application for the wash wave prediction of the ASV. Chapter 9 presents solution of the unsteady potential flow of a pulsating and moving pressure distribution on the free surface. It concentrates on the numerical aspects, where reliable numerical schemes are provided for the 4 wave numbers at different frequencies and field point locations. Equations of motions of the ASV in waves in frequency domain are presented for the seakeeping analysis. Additional equations to couple the air pressure in the cavity (cushion) and the vessel motions are established by using the adiabatic gas law and air flow continuity equation. Chapter 10 is a case study of seakeeping prediction for the ASV in frequency domain. Motion responses (pitch, heave roll and vertical acceleration at bow) of the ALV, E40, in irregular waves have been predicted for a range of Froude numbers and wave heading angles. Chapter 11 deals with the stability of the ASV.

The transverse static stability at zero speed, longitudinal dynamic stabilities and stability in manoeuvring in calm water are considered. The mathematical models for the dynamic stability analysis are nonlinear and are solved in the time domain. The time domain representation of the cushion pressure force is calculated by the impulse response function approach. Chapter 12 is the case study for the stability performances of the ASV. A longitudinal dynamic instability was identified for pitch and heave motions in calm water for the ALV E40. This phenomenon is connected to the vessel design parameters and characteristics of the fan system. The simulated results in manoeuvring (turning and directional stability) are also checked against the IMO requirements. Chapter 13 summarizes the main achievements and contributions of the present study. Chapter 14 presents recommendations for the future work based on the present study. A list of references is given at the end of the thesis.

Chapter 2 Aims

The main objective of the present thesis is to develop mathematical models and their associated numerical methods to predict the hydrodynamic performance of ASV ships; it is expected that the developed analysis methods and developed tools will be helpful in design and operation of the ASVs. The aim of this thesis is set specifically as follows:

1. To carry out numerical computations for the flow disturbed by the ASV in calm waters;
2. To carry out numerical computations for the fluid flow of the ASV travelling in harmonic motion;
3. To establish mathematical models and numerical methods for seakeeping prediction of the ASV in frequency domain;
4. To establish mathematical models and numerical methods for the dynamic stability analysis of the ASV.

A number of case studies will be provided to demonstrate the effectiveness and applicability of the numerical methods.

Chapter 3 Approach Adopted

Unlike conventional ships, the Air Supported Vessels have three components of vertical forces to support the vessel's weight: compressed air pressure force, hydrodynamic lift and buoyancy. The proportional of each of the component varies for different vessel designs and their speeds. For a high speed application, the air pressure force and the hydrodynamic lift may be dominant. The disturbance of the vessel and the external reaction forces on the ship come from both the pressure distribution and the wetted rigid hull. The fluid flow around the hull is rather complex, and numerical prediction of the external force on the vessel is challenging. There will be wave-breaking and sprays. The mixture of water and air may exist inside the cushion(s). There will also viscous effect on the flow.

In the present study, a number of assumptions will be made. First, the fluid (water) is assumed as ideal and incompressible, no viscous effect will be taken into account unless otherwise indicated, the water flow is assumed to be irrotational. Therefore, the water flow field can be described by potential flow theory. Secondly, the wave breaking and the spray are ignored as well; thirdly, the two-phase flow of mixture air/water inside the cushion is treated as air, however, the compressibility of the air inside the cushion will be considered, and the air pressure is assumed as inhomogeneous. Finally, the free surface boundary condition is linearised at the undisturbed free surface and the vessel hull boundary condition is linearised on the mean wetted hull surface.

The potential flow theory assumption implies that no viscous effect is taken into account. This means that only wave-making resistance can be predicted, the residual and frictional resistance components need to use other approaches if one want to predict the total resistance of the vessel, such as model testing or RANSE CFD (Computational Fluid Dynamics). Viscous effect on the resistance of a ship is important, such as viscous pressure resistance and frictional resistance. Normally, the total resistance of the ASV consists of the frictional resistance, wave-making resistance due to the cushion pressure, the residual resistance and wind drag. The residual resistance contains wave pattern resistance created by the hull, viscous pressure resistance, spray and eddy-making resistance, and possible induced resistance if there is a cross flow about the side keels (Allenstron et al. 2001). Due to the assumptions made in the present study, it is unable to predict the residual resistance component of the ASV, some approximate approach will be needed and comparison can be made with model testing. The viscous effect is less important for seakeeping problem, except for ship roll damping. Linearsation of the free surface condition and hull boundary condition restricts our study on small amplitudes for both the incident wave and vessel motions.

With growing capabilities of CFD, hydrodynamics of realistic ship hulls can be modelled in great detail, including viscous effects. This is particularly the case for prediction of ship resistance in calm water, see for example, Larsson et al (2011). However, for the unsteady ship flow problem, such as seakeeping of a ship in waves, the current capability of CFD is unable to provide results in an acceptable time frame due to the needs for evaluation of ship motions in a variety of sea states under a large number of headings. Simplified flow models, such as those based on the potential flow theory, remain as the main approach to tackle the problem of the ship-wave interaction.

The fluid flow around the ASVs is mathematically modelled by the disturbances of a pressure distribution and the wetted part of the rigid hull moving on the free surface, see Figure 3.1.

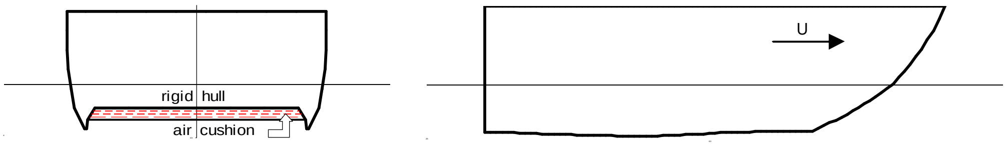

Figure 3.1 Air cushion and rigid hull of the ASV

Both the steady and unsteady pressure components are considered in the present study. In solving the steady and unsteady flow problems, the projected area of the air cavities on the free surface will be discretised into rectangular pressure patches. The solution of a pressure patch is the elementary solution of the problem and involves most of the computational efforts. The adiabatic gas law is used to couple the pressure in the cushion and the vessel motions. The seakeeping motion prediction will be carried out in frequency domain, while the dynamic stability analysis including manoeuvring simulations is carried out in the time domain. In the time domain models, the non-linear effect for coupling vessel motions and the cushion pressure is included.

When a vessel is designed, we need to predict its performance, such as resistance/powering, wash wave, seakeeping, etc, during its operation, this is called the direct problem. On the other hand, if the vessel’s performance(s) is specified in advance, and one needs to find the suitable design, this is called the indirect problem. The present study deals with the direct problem for the ASV, i.e., prediction of the hydrodynamic performances. With the developed mathematical model/tools, the effect of parameters of the hull, such as hull dimensions, dimensions of the air cushion, fan system(s), etc., on the vessel’s performance can be investigated.

In order to solve the direct problem, normally three approaches can be used: model test, full scale trial and numerical prediction. In the numerical prediction method, a mathematical model should be established for the physical problem concerned, and a numerical method is used to solve the mathematical model. The numerical results should be validated against the model test and/or full scale measurements. Once the numerical tools for solving the direct problem have been established, these tools can be used to address the indirect problem, for example, how the design parameters affect the performances of the vessel. Model tests and full scale trails are far more expensive to be adopted to address the indirect problem.

Chapter 4 Critical Review

In this Chapter, previous studies relating the hydrodynamic performances of the Air Supported Vessels, such as, the steady flow, hydrodynamics of planing hulls, far field wash wave prediction, ship motion in waves (seakeeping) and the stability are critically reviewed.

4.1 Prediction of the Steady Flow

Flows resulting from the Air Supported Vessels and high-speed planing crafts can be modelled via a moving distribution of pressure at the free (air/water) surface (for example Faltinsen 2005, Doctors 1985), or by using a free-surface pressure distribution together with distributions of source over the rigid side-hulls (modelled as thin ships) (Choi et al. 2005, Doctors & McKesson 2006). The main difference between the two methods is that the effect of the rigid side hulls is considered in the late approach. When the vessel's weight is mainly supported by the cushion excess pressure force or hydrodynamic lift force, the moving pressure distribution only method is expected to be a reasonable approximation. However, when buoyancy plays a more important role, the combined moving pressure distribution and source distribution method should be used, such as an Air Cavity Ship with a low to medium design speed. The computational effort will be doubled for the combined method.

Accordingly, flows resulting from a moving pressure patch on the free surface have been considered in a series of classic studies. In particular, the wave drag of a pressure patch advancing at a constant speed along a straight path on the free surface is considered in Havelock (1932) for deep water and in Lunde (1951) for finite water depth. Wave-drag calculations are also reported in Newman and Poole (1962) and Barratt (1965). The wave drag of a moving pressure patch on the free surface in steady and accelerated motions is considered in Doctors and Sharma (1972). The complexities and uncertainties associated with pressure distributions with shape edges are further examined in Zilman (2006).

The basic computational task of evaluating the steady near-field flow resulting from a moving pressure distribution on the free surface is considered in Doctors (1975) for deep water. The Green function for the steady flow in deep water has also been considered in a number of studies, where alternative mathematical representations and practical approximations – based on complementary near-field and far-field asymptotic approximations, and numerical approximations based on Chebyshev polynomials or table interpolation – are given (e.g., Noblesse 1978, 1981, Newman 1987, Telste & Noblesse 1989, Masson et al. 1991 and Ponizy et al. 1994).

More recently, Noblesse et al. (2009) presented a practical evaluation method for evaluating the free-surface elevation caused by the moving free-surface patch. The key ingredient of the method is a highly simplified analytical approximation to the local-flow component in the expression for the Green function associated with the classic Michell-Kelvin linearized free-surface boundary condition. The computational procedure for determining the free-surface elevation due to the passage of a pressure distribution is a complicated problem. In general, the calculation of the free surface elevation involves a quadruple integral – two for the dimensions of the disturber, one for the direction of the propagated plane waves and another for their wave number – some of which are computationally challenging due to the rapidly oscillating and singular integrands. Scullen and Tuck (2011) described an efficient and accurate method for computing the linearized free-surface disturbance of a moving pressure distribution. A method for desingularising the local-field integrand so that the free surface elevation can be calculated beneath the applied pressure patch is presented.

Besides the free-surface Green function method, several researches have been carried out via Rankine source distribution method. Matveev (2007) presents an approximate model for calculating wave patterns in the upstream part of long air cavities in a simplified, horizontal-plane geometry. The model is extended for multi-wave cavity configurations (Matveev, 2009). The aim of the study is to determine dimensions of a hull recess that accommodates the air cavity of an Air Cavity Ship. Rankine sources are distributed on the free surface inside and outside the air cavity. The influence of the recess planform boundaries and other factors on the wave patterns is studied parametrically. Choi et al. (2005) use a time domain boundary element method to study the wave-making resistance of an ACS. The effects of the dimension and size of the air cavity on the resistance characteristics are investigated.

There are some on-going efforts to apply RANSE volume method for modelling the steady flow around an Air Cavity Ship. Dogrul et al (2010) use a commercial CFD code to investigate frictional resistance of an equivalent flat plate of an ACS's wetted surface at various air flow velocities and ship's Froude numbers. Insel et al. (2010) simulate the steady flow of more complicate geometry of the hull and the air cavities by RANSE method. The flow patterns are compared with model tests.

4.2 Hydrodynamics of Planing Hull

When a craft is planing, the majority of its weight is supported by the hydrodynamic lift and the flow is assumed separating smoothly from the trailing edge and part of the side hull. This feature of planing allows researchers to adopt a pressure distribution on the water surface to represent the effect of the wetted area of a planing surface, and to establish an integral equation which relates the unknown pressure on the planing surface to its hull offsets.

Early studies on the planing problems were seen in the 1930's, but until the 1960's theoretical investigations were restricted mainly to linearised two-dimensional planing (Maruo, 1951). The three dimensional planing problem was tackled in the 1960's, but always with restrictions on either the planing speed or aspect ratio of the planing surface (Maruo, 1967; Wang and Rispin, 1971; Shen and Ogilve, 1972; Tuck, 1975). Doctors (1975) may be the first to study the three dimensional planing without these restrictions. In his approach, finite pressure elements were adopted to represent the wetted area of a planing surface and in an iterative procedure the wetted area was adjusted to satisfy the trailing-edge Kutta condition until it finally reached a constant, but the pressure distributions thus obtained were seriously oscillatory. Wellicome and Jahangeer (1978) and Tong (1989) prescribed the wetted area in advance, then calculated the pressure distribution and shape of the transom. The pressure oscillation, which Doctors found, was avoided when the number of buttocks was not more than five or six, otherwise it would still occur. The reason for such oscillation was believed to be the pressure discontinuities at the side edges of the constant pressure element they employed.

To avoid the pressure oscillation problem, Cheng and Wellicome (1994) developed a pressure strip method, in which a planing surface is represented by an assemblage of strips of transversely variable pressure placed on the mean free surface. The pressure oscillatory problem was successfully removed. But the transverse strip method was less successful for prismatic planing hulls (Cheng and Wellicome, 1999). Studies of Tuck, Scullen and Lazauskes, (2002) and Wang and Day (2007) showed the same problem of numerical instability in which the predicted pressure distribution shows a grid-scale oscillatory behaviour.

More recently, Noblesse, Delhommeau and Yang (2009) provided a practical evaluation method for the point pressure free surface Green function of the steady flow. Scullen and Tuck (2011) provide a numerical method for calculating the three dimensional near-field and far-field free-surface elevation due to moving pressure distributions. No prediction for the hydrodynamic pressure distribution was provided for those studies.

Methods using various computational techniques have been developed to tackle the planing hydrodynamic problem. Lai and Troesch (1996) developed a three-dimensional numerical model using vortex lattice method to solve the steady planing problem. A special vortex condition is applied to obtain the detailed flows at the leading, side and trailing edges. Matsumura and Katsui (1999) modelled the wetted surface of the planing craft in still water using vortex line and the circulation distribution around the longitudinal sections. Savander et al. (2002) formulated the boundary value problem for the steady planing surfaces and utilized a relation between the perturbation potential and vortex distribution. They obtained numerical results involving hydrodynamic pressure, lift and resistance for a planing craft at various speeds. Zhao et al. (1997) carried out a 2.5D (2D+ t) analysis of a high-speed planing craft in calm water. Taravella et al. (2011) developed a general solution for a flat and slender planing surface with a vortex distribution method. Faltinsen (2005) gave details on the hydrodynamics of a planing vehicle. Ghassemi et al. (2008), Matveev et al. (2009) and Kohanasal et al. (2010) adopt Rankine source panel method for the steady potential flow of a planing hull.

With growing capabilities of computational fluid dynamics, hydrodynamics of realistic high-speed ship hulls can be modelled in great details, including viscous effects. Subramanian et al. (2007) carried out a RANSE simulation for the steady flow around a planing hull.

In parallel with the theoretical development, numerous experimental studies of planing hydrodynamics have also been carried out, for example, Clement et al. (1963), Kapryan et al. (1955), Latorre (1982), Scottorf (1932), Shoemaker (1934). Savitsky (1964) derived regression formulae for prismatic planing hulls from a series of model tests, the formulae have been widely used in the prediction of the hydrodynamic characteristics of a planing craft. Katayama et al. (2002) performed the resistance test for the high-speed planing craft with prismatic hull forms at various speeds and reported the lift and resistance coefficients.

4.3 Seakeeping Prediction of the Air Supported Vessels

Traditionally, seakeeping predictions for ships are to solve the diffraction/radiation problem (2D, 2.5D and 3D) and to calculate hydrodynamic and wave exciting force/moments on the vessel. For an Air Supported Vessel, additional forces/moments of the excess pressure in the air cushion will be applied on the hull surface. In some cases, this excess pressure forces form major part of the external forces (e.g., the ALV). There was significant focus on understanding of the relevant physics, which led to the development of simulation models in the 1970’s and 1980’s. Doctors (1972, 1974 and 1977) coupled a linearized hydrodynamic model based on Green’s function method and a compressible fluid model for the air cushion to simulate the motion of a fully-skirted Air Cushion Vehicles (ACVs) in waves. The vehicle and air cushion dynamics were coupled to the free surface elevation via a pressure term added to the free surface boundary condition in the region beneath the air cushion. This work demonstrated the importance of treating the air cushion as a compressible fluid and showed the effect that a deformable free surface has on the unsteady vehicle motion. In particular, the relationship between the vessel motion and the cushion dynamic pressure was established; the mathematical expression for the free surface elevation due to a moving and oscillating pressure distribution was derived and some numerical results were provided. Similar approaches were developed by others to investigate seakeeping performance of the ACV. Collectively, these works have formed the basis for standard physics-based dynamic simulation models of the Air Supported Vessels (Yun et al. 2005).

Several models have been suggested to simulate the air flow in the air chamber. Doctors (1974), Chen (1977) and Kim et al. (1981) assumed the bubble (or cushion) pressure is spatially homogeneous, and only changes with time. The key challenge for this method remains as the evaluation of the free surface elevation at a field location for any combination of frequency and ship speed generated by a pulsating and moving pressure distribution on the free surface due to, not only the singularities and highly oscillatory integrands, but also wave numbers involved depending on the frequency and forward speed.

Sorensen and Egeland (1995) developed a simulation model for a SES which solved the one-dimensional wave equation for velocity potential to model the longitudinal pressure distribution inside the air chamber. This capability was used in the design of a ride control system and to reduce the cobblestone effect and significantly improve the motions of the vessel. Steen and Faltinsen (1995) studied high frequency dynamic response of a SES equipped with a flexible bag aft seal. The mathematical model accounts for the motions and accelerations in heave and pitch induced by both the unsteady uniform pressure and the spatially varying air cushion pressure (with modal solutions). Okita, Sahin and Hyman (2001) carried out a numerical study on disturbance during the unsteady motion of a two-dimensional pressure distribution, and indicated the difficulties in convergence for evaluation of the free surface profile because of the highly oscillatory integrand.

Thill et al. (2005) developed a mathematical model for seakeeping prediction of the air cavity ships. An air chamber dynamics model with spatially homogeneous chamber pressure distribution is incorporated to a 3D time domain radiation/diffraction panel code. The code uses a linearized free surface boundary condition and distribution of the transient Green function on the hull surface. Milewski et al. (2007) implemented a three-dimensional compressible fluid model to describe the air flow in the chamber of an ACV with small length/beam ratio. The hydrodynamic part of the flow (due to the wetted part of the rigid hul) is simulated by a time domain Rankine source panel method.

Several model tests have been carried out on the seakeeping performances for the ASVs. Allenstrom et al. (2001, 2003) investigated motions of the ALV in irregular head waves in a towing tank. Thill et al (2005) measured seakeeping characteristics of an Air Cavity Ship in head and oblique waves and compared the motion response with/without air chamber with numerical simulations. The results indicated that the seakeeping characteristics of the investigated ship are not significantly affected by the use of either bubbles or air chambers for the air lubrication. Power saving may become negative when using air chambers at relatively low speed. It also reveals that predictions for air chambers dynamics such as the variations of air volume, pressures and air losses seem to be in qualitative agreement with expectations. Cheng et al (2011) and Dong et al (2011) carried out model tests of vessel motion in waves for ASV mono-hull crafts (hard-chin planing hull). It was found that a properly design cavity can reduce resistance and motion response in waves as well.

4.4 Stability Study of the Air Supported Vessels

A classification of general type of instability of mono-hull ships was presented by Cohen and Blount (1987). Compared to conventional ships and their stability rule, safety codes for high speed craft need to include further requirements. High speed vehicles are in particular much more sensitive to problems associated with motions, transverse and longitudinal stability, control and behaviour in different sea states. The dynamic stability of high speed vessels both in calm water and in waves is in general poorly understood (Faltinsen, 2005). It should be noticed that the importance of hydrostatic pressure relative to hydrodynamic pressure decrease with increasing forward speed. One should also note that the rudder, cavitation and ventilation phenomena will influence the dynamic stability of high speed vessels. For catamaran, since it has a larger beam than a mono-hull, the catamaran with the same position of the centre of gravity as the mono-hull will have the clearly highest metacentric height.

Porpoising is a longitudinal dynamic instability for coupled heave and pitch motion for planing vessel, see for example, Savitsky (1964), Faltinsen (2005). Design guidelines are available for predicting and avoiding porpoising (Blount and Codega, 1992). Inception of porpoising can be found by a linear stability analysis. Small perturbations from the steady equilibrium position are then dynamically examined. There are no excitations, for instance, due to wave loads. If a small initial perturbation is given to the system and the motions grow with time, the system is unstable. A nonlinear stability analysis is needed to get a measure of how larger the unstable motion may be.

For an Air Supported Vessel, location of ship’s centre of gravity (both longitudinal and vertical from the keel), metacentric height, cushion beam, side-hull form and draught, air cushion pressure, and ratio between buoyancy and air pressure forces are the most relevant parameters to their stability. Other design variables that significantly affect stability are

1. Side hull length and dead-rise;
2. Type of bow and stern seal;
3. Size and location of skegs, fences and rudders;
4. Type of propulsion system;
5. Type of manoeuvring system.

When operating close to a capsizing condition in the above mentioned situations, behaviour of SES and the ASV is extremely complex and, in many cases defies analytic treatment. Non-linearities in forces and moments which result from such behaviour must be mainly assessed by model testing or full scale trials. Therefore step-by-step approach to evaluate stability of SES and ASV is preferred. A study of adaptation of the stability rules and tools to SES was carried out by Papanikolous et al (2002). The stability criteria which can be applied to SES and the applicability of the HSC code (IMO, 2000) were presented. Vassalos (1995), Blyth (1983), Lavis (1979), and Gonzalez (2002) have provided the stability criteria in calm water and waves for SES.

Kaplan, Bentson and Davis (1981) carried out a direct simulation of behaviour of SES. A description was given of importance of dynamics problem and their influence on the performance and design of SES. The interrelationship between analytical studies and test data, from models and manned test craft, is discussed together with a description of the problems associated with scaling motion responses between model scale and full-scale vessels due to the important influence of air pressure. The development of a non-linear computer program that describes the six degree of freedom motion of SES was given, showing its application to the prediction of horizontal plane manoeuvring and vertical plane motion in waves. Kaplan (1995) studied the manoeuvring and stability of SES and catamaran ships. The procedures used for determining the manoeuvrability of the cushion borne surface effect ships were described and illustrated, including theoretical prediction techniques and their comparison with model test data and full scale test craft trajectories. The results shown the hydrodynamic forces on the side hulls are less dependence on the cushion pressure. Wade and Wang (1977) carried out model tests in a free surface water tunnel to measure forces and moments on a typical SES side-hull. These measured data is used to validate the use of slender body theory for the prediction of side-hull hydrodynamic characteristics. Generally correlation of the data with the theory was very good.

The study of stability for the ASVs is scarce in the public domain.

Chapter 5 Mathematical Model

In this Chapter, the boundary value problem for the Air Supported Vessel travelling in waves will be presented within the potential flow theory. Both the steady and unsteady flows will be considered. The boundary value problems are further linearized. These mathematical models form the theoretical basis of the present study.

5.1 The Boundary Value Problem

To describe the flow fields and motions of a rigid body translating forward with mean speed, U, three Cartesian co-ordinate systems will be defined. The system $O-XYZ$ is fixed in space, system $o_0-x_0y_0z_0$ is fixed with respect to the body and system $o-xyz$ is the steady translating system with the mean forward velocity of the ship. The steady translating system ($o-xyz$) is an inertial frame with the $x-$axis translating on the undisturbed free surface with the same forward velocity U of the ship. The orientations of the axes of the Cartesian co-ordinate systems are defined as in Figure 5.1. The $xoy-$plane is on the undisturbed free surface, $ox-$axes pointing towards the bow and $oz-$axes pointing upwards. When the ship moving at a constant forward speed and without the oscillatory motions (steady state), the system $oxyz$ and system $o_0x_0y_0z_0$ coincide, $xoz-$plane is on the longitudinal symmetric plane and $oz-$axes is through the centre of gravity ($C.G.$) of the ship.

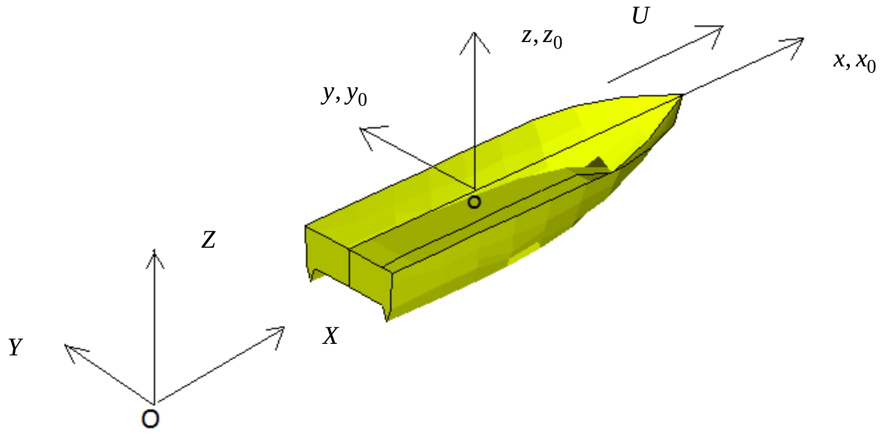

Figure 5.1 The coordinate systems

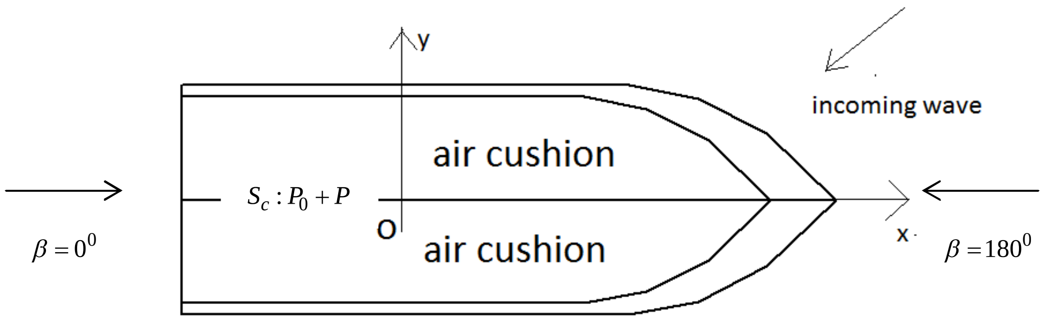

Figure 5.2 Air cushion of an Air Supported Vessel

The heading angle of the incoming wave is defined as angle between $x-$ axes and the wave direction, with $\beta = 180^0$ representing head wave and $\beta = 0^0$ being following wave. The encounter wave frequency is defined as

$$\sigma = \omega - \frac{U \cos\beta}{g}\omega^2 \tag{5.1}$$

where U is the mean forward speed of the vessel, ω is wave frequency of a regular incoming wave, g is acceleration due to gravity.

It is assumed that the fluid is ideal (no viscous effect will be taken into account unless otherwise indicated), water is incompressible and the water flow is irrotational. The external force on the vessel is given:

$$\mathbf{F}_t = \iint_{\Sigma} p_t \ \mathbf{n}\ ds \tag{5.2}$$

where p_t is the pressure distribution over the hull surface (Σ) and $\mathbf{n}$ is normal of Σ. Σ consists two parts: one is the wetted hull surface and another is part of the surface of the air chamber for the ASV. The pressure distribution on the cushion consists of two components: $P_0(x,y)$, a steady state excess pressure (time-independent); and $P(x,y,t)$, the unsteady excess pressure (time-varying part). The water flow field around the vessel can be described by a velocity potential, $\Phi(x,y,z,t)$, which satisfies Laplace equation:

$$\frac{\partial^2\Phi}{\partial x^2} + \frac{\partial^2\Phi}{\partial y^2} + \frac{\partial^2\Phi}{\partial z^2} = 0 \tag{5.3}$$

By using the velocity potential, the pressure distribution in the water flow field can be calculated by Bernoulli equation:

$$-\frac{p-p_a}{\rho}=\frac{\partial\Phi}{\partial t}+\frac{1}{2}\nabla\Phi\cdot\nabla\Phi+gz-\frac{1}{2}U^2 \tag{5.4}$$

where ρ is water density. On the water surface, there are two boundary conditions:

1. the pressure should equal to the atmospheric pressure (p_a) outside the cushion area; and equal to the cushion pressure inside the chambers;
2. a fluid particle can not leave the surface.

In mathematical terms, those conditions are given by

$$\frac{\partial\Phi}{\partial t}+\frac{1}{2}\nabla\Phi\cdot\nabla\Phi+g\varsigma-\frac{1}{2}U^2=\begin{cases}-\left(P_0+P\right)/\rho & (x,y)\in S_c\\ 0 & (x,y)\notin S_c\end{cases} \tag{5.5}$$

where S_c is the cushion area, and

$$\frac{\partial\varsigma}{\partial t}+\nabla\Phi\cdot\nabla\varsigma=\frac{\partial\Phi}{\partial t} \tag{5.6}$$

both on $z=\varsigma(x,y,t)$, the unknown momentary position of the water surface, which given by

$$\varsigma=-\frac{1}{g}\left(\frac{\partial\Phi}{\partial t}+\frac{1}{2}\nabla\Phi\cdot\nabla\Phi-\frac{1}{2}U^2\right)-\frac{1}{\rho g}\begin{cases}P_0+P & (x,y)\in S_c\\ 0 & (x,y)\notin S_c\end{cases} \tag{5.7}$$

These conditions are well known as the dynamic and kinematic conditions.

The vessel is assumed to be impermeable, so no water particles can come across this boundary. The normal velocity of the fluid (water) should therefore equal to the normal velocity of the vessel on the instantaneous wetted hull surface, $S(t)$:

$$\frac{\partial\Phi}{\partial n}=\mathbf{V}\cdot\mathbf{n} \qquad \text{on } S(t) \tag{5.8}$$

where $\mathbf{V}$ is the velocity of the points on the hull surface.

On the bottom of the fluid domain, no fluid particles may cross this boundary:

$$\frac{\partial\Phi}{\partial z}=0 \qquad z\to-\infty \tag{5.9}$$

We also need to provide initial condition. It is assumed that at $t=0$ the fluid is undisturbed:

$$\Phi(x,y,z,0)=0 \tag{5.10}$$

and

$$\frac{\partial \Phi}{\partial t}(x, y, z, 0) = 0 \tag{5.11}$$

To make the solution of the above mathematical model unique, we have to impose an extra condition, called radiation condition. This condition states that the radiated waves should travel away from the vessel.

5.2 Linearization of the boundary conditions

The problem formulated in the previous section contains several non-linearities, namely, the free surface boundary conditions and the hull boundary condition. It is very difficult (if not impossible) to solve this boundary value problem. In this study, these boundary conditions will be linearised. There are many ways to linearize the free surface boundary condition. One can use the uniform incoming flow to replace the steady flow and the free surface condition is expanded at the undisturbed free surface, the linearised free surface boundary condition is called as the Neumann-Kelvin condition (Newman, 1978). Another approach is to use the steady double body flow as the basis flow and the free surface boundary condition is expanded at the free surface corresponding to the double body flow, see for example, Sclavounos et al. (1993, 2003), Raven (1996), Bertram (1999), Xie et al. (2007). Linearization of the boundary conditions restricts our results to small amplitudes of the motions and the incoming waves, and the steady disturbance flow is small comparing with the incoming uniform flow.

The total velocity potential is split into three components

$$\Phi(x, y, z, t) = \phi_\infty + \phi_s(x, y, z) + \phi_u(x, y, z, t) \tag{5.12}$$

where ϕ_∞ is velocity potential of the incoming uniform flow

$$\phi_\infty = -Ux \tag{5.13}$$

and ϕ_s and ϕ_u are velocity potentials of the steady and unsteady disturbance flows, respectively. It is assumed that the steady flow and unsteady disturbance flow are much less than the incoming uniform flow:

$$\phi_s << \phi_\infty, \qquad \phi_u << \phi_\infty \tag{5.14}$$

The total free surface elevation consists of two parts:

$$\varsigma(x,y,t)=\varsigma_s(x,y)+\varsigma_u(x,y,t) \tag{5.15}$$

where $\varsigma_s(x,y)$ and $\varsigma_u(x,y,t)$ are the free surface elevations of the steady flow and unsteady flow, respectively. Substituting (5.12), (5.13) and (5.15) into the dynamic free surface boundary condition (5.5) and the kinematic free surface boundary condition (5.6), neglecting the higher order terms, the followings are obtained:

$$\frac{\partial\phi_u}{\partial t}-U\left(\frac{\partial\phi_s}{\partial x}+\frac{\partial\phi_u}{\partial x}\right)+g\left(\varsigma_s+\varsigma_u\right)=\begin{cases}-\left(P_0+P\right)/\rho & (x,y)\in S_c\\ 0 & (x,y)\notin S_c\end{cases} \qquad z=\varsigma(x,y,t) \tag{5.16}$$

and

$$\frac{\partial\varsigma_u}{\partial t}-U\frac{\partial\varsigma_s}{\partial x}-U\frac{\partial\varsigma_u}{\partial x}=\frac{\partial\phi_s}{\partial z}+\frac{\partial\phi_u}{\partial z} \qquad z=\varsigma(x,y,t) \tag{5.17}$$

(5.16) and (5.17) are expanded about the undisturbed free surface, $z=0$, separating the steady and unsteady (time-dependent) parts, one obtains: for the steady flow

$$g\varsigma_s-U\frac{\partial\phi_s}{\partial x}=\begin{cases}-P_0/\rho & (x,y)\in S_c\\ 0 & (x,y)\notin S_c\end{cases} \qquad z=0 \tag{5.18}$$

$$U\frac{\partial\varsigma_s}{\partial x}+\frac{\partial\phi_s}{\partial z}=0 \qquad z=0 \tag{5.19}$$

Substituting (5.18) into (5.19), the linearized free surface boundary condition for the steady flow potential is

$$U^2\frac{\partial^2\phi_s}{\partial x^2}+g\frac{\partial\phi_s}{\partial z}=\begin{cases}\dfrac{U}{\rho}\dfrac{\partial P_0}{\partial x} & (x,y)\in S_c\\ 0 & (x,y)\in S_c\end{cases} \qquad z=0 \tag{5.20}$$

For the unsteady flow

$$\frac{\partial\phi_u}{\partial t}-U\frac{\partial\phi_u}{\partial x}+g\varsigma_u=\begin{cases}-P/\rho & (x,y)\in S_c\\ 0 & (x,y)\notin S_c\end{cases} \qquad z=0 \tag{5.21}$$

$$\frac{\partial\varsigma_u}{\partial t}-U\frac{\partial\varsigma_u}{\partial x}-\frac{\partial\phi_u}{\partial z}=0 \qquad z=0 \tag{5.22}$$

Substituting (5.21) into (5.22), the linearized free surface boundary condition for the unsteady flow potential is

$$\frac{\partial^2\phi_u}{\partial t^2}-2U\frac{\partial^2\phi_u}{\partial t\partial x}+U^2\frac{\partial^2\phi_u}{\partial x^2}+g\frac{\partial\phi_u}{\partial z}=\begin{cases}\dfrac{1}{\rho}\left(U\dfrac{\partial P}{\partial x}-\dfrac{\partial P}{\partial t}\right) & (x,y)\in S_c\\ 0 & (x,y)\notin S_c\end{cases} \qquad z=0 \tag{5.23}$$

The body boundary condition (5.8), which is satisfied on the instantaneous hull surface, can be also linearized about the mean hull surface. The unsteady velocity potential consists of potentials of incident wave and other perturbation flows:

$$\phi_u(x,y,z,t) = \phi_I(x,y,z,t) + \phi_p(x,y,z,t) \tag{5.24}$$

It is assumed that the vessel undergoes 3 translational motions $\boldsymbol{\xi} = (q_1, q_2, q_3)$ along $x-$, $y-$ and $z-$axes, respectively; and 3 rotational motions $\boldsymbol{\theta} = (q_4, q_5, q_6)$ about these axes, the hull boundary condition (5.8) can be written as

$$\frac{\partial \phi_u}{\partial n} = -\mathbf{w}\cdot\mathbf{n} - \frac{\partial \phi_I}{\partial n} + \sum_{j=1}^{6} \dot{q}_j n_j \qquad \text{on } S(t) \tag{5.25}$$

where ϕ_I is velocity potential of the incident wave, and $\mathbf{w}$ is velocity distribution of the steady flow

$$\mathbf{w} = \nabla\phi_\infty + \nabla\phi_s \qquad \text{on } S(t) \tag{5.26}$$

and

$$\begin{cases} \mathbf{n} = (n_1, n_2, n_3) \\ \mathbf{r}\times\mathbf{n} = (n_4, n_5, n_6) \end{cases} \tag{5.27}$$

The local displacements of a point on the instantaneous wetted hull surface $S(t)$ due to the translational and rotational motions with respect to the mean hull surface, S_0, is

$$\boldsymbol{\alpha} = \boldsymbol{\xi} + \boldsymbol{\theta}\times\mathbf{r} \tag{5.28}$$

where $\mathbf{r}$ is position vector of the point at the body fixed system. Under the assumption of small amplitude of vessel motions, velocity of the steady flow is expanded at the mean hull position:

$$\mathbf{w}\big|_{S(t)} \approx \left\{\mathbf{w} + (\boldsymbol{\alpha}\cdot\nabla)\mathbf{w}\right\}\big|_{S_0} \tag{5.29}$$

On the other hand, the instantaneous hull surface $S(t)$ is reached from the mean position by 3 translating motions $\boldsymbol{\xi} = (q_1, q_2, q_3)$ and 3 rotating motions $\boldsymbol{\theta} = (q_4, q_5, q_6)$. The translating motions of the ship will not change the hull surface normal vector, whilst the rotating motions will. It is assumed that

$$\mathbf{n}\big|_{S_0} = n_x\mathbf{i}_b + n_y\mathbf{j}_b + n_z\mathbf{k}_b \tag{5.30}$$

where $\mathbf{i}_b, \mathbf{j}_b, \mathbf{k}_b$ are the unit vectors of the body fixed coordinate system. When the ship has a roll motion, q_4, the new unit vectors are

$$\begin{cases} \mathbf{i}_b^{'} = \mathbf{i}_b \\ \mathbf{j}_b^{'} = \cos q_4 \mathbf{j}_b + \sin q_4 \mathbf{k}_b \\ \mathbf{k}_b^{'} = -\sin q_4 \mathbf{j}_b + \cos q_4 \mathbf{k}_b \end{cases} \tag{5.31}$$

Under the assumption of small amplitude motion, (5.31) becomes

$$\begin{pmatrix} \mathbf{i}_b' \\ \mathbf{j}_b' \\ \mathbf{k}_b' \end{pmatrix} \approx \begin{pmatrix} 1 & 0 & 0 \\ 0 & 1 & q_4 \\ 0 & -q_4 & 1 \end{pmatrix} \begin{pmatrix} \mathbf{i}_b \\ \mathbf{j}_b \\ \mathbf{k}_b \end{pmatrix} \tag{5.32}$$

By using the same procedure for pitch (q_5) and yaw (q_6) motions, the following relationship can be obtained:

$$\mathbf{n}(t)\big|_{S(t)} \approx (\mathbf{n} + \boldsymbol{\theta} \times \mathbf{n})\big|_{S_0} \tag{5.33}$$

Substituting (5.29) and (5.33) into (5.25), neglecting the higher order terms, the hull boundary conditions are as follows. For the steady flow

$$\frac{\partial \phi_s}{\partial n} = -\frac{\partial \phi_\infty}{\partial n} = U n_1 \qquad \text{on } S_0 \tag{5.34}$$

And for the unsteady flow

$$\frac{\partial \phi_P}{\partial n} = -\frac{\partial \phi_I}{\partial n} + \sum_{j=1}^{6} \left[\dot{q}_j n_j + U q_j m_j \right] \qquad \text{on } S_0 \tag{5.35}$$

where

$$(m_1, m_2, m_3) = -\frac{1}{U} (\mathbf{n} \cdot \nabla) \mathbf{w} \tag{5.36}$$

$$(m_4, m_5, m_6) = -\frac{1}{U} (\mathbf{n} \cdot \nabla)(\mathbf{r} \times \mathbf{w}) \tag{5.37}$$

5.3 Force, Moment and Equations of the Motions

Once the velocity potentials have been solved and the pressure distribution around the vessel hull has been obtained, it is possible to calculate the forces/moments acting on the vessel. There are two components of force acting on the hull surface: the excess pressure force in the cushion chambers and the hydrodynamic pressure forces on the wetted rigid side hulls.

$$F_{t,j} = \iint_{\Omega(t)} (P_0 + P) n_j ds + \iint_{S(t)} p n_j ds \qquad j = 1, 2, ..., 6 \tag{5.38}$$

where $\Omega(t)$ is the instantaneous cushion chamber surface. Under assumption of small amplitude motions for the vessel, (5.38) is expanded at the mean hull surface position.

$$(P_0 + P)\big|_{\Omega(t)} \approx (P_0 + P)\big|_{\Omega_0} + (\boldsymbol{\alpha} \cdot \nabla)(P_0)\big|_{\Omega_0} \tag{5.39}$$

$$p\big|_{S(t)} \approx p\big|_{S_0} + (\alpha \cdot \nabla) p\big|_{S_0} \tag{5.40}$$

where Ω_0 is the mean cushion chamber surface and S_0 is the mean wetted rigid hull surface. Substituting (5.39) and (5.40) into (5.38), and also making use of (5.33), the forces/moments acting on the vessel can be calculated up to the first order as

$$F_{t,j} \approx F_j^0 + F_j(t) \qquad j = 1, 2, ..., 6 \tag{5.41}$$

The steady force/moments are

$$F_j^0 = \iint_{\Omega_0} P_0 n_j ds + \iint_{S_0} p_s n_j ds \tag{5.42}$$

where p_s is the steady hydrodynamic pressure distribution

$$p_s = \frac{1}{2}\rho\left[\mathbf{w}\cdot\mathbf{w} - U^2\right] + \rho g z \tag{5.43}$$

Due to symmetry of the hull, the non-zero steady forces and moments are longitudinal force (wave-making resistance), vertical (sinkage) force and trim moment, i.e., for $j = 1, 3, 5$.

The unsteady forces/moments also consist of two components: the excess air pressure in the cushion chambers and the hydrodynamic pressure on the rigid side hulls. For the force/moment due to the excess air pressure:

$$\begin{pmatrix} F_{p,1} \\ F_{p,2} \\ F_{p,3} \end{pmatrix} = A_c \begin{pmatrix} 0 \\ 0 \\ \sum_l P_l \end{pmatrix} \tag{5.44}$$

$$\begin{pmatrix} F_{p,4} \\ F_{p,5} \\ F_{p,6} \end{pmatrix} = P_0 h_0 A_c \begin{pmatrix} q_4 \\ q_5 \\ 0 \end{pmatrix} + \begin{pmatrix} \sum_l y_{cl} A_c P_l \\ \sum_l x_{cl} A_c P_l \\ 0 \end{pmatrix} \tag{5.45}$$

where l is cushion chamber index, (x_{cl}, y_{cl}, z_{cl}) is the cushion pressure centre. A_c is cushion area for the demi-hull. The forces/moments due to the hydrodynamic pressure can be calculated in a similar way

$$F_{w,j} = \iint_{S_0} p_w n_j ds - \rho g \iint_{S_0} (q_3 + y q_4 - x q_5) n_j ds \tag{5.46}$$

$j = 1, 2, ..., 6$, where the first order hydrodynamic pressure distribution is

$$p_w = -\rho \frac{\partial \phi_u}{\partial t} - \rho\, \mathbf{w} \cdot \nabla \phi_u \tag{5.47}$$

The second term in (5.46) is the hydrostatic restoring force/moment, and can be further calculated as:

$$F_{s,3} = -\rho g A_{wl} q_3 + [\rho g \iint_{wp} x dx dy] q_5 \tag{5.48}$$

$$F_{s,4} = -\rho g [\iint_{wp} y^2 dx dy + \forall z_B]\, q_4 \tag{5.49}$$

$$F_{s,5} = \rho g [\iint_{wp} x dx dy]\, q_3 - \rho g [\iint_{wp} x^2 dx dy + \forall z_B]\, q_5 \tag{5.50}$$

where $\forall$ is the displacement volume; z_B is vertical centre of buoyancy. Substituting (5.47) into (5.46), the hydrodynamic forces and moments are

$$F_{H,j} = -\rho \iint_{S_0} \frac{\partial \phi_u}{\partial t} n_j ds - \rho \iint_{S_0} (\mathbf{w} \cdot \nabla \phi_u) n_j ds \tag{5.51}$$

Since the origin of coordinate system is located on the undisturbed free surface, not at the centre of gravity of the vessel, there will non-zero components due to gravity force:

$$F_{g,j} = mgz_g q_j \qquad\qquad j = 4, 5 \tag{5.52}$$

The total velocity potential of the unsteady flow consists of the velocity potentials of the incident wave, the diffraction wave and the 6 radiation waves. The velocity potential of the incident wave in the translating frame can be written as (Newman, 1978)

$$\phi_I(x, y, z, t) = \mathrm{Re}\left\{\varsigma_a \phi_0(x, y, z) e^{i\sigma t}\right\} \tag{5.53}$$

where ς_a is amplitude of the incident wave; ϕ_0 is the complex amplitude of velocity potential of the incident wave in the translating frame:

$$\phi_0(x, y, z) = \frac{ig}{\omega} e^{kz} e^{-ik(x\cos\beta + y\sin\beta)} \tag{5.54}$$

where $\omega^2 = gk$. The velocity potential of the diffraction wave is expressed as

$$\phi_D(x, y, z, t) = \mathrm{Re}\left\{\varsigma_a \phi_7(x, y, z) e^{i\sigma t}\right\} \tag{5.55}$$

where ϕ_7 is the complex amplitude of the velocity potential in space for the diffraction wave. The vessel motions are expressed as

$$q_j(t) = \mathrm{Re}\left\{\eta_j e^{i\sigma t}\right\} \tag{5.56}$$

where η_j, $j = 1, 2, \ldots, 6$, are the complex amplitudes of the vessel motions. The velocity potential of the radiation wave for the j^{th} motion mode is expressed as

$$\phi_{r,j}(x,y,z,t) = \mathrm{Re}\left\{\eta_j \phi_j(x,y,z) e^{i\sigma t}\right\} \tag{5.57}$$

where $\phi_j, j = 1,2,...,6$ are the complex amplitude in space of the velocity potentials for the radiation waves.

In summary, the total unsteady velocity potential can be written as:

$$\phi_u(x,y,z,t) = \mathrm{Re}\{[\varsigma_a\left(\phi_0(x,y,z)+\phi_7(x,y,z)\right)+\sum_{j=1}^{6}\eta_j\phi_j(x,y,z)]e^{i\sigma t}\} \tag{5.58}$$

Substituting (5.56) and (5.58) into (5.51), the integrated unsteady forces/moments relating to the incident and diffraction waves are the wave exciting forces/moment, whilst the integrated forces/moments relating to the radiation waves are the added mass and damping coefficient. The total velocity potential of the radiation waves is:

$$\phi_R(x,y,z,t) = \sum_{k=1}^{6}\phi_{r,k}(x,y,z,t) = \sum_{k=1}^{6}\mathrm{Re}\left\{\eta_k\phi_k(x,y,z)e^{i\sigma t}\right\} \tag{5.59}$$

Substituting (5.59) into (5.51), the j^{th} component of the unsteady forces relating to the radiation wave is

$$F_{R,j} = -\rho\iint_{S_0}\frac{\partial\phi_R}{\partial t}n_j ds - \rho\iint_{S_0}(\mathbf{w}\cdot\nabla\phi_R)n_j ds \tag{5.60}$$

From (5.59)

$$\frac{\partial\phi_R}{\partial t} = \mathrm{Re}\{i\sigma\sum_{k=1}^{6}\eta_k\phi_k e^{i\sigma t}\} \tag{5.61}$$

$$\nabla\phi_R = \mathrm{Re}\{\sum_{k=1}^{6}\eta_k\nabla\phi_k e^{i\sigma t}\} \tag{5.62}$$

Substituting (5.61) and (5.62) into (5.60):

$$F_{R,j} = -\rho\,\mathrm{Re}\{\sum_{k=1}^{6}\eta_k[i\sigma\iint_{S_0}\phi_k n_j ds]e^{i\sigma t}\} - \rho\,\mathrm{Re}\{\sum_{k=1}^{6}\eta_k[\iint_{S_0}(w\cdot\nabla\phi_k)n_j ds]e^{i\sigma t}\} \tag{5.63}$$

Normally, the radiation forces are expressed as

$$F_{R,j}(t) = \sum_{k=1}^{6}\left[-A_{jk}\ddot{q}_k - B_{jk}\dot{q}_k\right] \tag{5.64}$$

where A_{jk} and B_{jk} are the added mass and damping coefficients, respectively. Comparing (5.63) and (5.64), and using equation (5.56), the added mass and damping coefficients are calculated as:

$$A_{jk} = -\frac{\rho}{\sigma^2}\mathrm{Re}\left\{\iint_{S_0} i\sigma\phi_k n_j ds + \iint_{S_0} (w\cdot\nabla\phi_k)n_j ds\right\} \tag{5.65}$$

$$B_{jk} = \frac{\rho}{\sigma}\mathrm{Im}\left\{\iint_{S_0} i\sigma\phi_k n_j ds + \iint_{S_0} (w\cdot\nabla\phi_k)n_j ds\right\} \tag{5.66}$$

By using Newton's law, the equations of motions for the vessel in wave can be written as

$$[\mathbf{M}+\mathbf{A}][\ddot{\mathbf{q}}] + [\mathbf{B}][\dot{\mathbf{q}}] + [\mathbf{C}][\mathbf{q}] = [\mathbf{F}_w] + [\mathbf{F}_p] \tag{5.67}$$

where the mass matrix $[\mathbf{M}]$ is

$$[\mathbf{M}] = \begin{bmatrix} m & 0 & 0 & 0 & mz_g & 0 \\ 0 & m & 0 & -mz_g & 0 & 0 \\ 0 & 0 & m & 0 & 0 & 0 \\ 0 & -mz_g & 0 & I_{44} & 0 & I_{46} \\ mz_g & 0 & 0 & 0 & I_{55} & 0 \\ 0 & 0 & 0 & I_{64} & 0 & I_{66} \end{bmatrix} \tag{5.68}$$

where m is mass of the vessel; z_g is vertical coordinate of centre of gravity; I_{jk} is the inertia moment:

$$I_{44} = \iiint (y^2+z^2)dm \qquad I_{55} = \iiint (x^2+z^2)dm \tag{5.69}$$

$$I_{66} = \iiint (x^2+y^2)dm \qquad I_{46} = \iiint (xy)dm = I_{64} \tag{5.70}$$

The non-zero restoring matrix coefficients are

$$C_{33} = \rho g A_{wp} \tag{5.71}$$

$$C_{35} = C_{53} = -\rho g \iint_{wp} xdxdy \tag{5.72}$$

$$C_{44} = \rho g[\iint_{wp} y^2 dxdy + \forall z_B] - mgz_g \tag{5.73}$$

$$C_{55} = \rho g[\iint_{wp} x^2 dxdy + \forall z_B] - mgz_g \tag{5.74}$$

where wp is the water plane. The air excess forces/moments are calculated by (5.44) and (5.45).

Chapter 6 The Three Dimensional Steady Flow Problem

This Chapter describes the three dimensional steady flow problem of a pressure patch moving on the free surface. Numerical calculation and behaviour of the elementary solution of a rectangular pressure patch is studied in detail. A reliable and effective numerical approach has been presented.

6.1 Solution of the Boundary Value Problem

Assuming a pressure distribution, $\Pi(\xi,\eta)$, is moving on a calm water surface with speed, U. The flow field is solved by velocity potential theory. Velocity potential of the steady flow is split into velocity potentials of the incoming uniform flow and the disturbance flow:

$$\Phi_s(x,y,z) = \phi_\infty(x,y,z) + \phi_s(x,y,z) \tag{6.1}$$

where ϕ_∞ and ϕ_s are velocity potentials of the incoming uniform flow and the steady disturbance flow, respectively, and

$$\phi_\infty = -Ux \tag{6.2}$$

It is assumed that the disturbance flow is small comparing with the incoming uniform flow: $\phi_s << \phi_\infty$, the velocity potential of the disturbance flow satisfies Laplace equation in the fluid domain:

$$\frac{\partial^2\phi_s}{\partial x^2} + \frac{\partial^2\phi_s}{\partial y^2} + \frac{\partial^2\phi_s}{\partial z^2} = 0 \tag{6.3}$$

On the free surface, the velocity potential of the disturbance flow and the free surface elevation, $\varsigma_s(x,y)$, satisfy the linearized kinematic and dynamic boundary conditions:

$$U\frac{\partial\varsigma_s}{\partial x} + \frac{\partial\phi_s}{\partial z} = 0 \qquad \text{on } z = 0 \tag{6.4}$$

$$\frac{\Pi(x,y)}{\rho} + g\varsigma_s(x,y) - U\frac{\partial\phi_s}{\partial x} = 0 \qquad \text{on } z = 0 \tag{6.5}$$

On the sea bottom and far field upstream:

$$\nabla\phi_s = 0 \qquad z \to -\infty \tag{6.6}$$

$$\nabla\phi_s = 0 \qquad x \to +\infty \tag{6.7}$$

The boundary value problem formulated in (6.3) – (6.7) for the steady disturbance flow is solved by Laplace transformation method, and can be expressed as (Wehausen and Laitone, 1960)

$$\phi_s(x,y,z)=\frac{1}{\pi^2\rho U}\iint_{S_c}\Pi(\xi,\eta)d\xi d\eta\int_0^{\pi/2}d\theta\sec\theta\ \text{P.V.}\int_0^{\infty}\frac{ke^{kz}}{k-k_0\sec^2\theta}\sin[k(x-\xi)\cos\theta]\cos[k(y-\eta)\sin\theta]dk$$
$$+\frac{k_0}{\pi\rho g}\iint_{S_c}\Pi(\xi,\eta)d\xi d\eta\int_0^{\pi/2}\sec^3\theta e^{k_0\sec^2\theta}\cos[k_0(x-\xi)\sec\theta]\cos[k_0(y-\eta)\sec^2\theta\sin\theta]d\theta \qquad (6.8)$$

where S_c is the area on which the pressure is applied and $k_0=g/U^2$ is the wave number. Π is the pressure distribution and defined as:

$$P_0(x,y,0)=\begin{cases}\Pi(x,y) & (x,y)\in S_c\\ 0 & (x,y)\notin S_c\end{cases} \qquad (6.9)$$

The expression of the free surface elevation, $\varsigma_s(x,y)$, can be obtained by substituting velocity potential (6.8) into the dynamic free surface condition (6.5):

$$\varsigma_s(x,y)=\frac{1}{\pi^2\rho U}\iint_{S_c}\Pi(\xi,\eta)d\xi d\eta\int_0^{\pi/2}d\theta\sec\theta\ \text{P.V.}\int_0^{\infty}\frac{k^2}{k-k_0\sec^2\theta}\cos[k(x-\xi)\cos\theta]\cos[k(y-\eta)\sin\theta]dk$$
$$+\frac{k_0^2}{\pi\rho g}\iint_{S_c}\Pi(\xi,\eta)d\xi d\eta\int_0^{\pi/2}\frac{\sin[k_0(x-\xi)\sec\theta]\cos[k_0(y-\eta)\sec^2\theta\sin\theta]}{\cos^4\theta}d\theta-\frac{P_0(x,y)}{\rho g} \qquad (6.10)$$

The application of (6.10) lies on two fronts: firstly, one can use this expression to predict the wave field generated by a known pressure distribution, $\Pi(\xi,\eta)$, moving on the free surface. This is of practical interest in predicting wash waves of high speed craft such as ACV, SES and ASV. The wash wave of high speed craft could be potentially damaging to the environment of the shore lines and dangerous to swimmers in the tourist attractions. Secondly, if the free surface elevation, $\varsigma_s(x,y)$, is known, the pressure distribution over the wetted hull surface can be predicted by solving the integral equation. Both of the above problems will be investigated in the present study.

6.2 Numerical Method for a Rectangular Pressure Patch

Several methods of discretisation have been proposed for numerical calculation of (6.10). Cheng and Wellicome (1994) divided the pressure applied area into a number of transverse strips, the pressure along the span of a strip is expressed by a sine series

$$p(y) = \sum_{n=1}^{N} A_n \sin\left[\frac{n\pi}{2B}(y + 0.5B)\right] \tag{6.11}$$

where B is the width of the pressure applied area, A_n are the coefficients.

Doctors (1975), Wang and Day (2007) discretize the pressure applied area into rectangular elements, the pressure strength over each element is represented with a pyramid shape:

$$p(\xi,\eta) = p_0\left(1 - \frac{|\xi|}{a}\right)\left(1 - \frac{|\eta|}{b}\right) \tag{6.12}$$

where $-a \le \xi \le a;\ -b \le \eta \le b$, and $a,\ b$ are the half length and beam of the panel, respectively, p_0 is constant for each panel. The continuity of the pressure strength at the edges of each element will be maintained with the discretisation in (6.12). The mathematical formulation of the analytic solution for each of the pyramidal pressure element is more complex than its counterpart of the constant pressure element, Doctors (1975).

In the present study, the cushion area, S_c, is divided into a number of rectangular panels, ΔS_i, as well, but the pressure strength over each panel is assumed to be constant, see Figure 6.1. The total free surface elevation at a field point is sum of the contributions from all of the rectangular pressure patches:

$$\varsigma_s(x_i, y_i) = \sum_{j=1}^{N} p(\xi_j, \eta_j)\tilde{D}_{ji} \tag{6.13}$$

where $\tilde{D}_{ji}$ is called as the influence coefficient at field point (x_i, y_i) by a pressure element located at (ξ_j, η_j) with unit pressure strength.

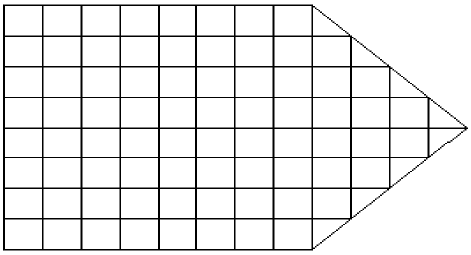

Figure 6.1 Discretization of the pressure applied area

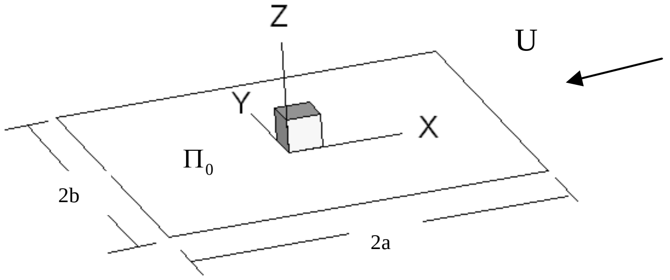

Figure 6.2 Definition of a rectangular pressure element, ΔS

The solution of a rectangular pressure patch with constant pressure strength is the elementary solution of the problem. Figure 6.2 shows a rectangular pressure element on the free surface. Without losing generality, one can assume

$$P_0(x,y)=\begin{cases}\Pi_0 & |x-\xi|\le a, |y-\eta|\le b\\ 0 & |x-\xi|> a, |y-\eta|> b\end{cases} \tag{6.14}$$

where Π_0 is the pressure strength and is a constant; a and b are half length and beam of the rectangular patch, respectively. The free surface elevation at a field point (x_j, y_j) induced by a pressure element of unit strength located on (ξ_i, η_i) can be expressed as (Kim and Tsakonas, 1980)

$$\tilde{D}_{ji}=-\frac{\delta_{ji}}{\rho g}-\frac{1}{2\pi^2\rho g}\sum_{m=1}^{8}(-1)^{m+1}\operatorname{Re}\left\{\int_0^{\pi/2}\frac{\exp[ik_0\sec^2\theta s_m(\theta)]}{\sin\theta\cos\theta}\times[E_1(ik_0\sec^2\theta s_m(\theta))-i\pi(1-\operatorname{sgn}(s_m))]d\theta\right\} \tag{6.15}$$

where

$$\delta_{ji}=\begin{cases}1 & (x,y)\text{ is inside }\Delta\mathrm{S_i}\\ 0.5 & (x,y)\text{ is on the boundary of }\Delta\mathrm{S_i}\\ 0.25 & (x,y)\text{ is at the corner of }\Delta\mathrm{S_i}\\ 0 & (x,y)\text{ is outside }\Delta\mathrm{S_i}\end{cases} \tag{6.16}$$

and $s_m(\theta), m=1,2,...,8$, are the distance scales defined as

$$\begin{aligned}
s_1&=(x_j-\xi_i-a)\cos\theta+(y_j-\eta_i-b)\sin\theta\\
s_2&=(x_j-\xi_i-a)\cos\theta+(y_j-\eta_i+b)\sin\theta\\
s_3&=(x_j-\xi_i+a)\cos\theta+(y_j-\eta_i+b)\sin\theta\\
s_4&=(x_j-\xi_i+a)\cos\theta+(y_j-\eta_i-b)\sin\theta\\
s_5&=(x_j-\xi_i-a)\cos\theta-(y_j-\eta_i+b)\sin\theta\\
s_6&=(x_j-\xi_i-a)\cos\theta-(y_j-\eta_i-b)\sin\theta\\
s_7&=(x_j-\xi_i+a)\cos\theta-(y_j-\eta_i-b)\sin\theta\\
s_8&=(x_j-\xi_i+a)\cos\theta-(y_j-\eta_i+b)\sin\theta
\end{aligned} \tag{6.17}$$

An example of the definitions for $s_1(\theta)$ is shown in Figure 6.3, where the index of j,i are omitted. In this example, the pressure source panel is located at point $P(\xi,\eta)$ and the field point is located at $Q(x,y)$. Distance between point A and B is $\overline{AB} = (x-\xi-a)$ and distance between point B and Q is $\overline{BQ} = (y-\eta-b)$. The angular variable is θ. The projection of $\overline{AB}$ on the ray line is $\overline{AC} = (x-\xi-a)\cos\theta$, and projection of $\overline{BQ}$ on the ray line is $\overline{DQ} = (y-\eta-b)\sin\theta$. $s_1(\theta)$ is the sum of these two projections:

$$s_1(\theta) = \overline{AC} + \overline{DQ} = (x-\xi-a)\cos\theta + (y-\eta-b)\sin\theta \tag{6.18}$$

Similar definitions can be found for other $s_m(\theta)$.

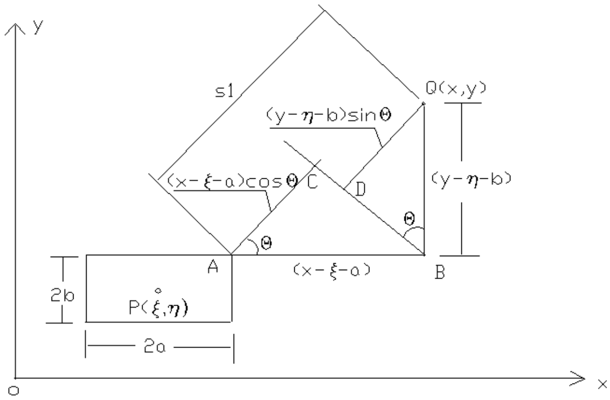

Figure 6.3 Definition of $s_1(\theta)$

$E_1(\bullet)$ in (6.15) is the exponential integral (Abramowtiz and Stegun,1970):

$$E_1(w) = \int_0^\infty \frac{e^{-(t+w)}}{t+w}dt \tag{6.19}$$

There is also a series expression for this integral

$$E_1(w) = -\gamma - \ln(w) - \sum_{n=1}^{\infty} \frac{(-1)^n w^n}{n \cdot n!} \tag{6.20}$$

where $\gamma = 0.5772...$ is the Euler's constant. (6.15) is rewritten as

$$\tilde{D}_{ji} = -\frac{\delta_{ji}}{\rho g} - \frac{1}{2\pi^2 \rho g} \sum_{m=1}^{8} (-1)^{m+1} \operatorname{Re}(J_{1m} + J_{2m}) \tag{6.21}$$

where

$$J_{1m} = \int_0^{\pi/2} \frac{\exp[ik_0 \sec^2\theta s_m(\theta)]}{\sin\theta\cos\theta} E_1(ik_0 \sec^2\theta s_m(\theta))d\theta \tag{6.22}$$

$$J_{2m} = -i\pi \int_{0}^{\pi/2} \frac{\exp[ik_0 \sec^2\theta s_m(\theta)]}{\sin\theta\cos\theta}[1-\mathrm{sgn}(s_m)]d\theta \tag{6.23}$$

for $m = 1, 2, ..., 8$. The main difficulties in numerical calculation for J_{1m} in (6.22) and J_{2m} in (6.23) are the singularities in the integrands and the highly oscillatory behaviour. It can be seen that the integrands in (6.23) have highly oscillatory behaviour when θ approaches $\pi/2$.

A commonly used method is to make a variable change of

$$u = \tan\theta \tag{6.24}$$

to stretch the dimension in the fast oscillatory region, see for example, Doctors, 1975, Wang and Day, 2007. With this variable transformation, one has ($m = 1$)

$$t_1 = k_0 \sec^2\theta s_1(\theta) = k_0(x-\xi-a)\sqrt{1+u^2} + k_0(y-\eta-b)u\sqrt{1+u^2} \tag{6.25}$$

$$J_{21} = -i\pi \int_{0}^{\infty} \frac{\exp(it_1)}{u}[1-\mathrm{sgn}(s_1)du \tag{6.26}$$

It can be seen from (6.26) that the integrand is highly oscillatory with monotonically decay amplitude when $u \to \infty$ (i.e., $\theta \to \pi/2$). The convergence of (6.26) at the upper limit is complicated by the fact that

$$t_1 \to k_0(y-\eta-b)u^2 \qquad \text{as} \quad u \to \infty \tag{6.27}$$

The oscillating behaviour will depends on the vessel speed (i.e., k_0), the relative location between the field point and source point ($y-\eta$) and size of the pressure element (b) as well. It will be difficult to calculate this integral with a high accuracy. Numerical tests indicate that the evaluation of the induced coefficients requires high accuracy in order to obtain accurate hydrodynamic pressure distribution for the planing hulls.

In the present study, the following variable change is introduced to stretch the highly oscillatory behaviour of the integrands:

$$u = \begin{cases} |\gamma| \dfrac{\sin\theta}{\cos^2\theta} & m = 1, 4, 6, 7 \\ |\delta| \dfrac{\sin\theta}{\cos^2\theta} & m = 2, 3, 5, 8 \end{cases} \tag{6.28}$$

where $\gamma = k_0(y-b), \delta = k_0(y+b)$, $\gamma \neq 0, \delta \neq 0$. By doing this, the integrands in (6.22) and (6.23) are stretched:

$$J_{1m} = \mathrm{Re}[\int_0^{\pi/2} \frac{\exp(ik_0 \sec^2\theta s_m(\theta))}{\sin\theta\cos\theta} E_1(ik_0 \sec^2\theta s_m(\theta))d\theta] = \int_0^\infty F_{1m}(u)du \tag{6.29}$$

$$J_{2m} = \mathrm{Re}\{-i\pi \int_0^{\pi/2} \frac{\exp(ik_0 \sec^2\theta s_m(\theta))}{\sin\theta\cos\theta} [1-\mathrm{sgn}(s_m(\theta))]d\theta\} = \int_0^\infty F_{2m}(u)du \tag{6.30}$$

where

$$F_{1m}(u) = \mathrm{Re}\{\frac{2ue^{it_m(u)}E_1(it_m)}{4u^2+\gamma^2-|\gamma|\sqrt{4u^2+\gamma^2}}\} \qquad m = 1,4,6,7 \tag{6.31}$$

$$F_{1m}(u) = \mathrm{Re}\{\frac{2ue^{it_m(u)}E_1(it_m)}{4u^2+\delta^2-|\delta|\sqrt{4u^2+\delta^2}}\} \qquad m = 2,3,5,8 \tag{6.32}$$

$$F_{2m}(u) = \mathrm{Re}\{-2\pi i \frac{ue^{it_m(u)}[1-\mathrm{sgn}(t_m)]}{4u^2+\gamma^2-|\gamma|\sqrt{4u^2+\gamma^2}}\} \qquad m = 1,4,6,7 \tag{6.33}$$

$$F_{2m}(u) = \mathrm{Re}\{-2\pi i \frac{ue^{it_m(u)}[1-\mathrm{sgn}(t_m)]}{4u^2+\delta^2-|\delta|\sqrt{4u^2+\delta^2}}\} \qquad m = 2,3,5,8 \tag{6.34}$$

where

$$t_m(u) = \begin{cases} \dfrac{\sqrt{2}\alpha u}{G_1} + \dfrac{\gamma}{|\gamma|}u & m = 1 \\ \dfrac{\sqrt{2}\beta u}{G_1} + \dfrac{\gamma}{|\gamma|}u & m = 4 \\ \dfrac{\sqrt{2}\alpha u}{G_1} - \dfrac{\gamma}{|\gamma|}u & m = 6 \\ \dfrac{\sqrt{2}\beta u}{G_1} - \dfrac{\gamma}{|\gamma|}u & m = 7 \end{cases} \tag{6.35}$$

$$t_m(u) = \begin{cases} \dfrac{\sqrt{2}\alpha u}{G_2} + \dfrac{\delta}{|\delta|}u & m = 2 \\ \dfrac{\sqrt{2}\beta u}{G_2} + \dfrac{\delta}{|\delta|}u & m = 3 \\ \dfrac{\sqrt{2}\alpha u}{G_2} - \dfrac{\delta}{|\delta|}u & m = 5 \\ \dfrac{\sqrt{2}\beta u}{G_2} - \dfrac{\delta}{|\delta|}u & m = 8 \end{cases} \tag{6.36}$$

where $G_1 = \sqrt{|\gamma|\sqrt{4u^2+\gamma^2}-\gamma^2}$, $G_2 = \sqrt{|\delta|\sqrt{4u^2+\delta^2}-\delta^2}$, $\alpha = k_0(x-a)$ and $\beta = k_0(x+a)$. It can be seen that the highly oscillatory behaviour of the integrands has been eliminated as $u \to \infty$ (i.e., $\theta \to \pi/2$), in fact, $t_m(u) \to \pm u$ as $u \to \infty$. The integrals in

(6.29) and (6.30) have a logarithmic singularity at lower limit of $u = 0$, however, when summing up all the 8 terms together, it will be regular. In fact, the integrands will have the following property:

$$\begin{cases} \lim\limits_{u \to 0} \dfrac{2u}{4u^2 + \gamma^2 - |\gamma|\sqrt{4u^2 + \gamma^2}} / \dfrac{1}{u} = 1 \\ \lim\limits_{u \to 0} \dfrac{2u}{4u^2 + \delta^2 - |\delta|\sqrt{4u^2 + \delta^2}} / \dfrac{1}{u} = 1 \end{cases} \tag{6.37}$$

This singularity can be removed by the following method:

$$J_{1m} = \int_0^\infty \{\frac{2ue^{it_m} E_1(it_m)}{4u^2 + \gamma^2 - |\gamma|\sqrt{4u^2 + \gamma^2}} - \frac{e^{it_m(0)} E_1(it_m(0))}{u}\} du + \int_0^\infty \frac{e^{it_m(0)} E_1(it_m(0))}{u} du \tag{6.38}$$

$$J_{2m} = -i\pi \int_0^\infty \{\frac{2ue^{it_m}[1 - \mathrm{sgn}(t_m)]}{4u^2 + \gamma^2 - |\gamma|\sqrt{4u^2 + \gamma^2}} - \frac{e^{it_m(0)}[1 - \mathrm{sgn}(t_m(0))]}{u}\} du - i\pi \int_0^\infty \frac{e^{it_m(0)}[1 - \mathrm{sgn}(t_m(0))]}{u} du \tag{6.39}$$

for $m = 1, 4, 6, 7$. Similar expressions can be derived for $m = 2, 3, 5, 8$. It can be shown that the second integral in (6.38) and (6.39) have no contribution when they are summarised over all m:

$$\sum_{m=1}^{8} (-1)^m \int_0^\infty \frac{e^{it_m(0)} E_1(it_m(0))}{u} du = 0 \tag{6.40}$$

$$\sum_{m=1}^{8} (-1)^m \int_0^\infty \frac{e^{it_m(0)}[1 - \mathrm{sgn}(t_m(0))]}{u} du = 0 \tag{6.41}$$

The integrands in the first integrals of (6.38) and (6.39) are regular at $u = 0$ (i.e., $\theta = 0$).

The convergence behaviour of (6.29) and (6.30) at the upper limits are analysed as follows. For larger $|w|$, the following asymptotic expression can be used (Abramowitz and Stegun, 1970)

$$e^w E_1(w) = \frac{1}{w} - \frac{1}{w^2} + \frac{2!}{w^3} - \frac{3!}{w^4} + \dots \tag{6.42}$$

Therefore, the first integral in (6.38) is convergent. On the other hand, the integrands in the first integral of (6.39) are oscillatory functions whose amplitudes monotonically decay as $u \to \infty$, thus the convergence can be easily achieved (similar to that of an alternating decay series).

Another singularity problem in the integrals is the logarithmic singularity in the integrands of (6.29), which is equally important for this problem. There will be zero points for

$$t_m(u) = 0 \qquad\qquad m = 1, 2, ..., 8 \tag{6.43}$$

Substituting (6.35) and (6.36) into (6.43), one can get these zero points as:

$$\hat{u}_{1,6} = \frac{|\alpha|\sqrt{\alpha^2+\gamma^2}}{|\gamma|} \tag{6.44}$$

$$\hat{u}_{4,7} = \frac{|\beta|\sqrt{\beta^2+\gamma^2}}{|\gamma|} \tag{6.45}$$

$$\hat{u}_{2,5} = \frac{|\alpha|\sqrt{\alpha^2+\delta^2}}{|\delta|} \tag{6.46}$$

$$\hat{u}_{3,8} = \frac{|\beta|\sqrt{\beta^2+\delta^2}}{|\delta|} \tag{6.47}$$

Theoretically, this singularity is integrable, an accurate integrating scheme is required. In fact, by using Taylor's expansion:

$$t_m(u) = t_m(\hat{u}_m) + t_m^{'}(\hat{u}_m)(u-\hat{u}_m) + ... \tag{6.48}$$

where $t_m^{'}(\hat{u}_m)$ is the first order derivate at zero point of $t_m(u) = 0$, i.e. $t_m(\hat{u}_m) = 0$. On the other hand,

$$E_1(it_m(u)) = -\gamma - \ln(it_m(u)) - \sum_{n=1}^{\infty} \frac{(-1)^n (it_m(u))^n}{n\, n!} \tag{6.49}$$

After keeping up-to the 1st order term:

$$E_1(it_m(u)) \approx -\gamma - \ln[it_m^{'}(\hat{u}_m)(u-\hat{u}_m)] - \sum_{n=1}^{\infty} \frac{(-1)^n [it_m^{'}(\hat{u}_m)(u-\hat{u}_m)]^n}{n\, n!} \tag{6.50}$$

Assuming ε is a small positive real number, for $m = 1, 4, 6, 7$

$$J_{1m}^{\varepsilon} = \int_{\hat{u}_m-\varepsilon}^{\hat{u}_m+\varepsilon} F_{1m}(u)du \approx \frac{2\hat{u}_m}{4\hat{u}_m^2+\gamma^2-|\gamma|\sqrt{4\hat{u}_m^2+\gamma^2}} \int_{\hat{u}_m-\varepsilon}^{\hat{u}_m+\varepsilon} \mathrm{Re}\left[E_1(it_m)\right]du$$

$$\approx \frac{2\hat{u}_m}{4\hat{u}_m^2+\gamma^2-|\gamma|\sqrt{4\hat{u}_m^2+\gamma^2}} \left\{2(1-\gamma)\varepsilon - 2\varepsilon \ln[\varepsilon \cdot \left|t_m^{'}(\hat{u}_m)\right|]\right\} \tag{6.51}$$

It can be seen that $J_{1m}^{\varepsilon} \to 0$ as $\varepsilon \to 0$. The same procedure can be applied for the cases of $m = 2, 3, 5, 8$. Thus, the logarithmic singularity is integrable. Having shown convergence of the integrals in the influence coefficients, the next is to demonstrate a practical and effective method for the evaluation of these coefficients. (6.21) is rewritten as

$$D(x,y) = \rho g\tilde{D}(x,y) = D_1(x,y) + D_2(x,y) \tag{6.52}$$

where

$$D_1(x,y) = -\delta_{ji} - \frac{1}{2\pi^2}\int_0^{u_c} f_1(u)du \tag{6.53}$$

$$D_2(x,y) = -\frac{1}{2\pi^2}\int_0^{u_c} f_2(u)du \tag{6.54}$$

where u_c is the truncated upper limit of the infinite integrals, and

$$f_1(u) = \sum_{m=1}^{8}(-1)^{m+1}F_{1m} \tag{6.55}$$

$$f_2(u) = \sum_{m=1}^{8}(-1)^{m+1}F_{2m} \tag{6.56}$$

In order to calculate the influence coefficients with high accuracy, it may be worth to look at characteristics of the integrands in (6.53) and (6.54). Some of samples of the integrands are shown in Figures 6.4 ~ 6.7. The element length based Froude number is defined as $f_n = U/\sqrt{2ag}$. In Figure 6.4 and Figure 6.6, the major contribution to the integral, D_1, is coming from the regions near the logarithmic singularity points ($\hat{u} \approx 0.01737$ in Figure 6.4, $\hat{u} \approx 6.5401$ and $\hat{u} \approx 7.8446$ in Figure 6.6). The integrands change sharply near these points, the slope also depends on craft speed and the length/beam ratio of the element. An accurate scheme should be used near these regions during the numerical integration: fine steps will be needed in Simpson’s rule or a proper interval in Gaussian quadrature scheme is necessary. In Figures 6.5 and 6.7, the integrands of D_2 show an oscillatory behaviour with monotonic decay amplitude, as it is expected the oscillating period trends to be approximately 2π, see (6.35) and (6.36). A sharp change near $u = 0$ can be observed.

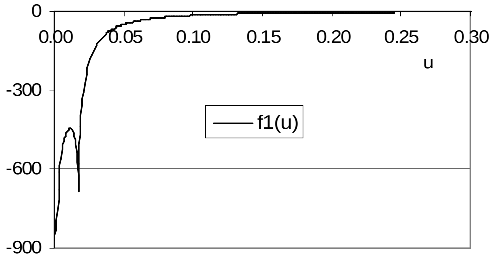

Figure 6.4 Integrand in (6.53) for $a/b = 1.64$, $f_n = 7.429$ at $(x, y) = (0,0)$

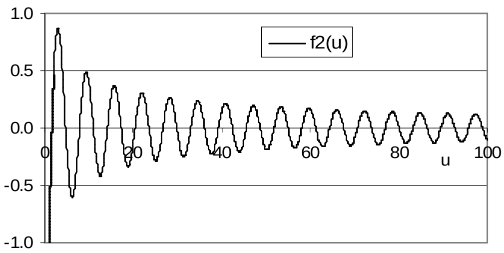

Figure 6.5 Integrand in (6.54) for $a/b = 1.64$, $f_n = 7.429$ at $(x, y) = (0, 0)$

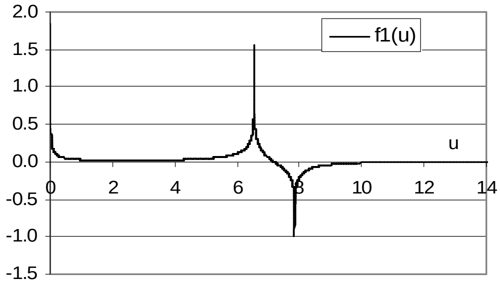

Figure 6.6 Integrand in (6.53) for $a/b = 1.64$, $f_n = 7.429$ at $(x, y) = (-22a, 0)$

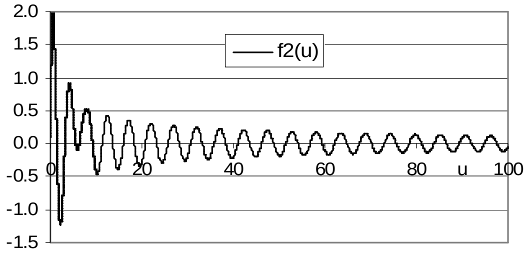

Figure 6.7 Integrand in (6.54) for $a/b = 1.64$, $f_n = 7.429$ at $(x, y) = (-22a, 0)$

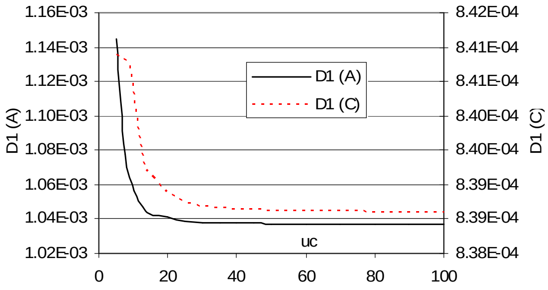

Figure 6.8 Convergence of D_1 for $a/b = 1.64$, $f_n = 7.429$ at field points A ($-11a, 2b$) and C ($-11a, 8b$)

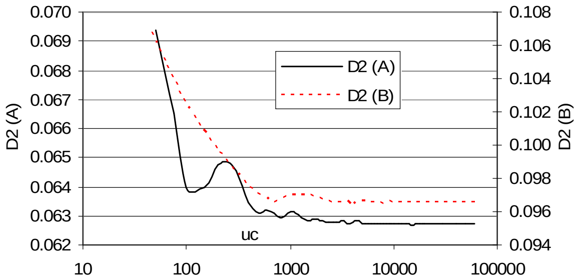

Figure 6.9 Convergence of D_2 for $a/b = 1.64, f_n = 7.429$ at field points A ($-11a, 2b$) and B ($0, 0$)

In the numerical calculations, the infinite integrations in (6.52) are truncated at some upper limits, u_c, as shown in (6.53) and (6.54). Figures 6.8 and 6.9 show examples of convergence of the integrals in (6.53) and (6.54) at three field points: A ($-11a, 2b$), B ($0, 0$) and C ($-11a, 8b$); the pressure panel is located at ($0, 0$) with a length/beam ratio of $a/b = 1.64$ and the panel length based Froude number $f_n = U/\sqrt{2ag} = 7.429$. It can be seen that when truncating at about $u_c = 50$, D_1 is convergent quite well (with 4 digital accuracy), while for D_2, the upper limit (u_c) should be more than 30000 to reach the same accuracy. This means that D_1 converges quicker than D_2. This property is useful for improving efficiency of numerical calculation due to frequent calls of exponential function consumes relatively more computing time. In order to predict the hydrodynamic pressure distribution on the planing hulls, normally, the relative coordinates will need to cover the region of $x = [-L \sim L], y = [-B, B]$, where L is water plane length of the planing hull, while B is the hull beam. The symmetric properties also can be used to save the computing effort. $D_1(x, y)$ is symmetric about $x = 0$ and $y = 0$, i.e., $D_1(x, -y) = D_1(x, y)$, $D_1(-x, y) = D_1(x, y)$, $D_1(-x, -y) = D_1(x, y)$, only values for the first quarter of the domain need to be calculated. On the other hand, $D_2(x, y)$ is symmetric about $x-$ axes: $D_2(x, -y) = D_2(x, y)$, thus only values on the first and second quarters need to be calculated. Figure 6.10 and 6.11 show samples of the influence coefficients.

As mentioned previously, the logarithmic singularity points in $F_{1m}(u)$ also play an important role in the evaluation of the influence coefficients. If there are N_x panels in longitudinal direction and N_y panels in transverse direction (maximum), then $2a = L_w / N_x$, $2b = B / N_y$. The minimum and maximum locations of the logarithmic singularity points will be

$$(\hat{u})_{\min} = \frac{1}{2 f_n^2} \sqrt{1 + \frac{1}{(2N_y + 1)^2} \left(\frac{a}{b} \right)^2} \tag{6.57}$$

$$(\hat{u})_{\max} = \frac{(2N_x + 1)}{2 f_n^2} \sqrt{1 + (2N_x + 1)^2 \left(\frac{a}{b} \right)^2} \tag{6.58}$$

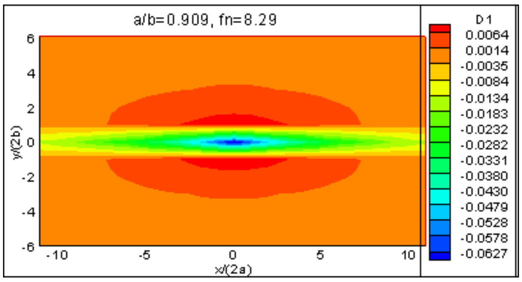

Figure 6.10 Sample of the influence coefficient $D_1(x, y)$

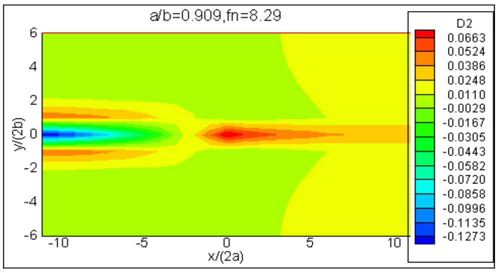

Figure 6.11 Sample of the influence coefficient $D_2(x, y)$

It can be observed from (6.57) that, when the number of the buttocks for a planing craft, N_y, is large; the panel length based Froude number, f_n, is also large as well, thus the minimum value of the singularity point is very small, $\hat{u} \to 0$, which requires a proper integration scheme.

Figure 6.12 shows a comparison of the free surface elevation of a rectangular pressure element with length/beam ratio of $B / L = 1.0$ at $Fn = 0.71$. The wave cut is taken at $y = B / 2 (= b)$. The wave elevation of the present prediction agrees well with that of Kim et al (1981), who adopted a different numerical scheme.

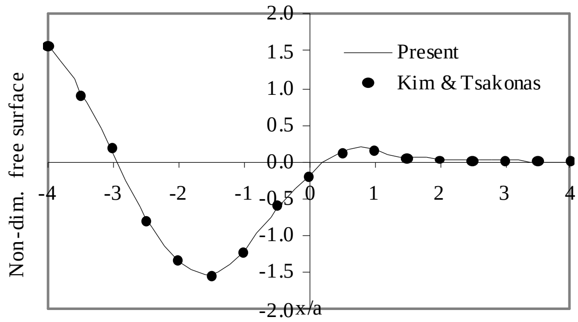

Figure 6.12 Comparison of wave cut at $y = b$, $b/a = 1, Fn = 0.71$

Table 6.1 Sample of the induced coefficients ($b/a = 1.34, fn = 9.04$, x, y are longitudinal and lateral distances to centre of the element, respectively)

y x	0	2b	4b	6b	8b
-7 l	-0.809781E-01	0.267377E-01	0.552860E-02	0.246351E-02	0.143168E-02
-6 l	-0.697273E-01	0.231254E-01	0.481483E-02	0.216792E-02	0.126788E-02
-5 l	-0.582469E-01	0.194874E-01	0.405869E-02	0.185975E-02	0.110599E-02
-4 l	-0.465847E-01	0.157250E-01	0.338853E-02	0.155573E-02	0.952134E-03
-3 l	-0.347012E-01	0.119831E-01	0.265249E-02	0.128658E-02	0.806927E-03
-2 l	-0.227081E-01	0.826154E-02	0.201714E-02	0.104593E-02	0.676633E-03
- l	-0.102581E-01	0.485673E-02	0.139680E-02	0.829829E-03	0.562147E-03
0	0.367811E-02	0.214768E-02	0.988816E-03	0.622272E-03	0.464104E-03
l	0.156091E-02	0.944974E-03	0.661455E-03	0.476320E-03	0.386360E-03
2 l	0.758113E-03	0.576489E-03	0.459877E-03	0.372690E-03	0.322092E-03
3 l	0.510338E-03	0.374945E-03	0.354668E-03	0.312561E-03	0.268896E-03
4 l	0.417445E-03	0.303526E-03	0.240145E-03	0.258015E-03	0.226030E-03
5 l	0.275688E-03	0.231732E-03	0.245897E-03	0.207067E-03	0.189273E-03
6 l	0.170239E-03	0.255575E-03	0.182931E-03	0.166518E-03	0.161186E-03
7 l	0.153567E-03	0.182703E-03	0.181568E-03	0.149332E-03	0.138721E-03

Table 6.1 is an example of the influence coefficients for a pressure element with $b/a = 1.34$, $fn = U/\sqrt{2ag} = 9.04$. A 3-D view is also shown in Figure 6.13. It is observed that the differences between the flow patterns down stream and up stream of the pressure element are significant due to the high element length Froude Number (fn).

In the present constant pressure distribution method, the "self-induced coefficient" is different from that of the conventional source distribution method, in which the self-induced coefficient is 2π (Newman, 1978). Figure 6.14 shows an example of the self-induced coefficients at the central line for a pressure element with length Froude Number $fn = 7.08$ and $b/a = 1.67$, 1.00 and 0.56 respectively. It is observed that the self-induced coefficients change much along the flow direction, especially for the element with lower beam-length ratio. This corresponds to the cases in which more number of buttocks is employed in the prediction of the hydrodynamic pressure distribution. Figure 6.15 shows 3-D view of the self-induced coefficients for an element of $b/a =$ 1.0 at $fn = 7.08$.

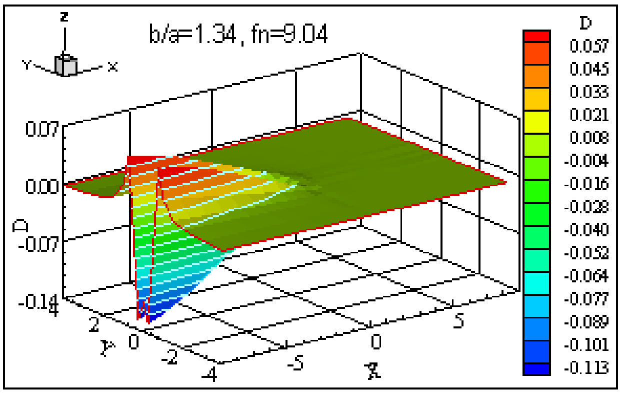

Figure 6.13 3-D view of the induced coefficients of a pressure element ($X = x/2a; Y = y/2b$, $fn = U/\sqrt{2ag}$)

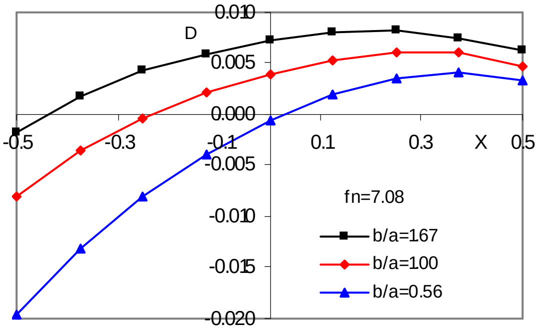

Figure 6.14 Sample of pressure element self-induced coefficients at central line ($X = x/2a$)

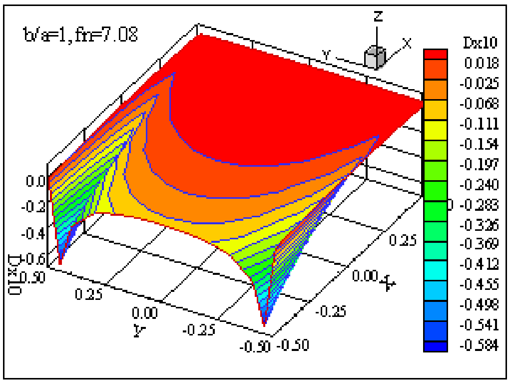

Figure 6.15 Sample of the self-induced coefficients of a element ($X = x/2a$; $Y = y/2b$)

6.3 Summary

In this chapter, a mathematical model for solving the steady potential flow of a pressure patch moving on the free surface is presented. An effective and efficient numerical method is proposed to tackle the singularity and high oscillation problem in calculation of the elementary solution of the free surface elevation resultant from a pressure patch moving on the free surface. The numerical scheme has the advantages of good convergence for a general field location, panel size/shape and forward speed (Froude Number). The high accuracy numerical scheme is valid for calculation of the wave surface elevations at both near field and far-field, and also independent of the vessel forward speed. This is particularly important because the present numerical method will be applicable for both prediction of dynamic pressure distribution of a planing hull and the wash wave problem.

Numerical examples are provided for the elementary solution of a moving rectangular pressure patch. The results are well behaved, which is essential for some of the hydrodynamic problems, such as wave pattern of an ASV, wash wave prediction of an ASV, and prediction of hydrodynamic pressure distribution of a planing craft.

Chapter 7 Case Study – Hydrodynamics of Planing Hulls

In this Chapter, solution of the steady potential flow for a pressure patch moving on the free surface is applied to predict the hydrodynamic pressure distribution for the planing hulls. The selected hull forms are: three-dimensional flat plate planing hull, flat plate planing catamaran and prismatic planing hulls. The flat plate planing hull is a planing hull with a flat bottom; a flat plate planing catamaran is a planing catamaran whose bottoms of the demi-hulls are flat. Method of the application and numerical results are provided and discussed.

7.1 Introduction

When a craft is planing, a major part of its weight is supported by the hydrodynamic lift and the flow separates smoothly from trailing edge and part of the side hull. This feature of planing allows researchers to adopt a pressure distribution on the water surface to represent the effect of the wetted area of a planing surface, and to establish an integral equation which relates the unknown pressure on the planing surface to its hull offsets. Although the fundamentals for establishing the integral equation are the same, numerical approaches to solve the problem may be significantly different for different authors.

Most of early studies on planing hydrodynamics dealt with two dimensional problems or three dimensional problems with restrictions on Froude number or aspect ratio (Maruo, 1967, Wang et al., 1971, Tuck, 1975). Based on Maruo’s (1967) slender planing theory, Taravella and Vorus (2011) have developed a general solution for flat and slender planing surface with vertex distribution method. Finite pressure elements were adopted to represent a three-dimensional planing surface without imposing restrictions on Froude number and aspect ratio (Doctors, 1975, Wellicome and Jahangeer, 1978, Tong, 1989). However these results showed unrealistic oscillatory pressure distribution. To solve the pressure oscillatory problem, transverse strips of variable pressure were proposed to represent a rectangular planing surface and achieved satisfactory convergence for flat plate hulls (Cheng and Wellicome, 1994) and flat planing catamaran (Cheng and Wellicome, 1999). The transverse strip method was less successful for prismatic planing hulls (Cheng and Wellicome, 1999).

In order to avoid the oscillatory behaviour of the predicted hydrodynamic pressure, a least square method was utilized in which the number of the free surface elevation points is much larger than that of the pressure source points on the hull (Tuck, Scullen and Lazauskes, 2002), this is effectively a filtering approach (averaging), the obtained pressure is then smoother. Pyramidal pressure element distribution model originally developed by Doctors (1975) was adopted to solve the planing problem, and it was found that the matrix for solving the unknown pressure is ill conditioned (Wang and Day, 2007). The Singular Value Decomposition technique is used to tackle the problem. In mathematical terms, this is a similar process to filter the pressure distribution. The numerical instability problem will be investigated in this chapter.

7.2 Flat Plate Planing Hull

The hydrodynamic problem of a 3-D flat planing hull is illustrated in Figure 7.1. The planing hull is moving on the calm water surface with forward speed of U and a small trim angle of τ. The problem is to find dynamic pressure distribution on the wetted hull surface:

$$\Pi(x,y)=\begin{cases} p(\xi,\eta) & (\xi,\eta)\in S_c \\ 0 & (\xi,\eta)\notin S_c \end{cases} \tag{7.1}$$

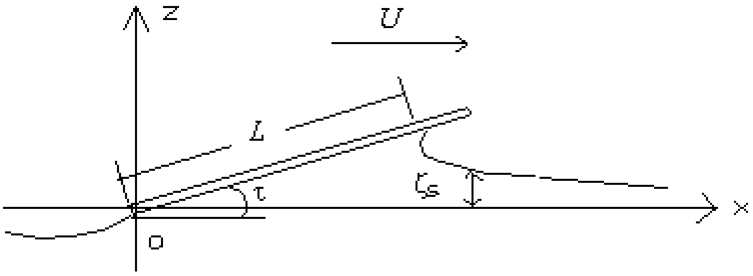

Figure 7.1 The hydrodynamic problem of flat plate planing hull

(L – length, τ – trim angle, U – forward speed, ς_s – free surface elevation)

In order to solve the planing hydrodynamic problem, the planing surface is replaced by a pressure distribution and the kinematic free surface condition will be utilised, in which the pressure induced free surface elevation underneath the planing hull is set equal to the hull vertical offset:

$$\begin{aligned}\varsigma_s(x,y) = &\frac{1}{\pi^2 \rho U}\iint_{S_c} p(\xi,\eta)d\xi d\eta \int_0^{\pi/2} d\theta \sec\theta \text{ P.V.}\int_0^{\infty} \frac{k^2}{k-k_0\sec^2\theta}\cos[k(x-\xi)\cos\theta]\cos[k(y-\eta)\sin\theta]dk \\ &+\frac{k_0^2}{\pi\rho g}\iint_{S_c} p(\xi,\eta)d\xi d\eta \int_0^{\pi/2} \frac{\sin[k_0(x-\xi)\sec\theta]\cos[k_0(y-\eta)\sec^2\theta\sin\theta]}{\cos^4\theta}d\theta - \frac{\Pi(x,y)}{\rho g} \\ &= \hat{z}(x,y) \qquad\qquad (x,y)\in S_c \end{aligned} \tag{7.2}$$

Since the offset of the planing hull, $\hat{z}(x,y)$, is known for a giving design, in order to obtain the pressure distribution, $p(\xi,\eta)$, we need to solve integral equation (7.2). In doing so, the planing surface, S_c, is divided into a number of rectangular elements, over which the pressure strength is constant, see Figure 7.2. In discretised form of (7.2), the free surface elevation on a field point (x_j, y_j) can be expressed as

$$\varsigma_s(x_j,y_j) = \sum_{i=1}^{N}\tilde{D}_{j,i}p_i \tag{7.3}$$

where $\tilde{D}_{j,i}$ is the wave elevation at field point (x_j, y_j) by a pressure element located at (ξ_i, η_i) with unit strength and can be calculated by the numerical method described in Chapter 6. Substituting (7.3) into (7.2), one obtains:

$$\sum_{i=1}^{N}\tilde{D}_{j,i}p_i = \hat{z}(x_j,y_j) \qquad\qquad j=1,2,...,N \tag{7.4}$$

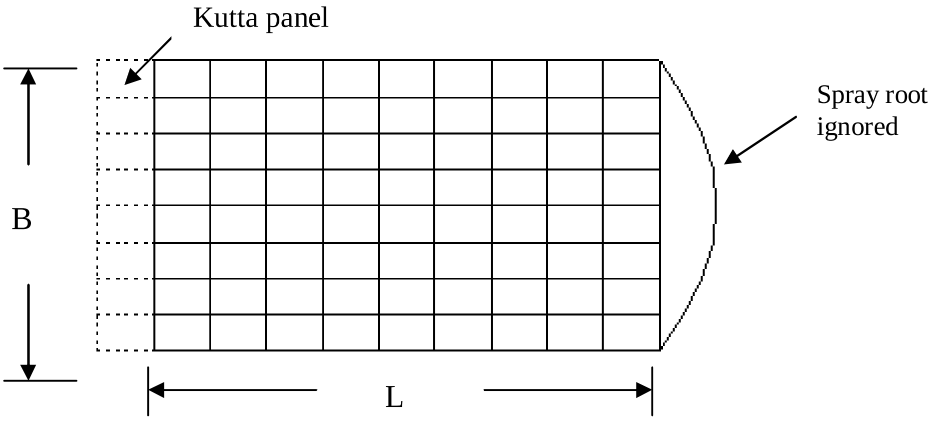

Figure 7.2 Representation of the flat plate planing hull by pressure elements

In order to satisfy the Kutta condition at the trailing edge of the planing hull, an additional row of elements are added at stern of the hull, see Figure 7.2. By satisfying a Kutta condition, the flow detaches freely from stern of the craft, and the pressure is atmospheric pressure at the trailing edge. The free surface elevations on the Kutta panels are to be determined:

$$\sum_{i=1}^{N} \tilde{D}_{N+k,i} p_i = \tilde{z}(x_{N+k}, y_{N+k}) \qquad k = 1, 2, ..., K \tag{7.5}$$

where K is total number of the Kutta elements. (7.4) and (7.5) form a close set of linear algebra equations for the unknown pressure strength $p_j, j = 1, 2, ..., N$ on the wetted hull surface and the trailing edge profile at the stern $\tilde{z}_{N+k}, k = 1, 2, ..., K$. In the present study, the spray root is ignored for the flat plate planing hull. The vertical hull offsets can be expressed as

$$\hat{z}_j = H_j + x_j \cdot \tau \tag{7.6}$$

where τ is the trim angle, which is assumed to be small, H_j is the transom stern profile. The non-dimensional pressure coefficient is defined as

$$c_p = \frac{p}{0.5 \rho U^2 \cdot \tau} \tag{7.7}$$

Non-dimensional lift force and pressure centre are defined as

$$C_L = \frac{F_L}{0.5 \rho U^2 BL \cdot \tau} \tag{7.8}$$

$$L_{CP} = \frac{l_{cp}}{L} \tag{7.9}$$

where F_L is lift force, l_{cp} is the distance between the dynamic pressure centre and stern of the hull.

The problem for solving the hydrodynamic pressure distribution mentioned above is a “particularly unpleasant task” (Tuck et al., 2002). It was found that the obtained pressure distribution has a grid-scale oscillatory behaviour. Figure 7.3 shows an example of convergence of the pressure distribution at the central line of a flat plate planing hull. Beam/length ratio of the hull is $B/L = 0.67$ and the length Froude number $Fn = 2.86$. Four truncations of the upper limit for the integral D_2 are selected: $u_c = 1000, 1500, 5000, 50000$, respectively. It can be seen that at the lower truncations ($u_c = 1000, 1500$), the predicted pressure distributions clearly show grid-scale oscillatory behaviour, this was also found in the works of Doctors (1975), Tong (1989), Tuck et al (2002) and Wang and Day (2007), even negative pressure exists. However, as the truncation of the integral increases to $u_c = 5000, 50000$, the influence coefficients are expected to be converged with higher accuracy, and the grid scale oscillatory behaviour of the predicted pressure distribution disappears. Figure 7.4 is the 3D views of the predicted pressure distribution with and without oscillation, respectively. This shows that the truncation of the integrals of the influence coefficients play a vital role in obtaining realistic pressure distribution on the planing surface and eliminating the numerical instability. Numerical tests so far demonstrated that for a normal planing surface the truncation of integral D_2 at $u_c = 30000$ will result a reasonably smooth pressure distribution.

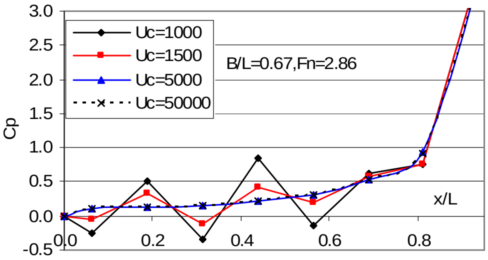

Figure 7.3 Convergence of pressure distribution on the central line of a flat plate hull

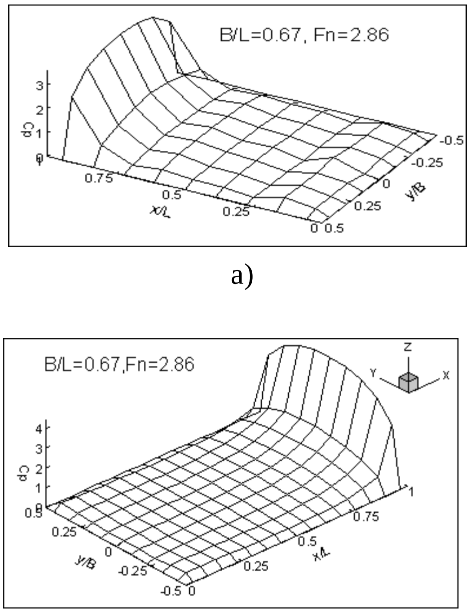

a)

b)

Figure 7.4 Pressure distribution of a flat plate hull(a: $u_c = 2000$; b: $u_c = 50000$)

To avoid the pressure oscillatory problem, Cheng and Wellicome (1994) developed a pressure strip method, in which a planing surface is represented by an assemblage of strips of transversely variable pressure placed on the mean free surface. Figure 7.5 is a comparison between the present results and a model test measurement for pressure distribution at the central line of a flat plate of $B/L=1.22$, and length Froude number $Fn=U/\sqrt{gL}=3.86$. The agreement is fairly satisfactory, and no oscillatory behaviour exists for the results of the present prediction. There are discrepancies between the model test and the numerical predictions at the bow region, this may be due to the assumption of ignoring the spray root made in the theoretical model.

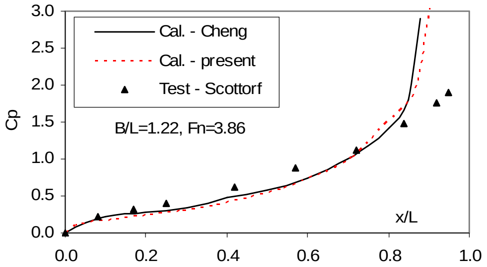

Figure 7.5 Comparison of pressure distribution at the central plane of a flat plate hull

Figure 7.6 shows the pressure distribution of a flat plate planing hull with beam/length ratio of $B/L=0.5$. 176 pressure panels were used in the calculation, which is equal to the number of hull offset points. Draft at stern and trim angle is prescribed before the calculation. It can be seen that the obtained pressure distribution is free of the grid-scale oscillation. A similar case was also predicted by Tuck et al. (2002). In the calculation of Tuck et al., the hull length is $L=80m$ and width is $B=40m$, displacement is 3200 tones and craft speed is 40 knots. 2000 hull offset points and 176 pressure elements were used for the least square approach in the calculation. The result is reproduced and shown in Figure 7.7 for the purpose of comparison. The Froude number of Tuck et al. differs from that of the present study, thus the pressure magnitude and distributions of the two computations may be different. Nevertheless it can be clearly seen that results of Tuck et al. still have some small wavy oscillations after the least square process

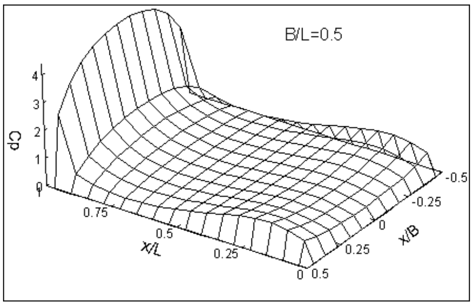

Figure 7.6 Pressure distribution of a flat plate hull ($Fn = 2.0$)

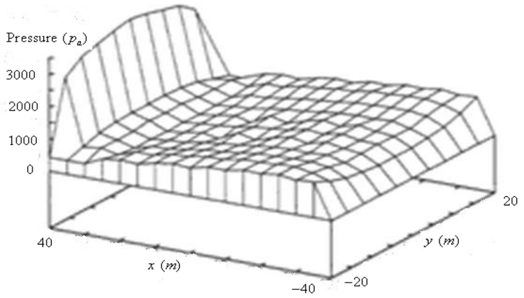

Figure 7.7 Pressure distribution of a flat plate with $B/L = 0.5$ at $Fn = 0.73$, $L = 80m$,
Tuck et al. (2002),

Figure 7.8 shows a comparison of the present prediction with other published numerical results. The agreement is good. Figure 7.9 is a convergence study of the transversal pressure distributions for various numbers of buttocks to discretise the planing hull. The pressure distribution converges well. Figures 7.10 ~ 7.12 show the 3D views of the pressure distributions for flat planing plates with length/beam ratio $B/L = 0.5,\ 1.0$ and 1.2, respectively. The predicted pressure distribution over the planing surface is quite smooth and no grid-scale oscillatory behaviour exists.

Figure 7.13 is the predicted transom stern profile for a flat plate planing hull with $B/L = 0.5, Fn = 2.24$. For a given rectangular wetted area, which is supposed to correspond to a flat plate, the predicted transom profile is slightly bended in order to satisfy the Kutta condition as shown in Figure 7.13. Furthermore, a prescribed wetted area may correspond to slightly different transom profiles at different planing speed. Fortunately the influence of such a small hull curvature on the hydrodynamic force is negligible, and the effect of the planing speed on the transom profile is hardly discernible (Cheng and Wellicome, 1994).

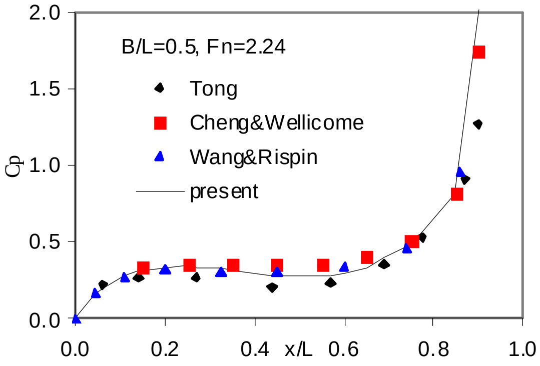

Figure 7.8 Pressure distribution on the central plane of a flat plate planing hull ($B/L = 0.5$, $Fn = 2.24$)

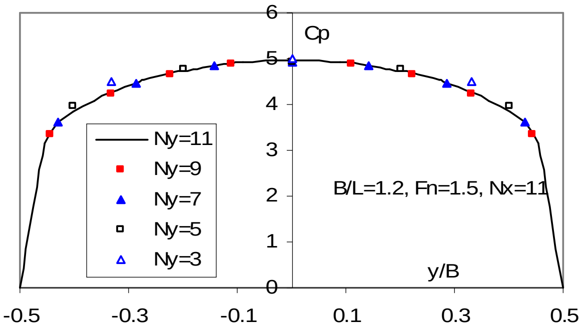

Figure 7.9 Convergence of the pressure distribution for a flat plate planing hull with various patches at the bow ($i_x = Nx = 11$) on flat planing hull ($B/L = 1.2$, $Fn = 1.50$)

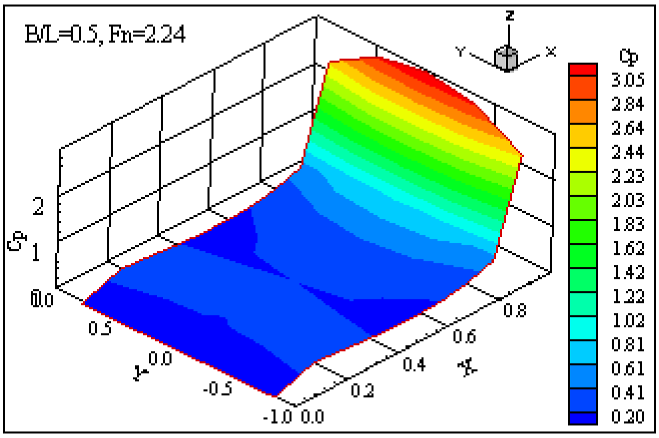

Figure 7.10 3-D pressure distribution of a flat plate planing hull ($B/L = 0.5$, $Fn = 2.24$, $C_L = 0.581$, $L_{CP} = 0.72$)

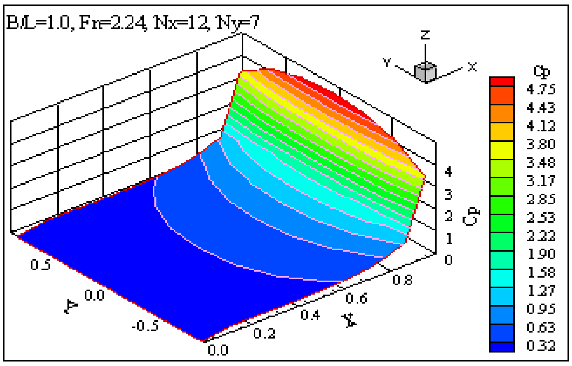

Figure 7.11 3-D pressure distribution of a flat plate planing hull ($B/L = 1.0$, $C_L = 0.796$, $L_{CP} = 0.79$)

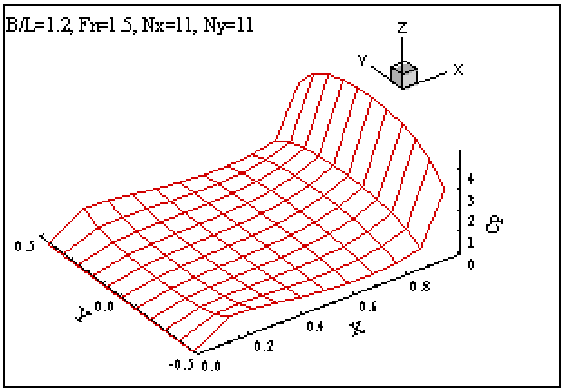

Figure 7.12 3-D pressure distribution of a flat plate planing hull ($B/L = 1.2$, $Fn = 1.50$, $C_L = 0.988$, $L_{CP} = 0.721$)

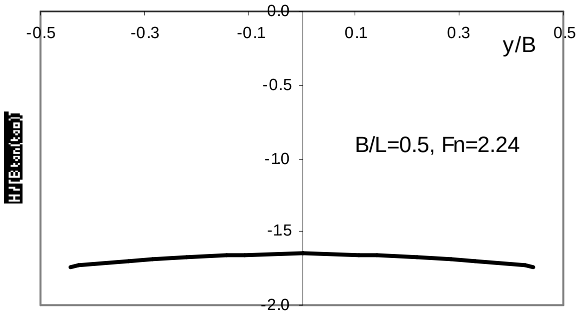

Figure 7.13 Predicted trailing-edge profile for a flat plate planing hull ($B/L = 0.5$, $Fn = 2.24$)

7.3 Flat Plate Planing Catamaran

The pressure patch distribution method is also applied to the hydrodynamic analysis of the flat plate planing catamaran. The two demi-hulls are represented by two pressure distributions on the free surface. At the trailing edge of each demi-hull, some Kutta panels are added in which the pressure is atmospheric pressure (omitted in Figure 7.13) and the profiles are to be determined with the pressure integral equations. The spray root on the bow region is ignored. The hydrodynamic interaction between the two demi planing hulls can be investigated. Length and beam of the demi-hull are L and B, respectively. Distance between the central lines of the two demi-hulls is S_p. The wetted hull surface of the flat plate planing catamaran is divided into a number of rectangular panels, see Figure 7.14.

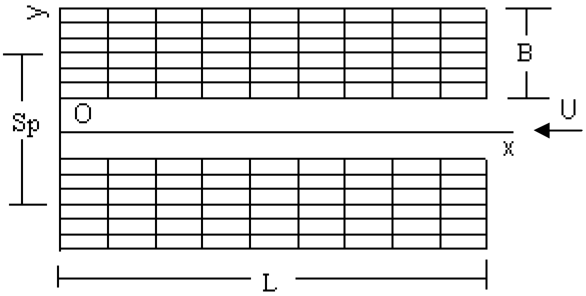

Figure 7.14 Discretization of the catamaran demi-hulls

Figure 7.15 shows the central line pressure distribution of the demi-hull for a flat plate catamaran with $B/L=0.35, S_p/L=0.4$. At lower speed, there are higher pressure regions on the aft part of the hull; as the craft speed increases, the dynamic pressure on the aft part of hull decreases and the pressure centre shifts towards to the bow. The predicted pressure distributions are well behaved and without the grid-scale oscillation. Figure 7.16 is a sample of the predicted pressure distribution on the flat plate catamaran hull at the length based Froude number $Fn = U/\sqrt{gL} = 2.5$, and again, pressure distribution over the whole hull surface exhibits the same characteristics and free of the numerical instability.

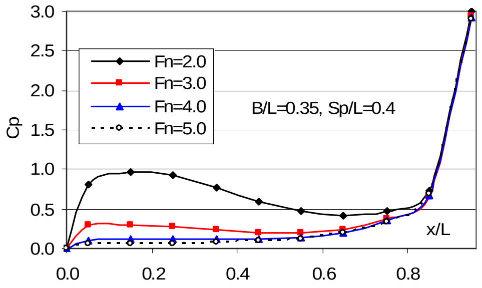

Figure 7.15 Pressure on the central line of demi-hull for a flat plate catamaran planing hull

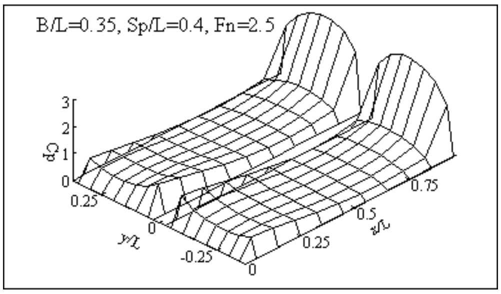

Figure 7.16 Pressure distribution of a flat plate planing catamaran at $Fn = 2.5$

Figures 7.17 and 7.18 show the effect of the demi-hull separation on the dynamic lift and the pressure centre. The separations between the two demi-hulls are $S_p / L = 0.4, 0.5$ and 0.7, respectively. The results of the flat plate planing mono-hull which is the same as the demi-hull are also plotted for the comparison. For a catamaran hull, the non-dimensional lift is defined as

$$C_L = \frac{F_L}{0.5 \rho U^2 B^2 \tau \times 2} \tag{7.10}$$

where F_L is the lift force, τ is the trim angle and the factor 2 in the numerator means for the two demi-hulls. The non-dimensional pressure centre is defined as

$$L_{cp} = \frac{x_{cp}}{L} \tag{7.11}$$

where x_{cp} is distance of the pressure centre to stern. For mono planing hull, the lift coefficient is defined as

$$C_L = \frac{F_L}{0.5 \rho U^2 B^2 \tau} \tag{7.12}$$

The hydrodynamic interaction between the demi-hulls can be observed in Figure 7.17. The dynamic lift is much different from that of the mono-hull for a closer demi-hull separation. However, the trends of lift force against the craft speed are similar. Figure 7.18 presents the results of the predicted pressure centre. The pressure centre is less sensitive to the demi-hull separation. Figures 7.19 and 7.20 show effects of the demi-hull separation on the central line pressure. The dynamic pressure increases as the demi-hull separation decreases.

It should be mentioned that a linear potential theory is used in the present study, therefore, the non-linear effects such as the spray was not accounted for. This may affect the validity of the present results (like any other similar theories) in some cases (e.g., Cheng and Wellcome, 1999).

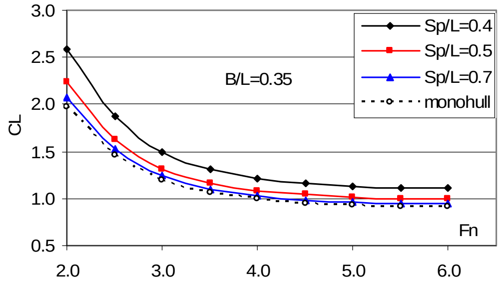

Fig. 7.17 Lift coefficient for the flat plate catamaran planing hulls

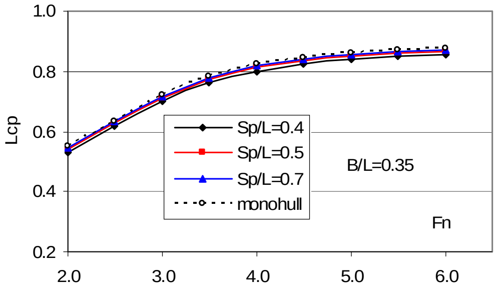

Figure 7.18 Pressure centre for the flat plate catamaran planing hulls

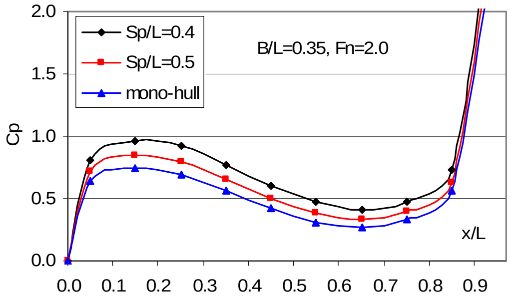

Figure 7.19 Pressure on the central line for the flat plate planing catamaran

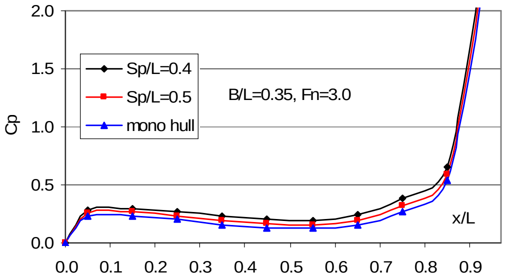

Figure 7.20 Pressure on the central line for the flat plate planing catamaran

7.4 Prismatic Planing Hull

The pressure patch method is used to predict the hydrodynamic pressure distribution for a prismatic planing hull. Figure 7.21 shows definition of the hull, where β and τ are the deadrise angle and trim angle, respectively. B is the hull beam; L_C and L_K are the wetted chine length and keel length, respectively. The pressure patch arrangement is depictured in Figure 7.22.

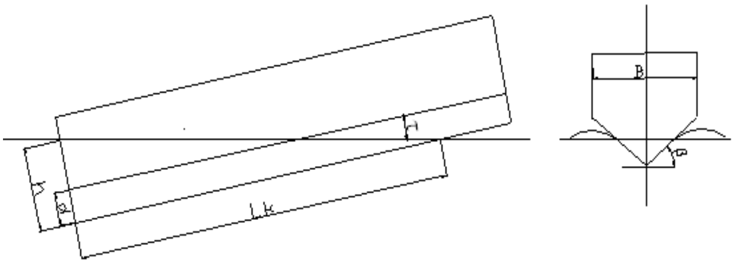

Figure 7.21 Definition of the prismatic planing hull

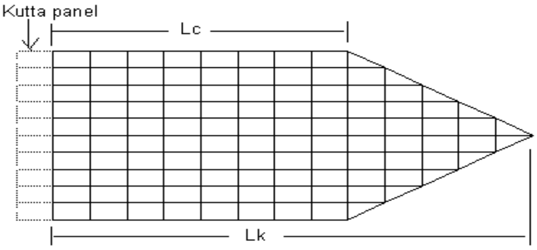

Figure 7.22 Panel distribution for a prismatic planing hull

Figures 7.23 and 7.24 show the dynamic lift and pressure centre of a prismatic planing hull whose chine and keel wetted lengths are $L_K/B=1.5, L_C/B=1.0$, respectively. The predicted results of Cheng and Wellicome (1999) using the transverse pressure strip method and results obtained by Savitsky's empirical formula (Savitsky, 1964) are also plotted in the figures. It is noticed from these figures that the present results agree with that of Savitsky better than those predicted by Cheng and Wellicome. The lift force coefficients of Cheng and Wellicome are sensitive to Froude numbers. This is probably because the transverse strip with sine series pressure terms will have difficulty in modelling the pressure distribution at the fore part of the hull. In fact, as it can be seen from Figures 7.25 ~ 7.27, there are stagnation points along the front waterline where the dynamic pressure is high. The constant pressure patch distribution method has the flexibility of modelling this type of pressure distribution, while in the transverse strip method, the pressure trends to zero near both ends of each strip (see, equation (6.5)), therefore it would be unable to reflect this type of distribution. Definition of the non-dimensional lift force for a prismatic hull is the same as in equation (7.12), while the non-dimensional pressure centre is defined as $L_{cp} = x_{cp} / B$. The definitions of C_L and L_{cp} for the prismatic hulls in this study are slightly different from those of Cheng and Wellicome (1999). These results are transformed into the present definitions and shown in Figure 7.23 and 7.24 for the comparison. Figure 7.28 shows an example of predicted trailing edge profile for a prismatic planing hull with the wetted keel length of $L_K / B = 1.5$ and the wetted chine length $L_C / B = 1.0$. The predicted trailing edge profiles are slightly bended in comparison to the real hull transom stern. However, the effect of planing speed on the transom profile is hardly distinguishable (see Figure 7.28) and the influence of such a small hull curvature on the hydrodynamic force is negligible.

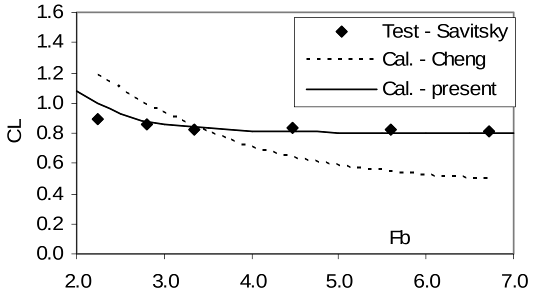

Figure 7.23 Lift coefficient for a prismatic planing hull ($L_K / B = 1.5, L_C / B = 1.0$)

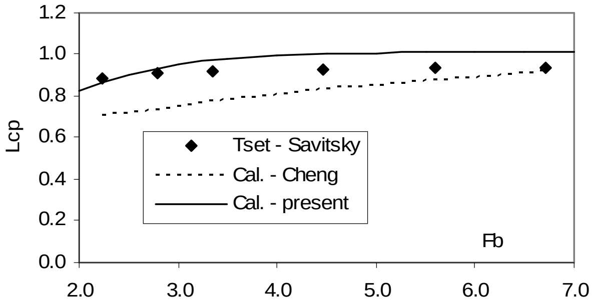

Figure 7.24 Pressure centre of a prismatic planing hull ($L_K / B = 1.5, L_C / B = 1.0$)

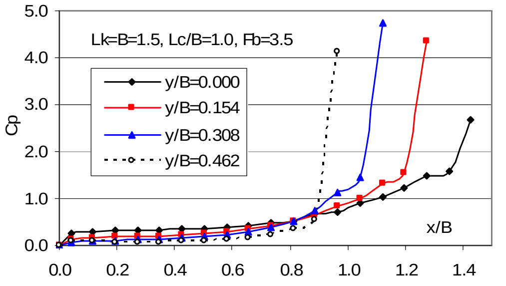

Figure 7.25 Pressure distribution for a prismatic planing hull

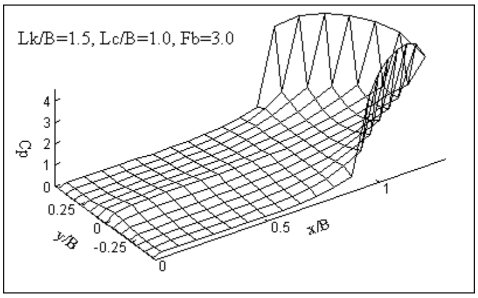

Figure 7.26 Pressure distribution for a prismatic planing hull ($L_K / B = 1.5, L_C / B = 1.0$)

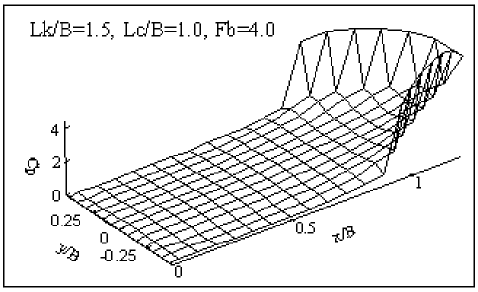

Figure 7.27 Pressure distribution for a prismatic planing hull ($L_K / B = 1.5, L_C / B = 1.0$)

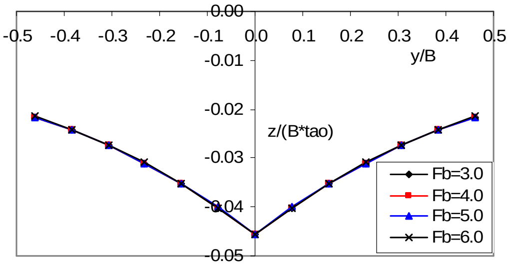

Figure 7.28 Predicted trailing edge profile of a prismatic planing hull

($L_K / B = 1.5, L_C / B = 1.0$)

7.5 Summary

In this Chapter, solution of the steady potential flow of a pressure patch moving on the free surface has been applied to predict the hydrodynamic pressure distributions of some planing crafts: flat plate hull, flat plate catamaran and prismatic hull. Results obtained by the present method show satisfactory agreements with other researches. The numerical instability of the grid-scale oscillatory behaviour in the predicted pressure distribution over the planing hull surfaces found in some previous studies has been eliminated.

Chapter 8 Case Study – Prediction of Wash Waves

In Chapter 7, the elementary solution of a pressure patch moving on the free surface presented in Chapter 6 is applied to the prediction of the hydrodynamic pressure distribution for a planing hull, where the relative position between the pressure source point and the field point is relatively small. In this Chapter, the elementary solution of a pressure patch moving on the free surface is used to predict the wash wave of SES and ASV. The main difference between predictions of the hydrodynamic pressure for a planing hull and that of the wash waves is that the relative position between the pressure source point and the field point is relatively large for the wash wave prediction. The method of the application and numerical results are provided and discussed.

8.1 Wash Wave Predictions for SES

For vessels whose weight is mainly supported by hydrodynamic force (e,g, planing crafts), SES or ASV (e.g., the ALV), the displacement of the rigid hull for these vessels is a small portion of its weight (less than 20%), it is expected that waves generated by the rigid hull may be neglected, and the wash wave fields can be predicted by the pressure patch distribution method.

As mentioned previously, unlike the prediction of the hydrodynamic pressure of a planing hull, the relative position between the source point and field point is large for the wash wave calculation. Since the distance between the source point and the field point has been taken into consideration in the variable transformation of the numerical scheme for evaluation of the free surface elevation in the present study, see, equation (6.28), the procedure proposed in Chapter 6 can be adopted in the wash wave prediction directly.

We recall the free surface elevation generated by a rectangular pressure patch of equation (6.21):

$$\varsigma_s(x,y)=\varsigma_1(x,y)+\varsigma_2(x,y) \tag{8.1}$$

where

$$\begin{cases} \varsigma_1(x,y) = -\dfrac{P_0\delta_{j,i}}{\rho g} - \dfrac{P_0}{2\pi^2\rho g}\sum_{m=1}^{8}(-1)^{m+1}J_{1m} \\ \varsigma_2(x,y) = -\dfrac{P_0}{2\pi^2\rho g}\sum_{m=1}^{8}(-1)^{m+1}J_{2m} \end{cases} \tag{8.2}$$

where P_0 is the pressure strength on the element. For planing hulls, the pressure strength can be obtained by solving the integral equation relating the pressure distribution to the hull vertical offsets, see Chapter 7; whilst for SES and the ALV, where the cushion pressure is assumed as constant, and the excess pressure is approximated as the average pressure on the cushion which is the vessel's weight divided by the cushion area and neglecting the small portion of the displacement value from buoyancy and hydrodynamic lift from the wetted part of the rigid hull.

It is known that the rate at which the pressure is transferring energy to the fluid is equal to the power consumption. Therefore the wave-making resistance of a constant pressure patch is

$$R_w U = -\iint_{S_c} p(x,y)\cdot\frac{\partial\phi_s}{\partial z}(x,y,0)dxdy \tag{8.3}$$

By using the kinematic free surface boundary condition (6.4), the wave-making resistance for a rectangular pressure patch with constant pressure strength of P_0 can be written as

$$R_w = P_0\int_{-b}^{b}\left[\varsigma_s(a,y)-\varsigma_s(-a,y)\right]dy \tag{8.4}$$

Figure 8.1 shows a comparison of wave cut for a rectangular pressure patch, while Figure 8.2 shows the predicted wave-making resistance for a rectangular pressure patch. The agreements between the present predictions and other published results are satisfactory. It is also noticed that $C_w \to 0$ as $f_n \to \infty$. The non-dimensional wave elevation and wave-making resistance are defined as

$$\tilde{\varsigma} = \frac{\rho g \varsigma_s}{P_0} \tag{8.5}$$

$$C_w = \frac{\rho g R_w}{2bP_0^2} \tag{8.6}$$

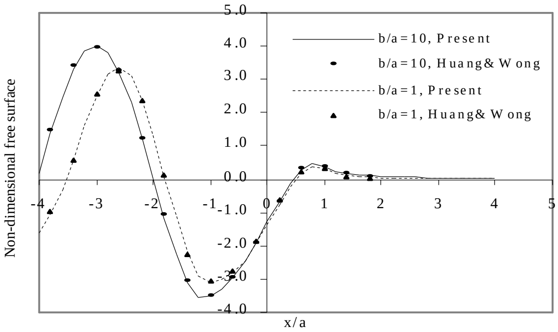

Figure 8.1 Comparison of the wave cuts at $y = 0$, $Fn = 0.57$

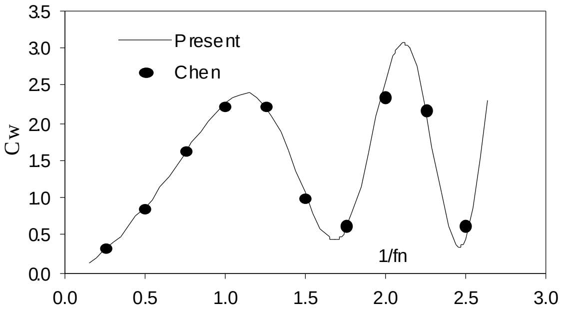

Figure 8.2 Wave-making resistance of a rectangular pressure patch ($b/a = 0.5,\ fn = U/\sqrt{ga}$)

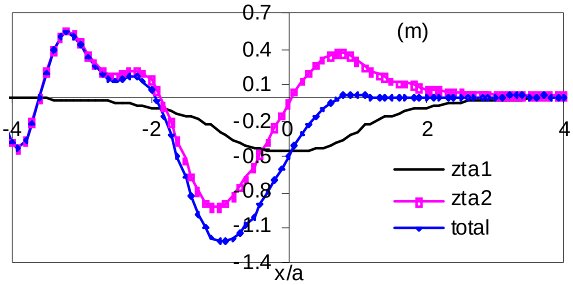

Figure 8.3 Components of the wash wave of a SES ($B/L = 0.2, Fn = 1.0, y = 0, L = 40m$)

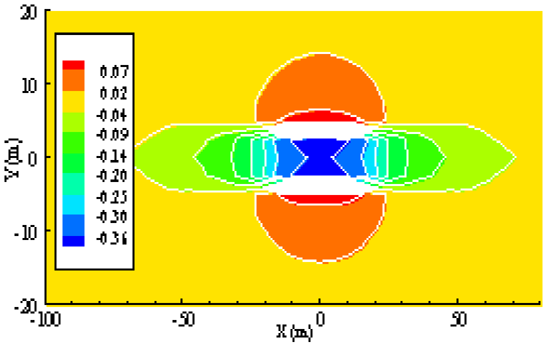

Figure 8.4 Local effect part of the wash wave of a SES ($\tilde{\varsigma}_1 = \rho g \varsigma_1 / P_0$, $Fn = 1.5$)

It may be helpful to notice some of the properties of (8.2). In fact, $\varsigma_1(x,y)$ is a local wave, and decays quickly when the relative distance increases, see Figures 8.3 and 8.4. In Figure 8.3, the wave elevation of the local effect part ($\varsigma_1 = zta1$) is relatively small at the longitudinal location beyond $x = 2L$ up-stream and $x = -2L$ down-stream from midship of the vessel. The second term, $\varsigma_2(x,y)$, is the wave term, and will propagate far away from the vessel.

Figure 8.5 is a bird's view of the wave field for a rectangular pressure patch. The Kelvin wave pattern is clearly observed in this picture. Figures 8.6 and 8.7 show the wash wave fields of a SES at $Fn = 0.5$ and 1.5, respectively. The contribution of the wash waves from the rigid side hulls of the SES has been neglected. The vessel has a displacement of 200 tons, its cushion length is 40m and the beam-length ratio is $b/a = 0.2$. It can be seen that there are divergent and transversal wave systems at $Fn = 0.5$, however, only divergent wave system exists at a high Froude number ($Fn = 1.5$).

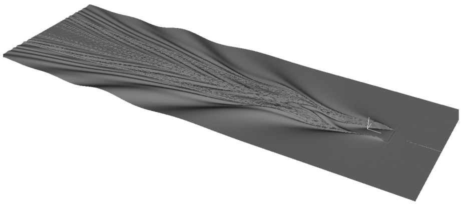

Figure 8.5 Wave pattern of a rectangular pressure patch with $b/a = 0.5$ at $Fn = 0.71$

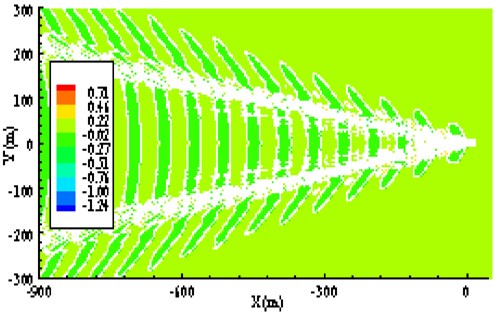

Figure 8.6 Wash wave of a SES at $Fn = 0.5$

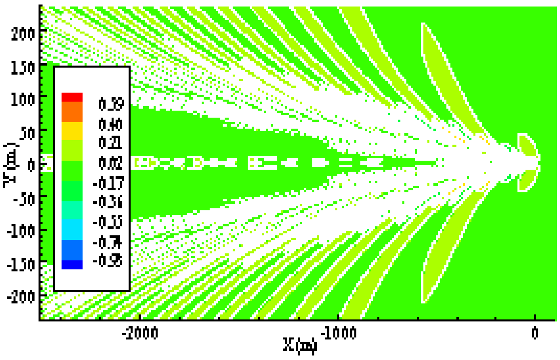

Figure 8.7 Wash wave of a SES at $Fn = 1.5$

8.2 Wash Wave Prediction for the ALV

The wash wave field of an Air-Lifted Vessel is also calculated by the pressure patch method. Details of the ALV are described in Chapter 10. The vessel has two cushion chambers and similar to catamaran configuration. Beam/length ratio of demi-hull of the ALV is $B_c / L_c = 0.16$, the separation between the central planes of the demi-hulls is $S_p / L_c = 0.32$. Its displacement is 200 tons and length is 40m. The major part of weight of the vessel is supported by the excess pressure in the cushions (Allenstrom et al. 2003), thus, the effect of the steady wave caused by the rigid side-hull walls is ignored. Figure 8.8 shows pressure element representation of the cushions for the ALV.

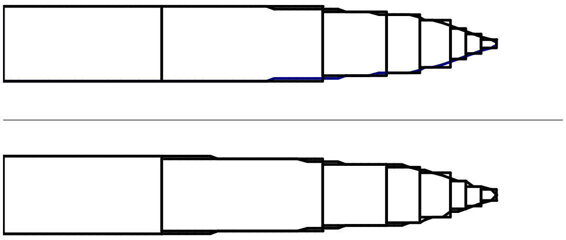

Figure 8.8 representation of the cushion area of an Air Lifted Vessel

The total wash wave field of the vessel is the sum of all the contributions from each of the cushion pressure elements:

$$\begin{cases} \varsigma_1(x,y) = \sum_{j=1}^{N} p_j \varsigma_{1,j} \\ \varsigma_2(x,y) = \sum_{j=1}^{N} p_j \varsigma_{2,j} \end{cases} \tag{8.7}$$

and the wave-making resistance can be calculated as

$$R_w = \sum_{j=1}^{N} R_{w,j} \tag{8.8}$$

where N is the total number of the elements, $R_{w,j}$ is the wave-making resistance of the j^{th} rectangular pressure patch, and is calculated by (8.4)

$$R_{w,j} = p_j \iint_{\Delta S_j} \frac{\partial \varsigma_j(x,y)}{\partial x} dxdy \tag{8.9}$$

where p_j is the pressure strength of the rectangular element. Substituting (8.9) into (8.8), the wave-making resistance of the ALV is

$$R_w = \sum_{j=1}^{N} R_{w,j} = \sum_{j=1}^{N} p_j \iint_{\Delta S_j} \frac{\partial \varsigma_j(x,y)}{\partial x} dxdy \tag{8.10}$$

Several wash wave criteria have been proposed. Anderson et al. (2000) suggested the following non-dimensional number:

$$Q = \frac{R_w}{gD_w} \tag{8.11}$$

as the means of comparison in terms of ship wash wave for different type of vessel and/or at different speed, where D_w is the dead weight of the vessel. Zaraphonitis et al. (2002) adopted the following wave wash definition:

$$W = \sqrt{\frac{1}{x_2 - x_1} \int_{x_1}^{x_2} \varsigma_s(x,\bar{y})^2 dx} \tag{8.12}$$

where $\bar{y}$ is wave-cut location, x_1, x_2 are the starting and ending points of the integration interval along the wave-cut. Papanikolaou (2010) used (8.12) as one of the design objectives for ship hull form design. Allenstrom et al. (2003) used wave energy per metre wave front in deep water as the measure of the wash wave

$$E_1(\bar{y}) = \frac{1}{8} \rho g H^2(\bar{y})(gT^2/2\pi) = 1961 H^2(\bar{y}) T^2 \tag{8.13}$$

where $H(\bar{y})$ is the wave height of the wave front of the wave-cut at the location $y = \bar{y}$, T is the wave period.

In the present study, the wave energy is also taken as the wash wave criteria, and the wave energy is defined as

$$E = \frac{1}{8}\rho g \lambda H_m^2(\bar{y}) \tag{8.14}$$

where $H_m(\bar{y})$ is the maximum wave height of the wave-cut at the distance of $y = \bar{y}$, λ is the corresponding wave length of the wave with the maximum wave height.

It should be mentioned that the wave energies calculated by (8.13) and (8.14) may be different, this is because the maximum wave height does not necessarily occur in the wave front, especially when a vessel is travelling at high speed, as discussed late.

Figure 8.9 is the predicted wave-making resistance by the excess pressure inside the two cushions for two ALV designs. Each design has the same demi-hull geometry, but the separations between the demi-hulls are 0.26 and 0.65, respectively. The wave-making resistance for a single demi-hull is also plotted in the figure. For each of the Air Lifted Vessel configuration, the resistance coefficients have a hump. The interactions between the two demi-hulls can be also identified in this picture. When vessel length Froude number is between 0.45 and 0.65, the resistance coefficients increase with decrease of separation distance of the demi-hull; however, when Froude number is larger than 0.72, the effect of the separation distance between the demi-hulls on the wave-making resistance coefficient has a opposite trends, i.e., increasing the separation distance will result a decrease for the resistance by the present definition of wave-making resistance coefficient in equation (8.6).

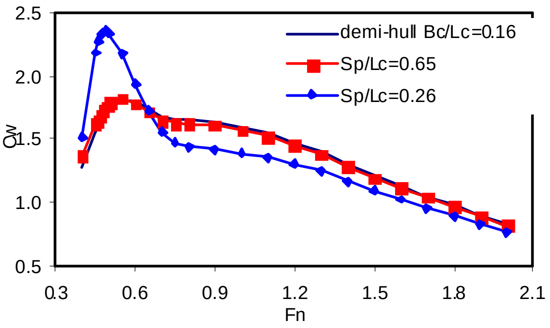

Figure 8.9 Wave-making resistance due to the cushion excess pressure of the ALV

An attempt is made to compare the resistance of the ALV based on the wave-making resistance of the cushion pressure predicted by the present numerical method and that of model test. Following Allenstrom et al. (2001,2003), the total resistance of the ALV in calm water is represented by:

$$R_t = R_f + R_w + R_{res} + R_{wind} \tag{8.15}$$

where R_f is the frictional resistance; R_w is the wave-making resistance due to cushion pressure, R_{res} is the residual resistance – mainly containing wave pattern resistance created by the rigid part of the hull, some spray and eddy-making resistance, and finally R_{wind} is the wind drag. The frictional resistance is calculated by:

$$R_f = C_f \cdot \frac{1}{2}\rho U^2 S_w \tag{8.16}$$

where S_w is area of the wetted hull surface, U is vessel speed, C_f is the frictional coefficient which is calculated by the ITTC formula:

$$C_f = \frac{0.075}{(\log Rn - 2)^2} \tag{8.17}$$

where Rn is length based Reynolds number. The wind drag is calculated by

$$R_{wind} = C_a \cdot \frac{1}{2}\rho_a U^2 A_T \tag{8.18}$$

where C_a is the drag coefficient, ρ_a is the air density and A_T is the transverse projected area of the above water part of the hull. For calculation of the residual resistance, two methods are adopted: for lower vessel speed ($Fn_\nabla = U/\sqrt{g\nabla^{1/3}} \le 3$), the estimate method for the resistance of a conventional catamaran is used, details can be found in Zhao et al (2009). While for higher vessel speed ($Fn_\nabla = U/\sqrt{g\nabla^{1/3}} > 3$, the fore rigid part of the ALV hull is treated as a planing surface, the residual resistance is calculated as

$$R_{res} \approx \mu \cdot F_L \cdot \tau^* \tag{8.19}$$

where F_L is the lift on the planing surface, τ^* is the angle of attack and μ is a coefficient representing the interface effect between the demi-hulls (Zhao et al. 2009).

The comparison between the predicted total resistance and that of the model test (Allenstrom et al. 2003) is shown in Figure 8.10. The agreement is reasonably satisfactory, but improvement may be made, for example, the predicted resistance at about $Fn = 0.5$ is lower than the model test measurement.

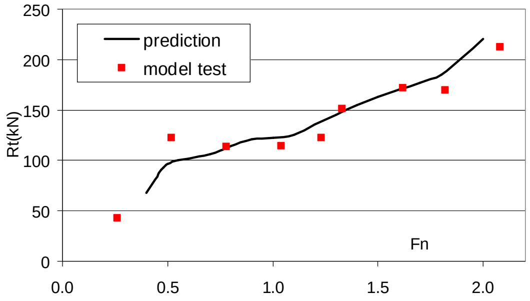

Figure 8.10 Comparison of total resistance of the ALV E40

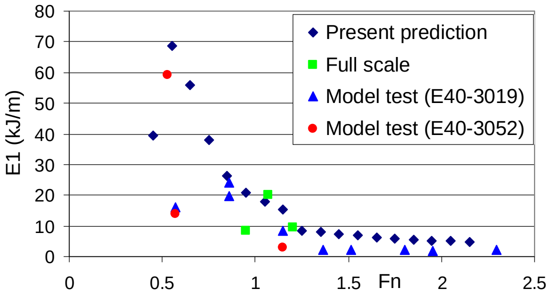

Figure 8.11 Comparison of the predicted and measured (Allenstrom et al., 2003) wave energy of the wash wave at $\bar{y} = 50m$ from the central line for the ALV E40

A comparison between the wave energies of the wash wave predicted by the present numerical method and that of model test/full scale measurements (Allenstrom et al. 2003) for the ALV E40 is presented in Figure 8.11. The location of the wave–cut is $\bar{y} = 50m$ from the centre line of the vessel at full scale. The wave energy is calculated by equation (8.13). At the lower vessel speed range ($Fn < 1.2$), the trends of both numerical and measurements are the same except a couple of scatted point from the measurements. At higher vessel speed range ($Fn > 1.2$), the predicted values are larger than that of the tank model tests. The reason is not clear yet. One possibility is that, at a high vessel speed, the wash wave (also the tank wall reflection wave) travels very quickly, and it may be difficult to record the first 3 undisturbed wave cycles.

The maximum wave height against the transversal distance from the central line of the ALV at various vessel speeds is shown in Figure 8.12. It can be seen that the maximum wave heights decay quicker at high Froude numbers, which means that when the vessel is travelling at high speed, there will be less wash wave height for the same transversal range of distance. The location of the maximum wave height is shown in Figure 8.13. The Kelvin line ($\alpha = 19.28^0$) is also shown. It can be observed that, for Fn=0.5, the calculated points fit with Kelvin line very well; however, for the other three higher Froude numbers ($Fn = 1.0,\ 1.5,\ 2.0$), the points do not follow Kelvin line due to the fact that they do not occur in the wave fronts. Figure 8.14 shows the wash wave energy calculated with equation (8.14). The trend is similar to the maximum wave height shown in Figure 8.12. However, the fact that the effect of wave period (or length) is taken into account in this criterion makes them different from the maximum wave height criterion. Figures 8.15 and 8.16 are samples of the wash wave pattern of the ALV with the basic design.

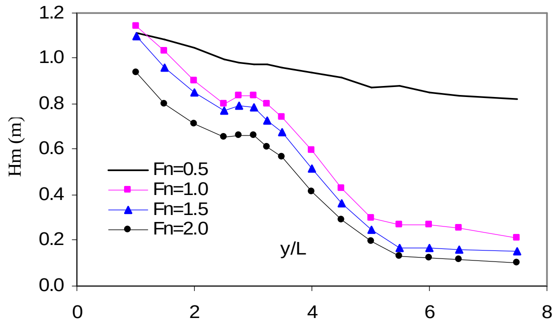

Figure 8.12 The maximum wash wave height of the ALV

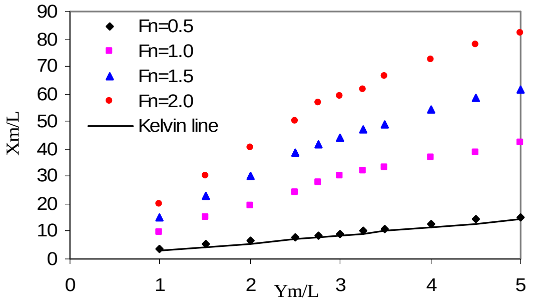

Figure 8.13 Location of the maximum wave height of the ALV

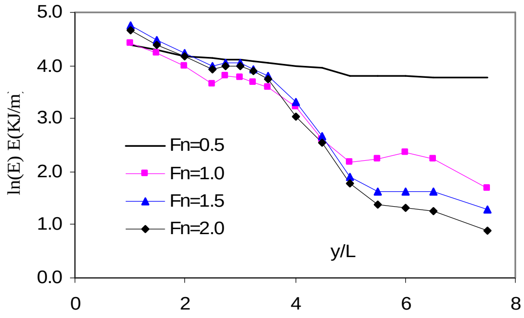

Figure 8.14 Wave energy per meter of the ALV

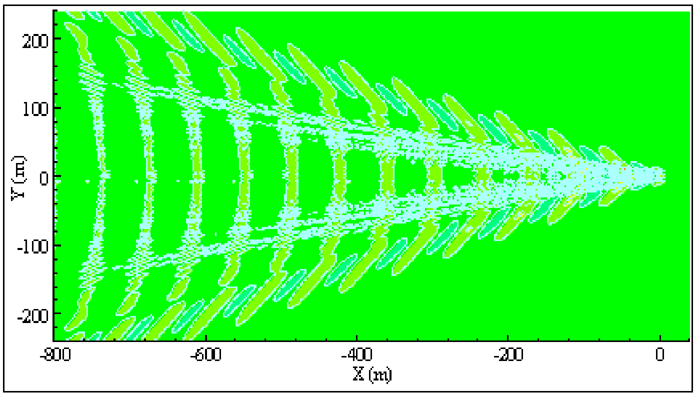

Figure 8.15 Wave pattern of an ALV at $Fn = 0.5$

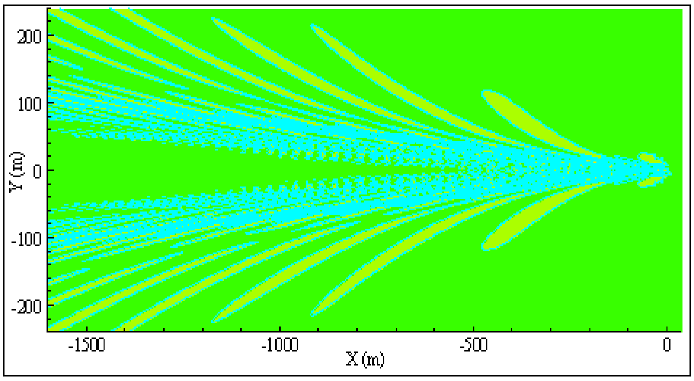

Figure 8.16 Wave pattern of an ALV at $Fn = 1.5$

It should be mentioned that, in the above wash wave prediction, the cushion pressure is assumed to be uniformly distributed. This is a reasonable approximation based on the measurement of the cushion pressure during tank model tests reported by Allenstrom, Lijenuberg and Tudem (2001, 2003). The wash waves generated by the rigid side hulls are not included. This approximation is justified by the fact that the majority weight of the vessel is supported by the air cushions. A validation with model test/full scale measurement supports this approximation.

8.3 Summary

In this Chapter, solution of the steady potential flow of a pressure patch moving on the free surface has been applied to the wash wave predictions for SES and the ASV. The present numerical approach can be used to predict the wash wave of a planing craft where the planing carft is replaced by a pressure distribution.

Chapter 9 The Three Dimensional Unsteady Flow Problem

In this Chapter, numerical methods for solving the potential flow of a pulsating and moving pressure distribution on the free surface are presented. Emphasis is placed on the free surface waves generated by the pressure patch. New numerical schemes are proposed for calculating the three-dimensional free surface elevation. Numerical results of the free surface elevation, escape area, escape volume are validated with existing results, and a fairly good agreement has been found. The solution of the free surface elevation is essential for predicting the unsteady motions of Air Supported Vessels. The equations of motions of the vessel in waves are also derived by using the adiabatic gas law in the air cushion.

9.1 Solution of the Unsteady Flow of a Pulsating Pressure Patch

It is assumed that a pulsating and moving pressure distribution on the free surface is:

$$P = \begin{cases} \Pi(x,y)e^{i\sigma t} & (x,y)\in S_c \\ 0 & \text{other} \end{cases} \tag{9.1}$$

The boundary value problem for the unsteady velocity potential described in Chapter 5 can be solved by using Fourier transformation method. The velocity potential (after the transient time period) can be written as (Wehausen and Laitone, 1960, Kim and Tsakonas, 1981):

$$\phi_u(x,y,z,t) = \mathrm{Re}\left\{\phi(x,y,z)e^{i\sigma t}\right\} \tag{9.2}$$

where

$$\phi = \frac{1}{4\pi^2\rho U^2}\iint_S \Pi(\xi,\eta)d\xi d\eta \left\{ -\int_0^{\pi/2} d\theta \sec^2\theta \int_0^\infty dk\Xi_1(\theta,k) + \int_{\theta_c}^{\pi/2} d\theta \sec^2\theta \int_0^\infty dk\Xi_2(\theta,k) + \int_0^{\theta_c} d\theta \sec^2\theta \int_0^\infty dk\Xi_2(\theta,k) \right\} \tag{9.3}$$

and

$$\Xi_1(\theta,k) = \left(Uk\cos\theta - \sigma\right)\frac{e^{k(z+ir_1)} + e^{k(z+ir_2)}}{k_1 - k_2}\left(\frac{k_1}{k-k_1} - \frac{k_2}{k-k_2}\right) \tag{9.4}$$

$$\Xi_2(\theta,k) = \left(Uk\cos\theta + \sigma\right)\frac{e^{k(z-ir_1)} + e^{k(z-ir_2)}}{k_3 - k_4}\left(\frac{k_3}{k-k_3} - \frac{k_4}{k-k_4}\right) \tag{9.5}$$

$$\begin{cases} r_1 = (x-\xi)\cos\theta + (y-\eta)\sin\theta \\ r_2 = (x-\xi)\cos\theta - (y-\eta)\sin\theta \end{cases} \tag{9.6}$$

The wave numbers are defined as

$$k_1 = 0.5k_0 \sec^2\theta\left[1+2\tau\cos\theta-\sqrt{1+4\tau\cos\theta}\right] \tag{9.7}$$

$$k_2 = 0.5k_0 \sec^2\theta\left[1+2\tau\cos\theta+\sqrt{1+4\tau\cos\theta}\right] \tag{9.8}$$

$$k_3 = 0.5k_0 \sec^2\theta\left[1-2\tau\cos\theta-\sqrt{1-4\tau\cos\theta}\right] \tag{9.9}$$

$$k_4 = 0.5k_0 \sec^2\theta\left[1-2\tau\cos\theta+\sqrt{1-4\tau\cos\theta}\right] \tag{9.10}$$

with the reduced frequency, $\tau = U\sigma/g$, and

$$\theta_c = \begin{cases} \cos^{-1}(1/4\tau) & \tau > 0.25 \\ 0 & \tau < 0.25 \end{cases} \tag{9.11}$$

The wave surface elevation is calculated by (5.20):

$$\varsigma = -\frac{P}{\rho g} + \frac{U}{g}\frac{\partial\phi}{\partial x} - \frac{i\sigma}{g}\phi \qquad z = 0 \tag{9.12}$$

Following the approach adopted for the steady flow problem, the cushion area, S_c, is discretized into a number of rectangular patches. The wave surface elevation at a field point (x_j, y_j) will be sum of the contributions from all of the pressure patches. Solution for a rectangular pressure patch located on $\Delta S_i : [\left|x_j-\xi_i\right| \le a;\ \left|y_j-\eta_i\right| \le b]$, with strength $\Pi_0 e^{i\sigma t}$, is the elementary solution for the problem, where Π_0 is constant. The free surface elevation due to a moving and oscillating rectangular pressure patch with unit strength will be (see Appendix C):

$$\varsigma_p(x_j, y_j) = -\frac{\delta_{ji}}{\rho g} - \frac{1}{4\pi^2\rho g}\sum_{m=1}^{8}(-1)^m\left(J_{0m}+J_{1m}+J_{2m}+J_{3m}+J_{4m}+J_{5m}+J_{6m}\right) \tag{9.13}$$

where

$$J_{0m} = \int_0^{\pi/2} \frac{1}{\sin\theta\cos\theta}\ln\left|s_m(\theta)\right| d\theta \tag{9.14}$$

$$J_{1m} = \int_0^{\pi/2} \frac{E_1(ik_1 s_m)}{\sin\theta\cos\theta\sqrt{1+4\tau\cos\theta}} e^{ik_1 s_m} d\theta$$

$$-i\pi \int_0^{\pi/2} \frac{(1-\mathrm{sgn}(s_m))}{\sin\theta\cos\theta\sqrt{1+4\tau\cos\theta}} e^{ik_1 s_m} d\theta \tag{9.15}$$

$$J_{2m} = \int_0^{\pi/2} \frac{E_1(ik_2 s_m)}{\sin\theta\cos\theta\sqrt{1+4\tau\cos\theta}} e^{ik_2 s_m} d\theta$$

$$+i\pi\int_{0}^{\pi/2}\frac{(1-\mathrm{sgn}(s_m))}{\sin\theta\cos\theta\sqrt{1+4\tau\cos\theta}}e^{ik_2 s_m}d\theta \tag{9.16}$$

$$J_{3m}=\int_{\theta_c}^{\pi/2}\frac{E_1(-ik_3 s_m)}{\sin\theta\cos\theta\sqrt{1-4\tau\cos\theta}}e^{-ik_3 s_m}d\theta$$

$$-\pi\int_{\theta_c}^{\pi/2}\frac{\sin(k_3 s_m)[1+sgn(s_m)]}{\sin\theta\cos\theta\sqrt{1-4\tau\cos\theta}}d\theta$$

$$-i\pi\int_{\theta_c}^{\pi/2}\frac{\cos(k_3 s_m)[1+sgn(s_m)]}{\sin\theta\cos\theta\sqrt{1-4\tau\cos\theta}}d\theta \tag{9.17}$$

$$J_{4m}=-\int_{\theta_c}^{\pi/2}\frac{E_1(-ik_4 s_m)}{\sin\theta\cos\theta\sqrt{1-4\tau\cos\theta}}e^{-ik_4 s_m}d\theta$$

$$-\pi\int_{\theta_c}^{\pi/2}\frac{\sin(k_4 s_m)[1-sgn(s_m)]}{\sin\theta\cos\theta\sqrt{1-4\tau\cos\theta}}d\theta$$

$$-i\pi\int_{\theta_c}^{\pi/2}\frac{\cos(k_4 s_m)[1-sgn(s_m)]}{\sin\theta\cos\theta\sqrt{1-4\tau\cos\theta}}d\theta \tag{9.18}$$

$$J_{5m}=-i\int_{0}^{\theta_c}\frac{E_1(-ik_3 s_m)}{\sin\theta\cos\theta\sqrt{4\tau\cos\theta-1}}e^{-ik_3 s_m}d\theta$$

$$-\frac{\pi}{2}\int_{0}^{\theta_c}\frac{\cos(k_{3r}s_m)[1+\mathrm{sgn}(s_m)][1+\mathrm{sgn}(k_{3r})]}{\sin\theta\cos\theta\sqrt{4\tau\cos\theta-1}}e^{k_{3i}s_m}d\theta$$

$$+\frac{i\pi}{2}\int_{0}^{\theta_c}\frac{\sin(k_{3r}s_m)[1+\mathrm{sgn}(s_m)][1+\mathrm{sgn}(k_{3r})]}{\sin\theta\cos\theta\sqrt{4\tau\cos\theta-1}}e^{k_{3i}s_m}d\theta \tag{9.19}$$

$$J_{6m}=i\int_{0}^{\theta_c}\frac{E_1(-ik_4 s_m)}{\sin\theta\cos\theta\sqrt{4\tau\cos\theta-1}}e^{-ik_4 s_m}d\theta$$

$$-\frac{\pi}{2}\int_{0}^{\theta_c}\frac{\cos(k_{4r}s_m)[1-\mathrm{sgn}(s_m)][1+\mathrm{sgn}(k_{4r})]}{\sin\theta\cos\theta\sqrt{4\tau\cos\theta-1}}e^{k_{4i}s_m}d\theta$$

$$+\frac{i\pi}{2}\int_{0}^{\theta_c}\frac{\sin(k_{4r}s_m)[1-\mathrm{sgn}(s_m)][1+\mathrm{sgn}(k_{4r})]}{\sin\theta\cos\theta\sqrt{4\tau\cos\theta-1}}e^{k_{4i}s_m}d\theta \tag{9.20}$$

and $s_m(\theta), m=1,2,...,8$, is defined in (6.11). The static pressure is discontinuous along the periphery of the pressure patch. The value of discontinuities is defined as

$$\Pi_0(\pm a, y)=[\Pi_0(\pm a+0, y)+\Pi_0(\pm a-0, y)]/2 \tag{9.21}$$

At the corner, $\Pi_0(\pm a+0, \pm b\mp 0)=0.25\Pi_0(\pm a, \pm b)$. Hence, the total non-dimensional elevation is obtained by adding the following to the dynamic term:

$$\frac{\rho g \varsigma_{\text{static}}}{\Pi_0} = \begin{cases} -0.5 & |x| = a \text{ or } |y| = b \\ -1.0 & |x| < a, \ |y| < b \\ -0.25 & \text{at corners} \end{cases} \tag{9.22}$$

It is noticed that

$$\lim_{\theta \to \pi/2} \{k_1\} = \frac{\sigma^2}{g} \qquad \lim_{\theta \to \pi/2} \{k_2\} = +\infty \tag{9.23}$$

$$\lim_{\theta \to \pi/2} \{k_3\} = \frac{\sigma^2}{g} \qquad \lim_{\theta \to \pi/2} \{k_4\} = +\infty \tag{9.24}$$

The wave system in (9.14) is a local wave and non-oscillatory component. This local wave will disappear at the far field from the pressure patch. The first terms in (9.15) and (9.16) are local waves as well. The second terms in (9.15) and (9.16) are wave terms. These waves propagate down stream from the pressure patch in a wedge-shaped region, and the wave relating to k_2 travels faster than the wave relating to k_1. There will be transverse and divergent wave components. When $\tau > 1/4$, the wave components relating to wave number k_3 and k_4 are local waves. When $\tau < 1/4$ (i.e., $\theta_c = 0$), the first terms in (9.17) and (9.18) are local waves, the remaining terms are the wave terms. The propagating wave relating to wave number k_4 is behind the moving pressure patch and its direction is the same as the direction of moving pressure. Waves relating to k_3 will propagate up-stream, but this wave is relatively small. A detailed analysis of the unsteady wave system can be found in Chen et al. (1999) and Chen et al. 2001).

9.2 Numerical Methods

Evaluation of the free surface elevation (9.13) is hampered by the singularities in the integrand of $J_{i,m}$ and by their highly oscillatory behaviour. For example, the integrand of J_{0m} becomes infinite when $\theta \to 0$ and $\theta \to \pi/2$; also $k_2 s_m \to \pm\infty$ as $\theta \to \pi/2$. To overcome these difficulties, we write the integrand as $F_{i,m}(\theta) = f_{i,m}(\theta)/g_{i,m}(\theta)$, where $f_{i,m}(\theta)$ is regular and $g_{i,m}(\theta)$ has a zero of order one at $\theta = \theta_a$. Thus the integral of $F_{i,m}(\theta)$ may be written as

$$J_{i,m} = \int_{\theta_a}^{\theta_b} \frac{f_{i,m}(\theta)}{g_{i,m}(\theta)} d\theta = \int_{\theta_a}^{\theta_b} \left[\frac{f_{i,m}(\theta)}{g_{i,m}(\theta)} - \frac{f_{i,m}(\theta_a)}{g'_{i,m}(\theta_a)(\theta-\theta_a)} \right] d\theta + \int_{\theta_a}^{\theta_b} \left[\frac{f_{i,m}(\theta_a)}{g'_{i,m}(\theta_a)(\theta-\theta_a)} \right] d\theta \qquad (9.25)$$

On the right hand side of (9.25), it is observed that the integrand of the first integral is regular at $\theta = \theta_a$. It can also be shown that the second integral makes no contribution after summation for all $m's$ in (9.13). The same approach can be applied to the cases of $\theta = \theta_b$. In this way, the singularities in the integrals of the free surface elevation can be removed.

For J_{3m}, J_{4m}, J_{5m} and J_{6m}, there is a singularity of order ½ at $\theta = \theta_c$, which is theoretically integrable:

$$\sqrt{1-4\tau\cos\theta} = \sqrt{\frac{2}{\tau}} \sqrt{\sin\left(\frac{\theta+\theta_c}{2}\right)} \sqrt{\sin\left(\frac{\theta-\theta_c}{2}\right)} \qquad (9.26)$$

where $\theta \in (\theta_c, \pi/2)$. A direct integration scheme can be used to calculate $J_{0m}, J_{1m}, J_{3m}, J_{5m}$ and J_{6m} in (9.13).

It then remains to calculate J_{2m} and J_{4m}. The integrands becomes highly oscillatory when $\theta \to \pi/2$. To stretch the integrands, the same variable changes as equation (6.17), which is reproduced here:

$$u = \begin{cases} |\gamma| \dfrac{\sin\theta}{\cos^2\theta} & m = 1,4,6,7 \\ |\delta| \dfrac{\sin\theta}{\cos^2\theta} & m = 2,3,5,8 \end{cases} \qquad (6.17)$$

By doing this, the highly oscillatory integrands in (9.16) and (9.18) are stretched. For example:

$$t_{21} = k_2 s_1 = \psi(\theta) \left[\frac{\sqrt{2}\alpha u}{\sqrt{|\gamma| \sqrt{4u^2+\gamma^2} - \gamma^2}} + \frac{|\gamma|}{\gamma} u \right] \qquad (9.27)$$

where $\psi(\theta)$ is a regular function of θ (and also of u as well):

$$\psi(\theta) = \frac{1}{2}\left(1 + 2\tau\cos\theta + \sqrt{1+4\tau\cos\theta}\right) \qquad (9.28)$$

therefore

$$\lim_{\theta\to\pi/2} \{t_{2m}\} = \lim_{\theta\to\pi/2} \{k_2(\theta) s_m(\theta)\} = \lim_{u\to\infty} \{k_2(u) s_m(u)\} \propto \pm u \qquad (9.29)$$

(9.16) becomes

$$J_{2m} = -\int_0^\infty \frac{2u[E_1(it_{2m}) - i\pi(1-\operatorname{sgn}(s_m))]}{\left(4u^2+\gamma^2-|\gamma|\sqrt{4u^2+\gamma^2}\right)\sqrt{1+4\tau\cos\theta(u)}} e^{it_{2m}} du \qquad m = 1,4,6,7 \qquad (9.30)$$

$$J_{2m} = -\int_0^\infty \frac{2u[E_1(it_{2m}) - i\pi(1-\operatorname{sgn}(s_m))]}{\left(4u^2+\delta^2-|\delta|\sqrt{4u^2+\delta^2}\right)\sqrt{1+4\tau\cos\theta(u)}} e^{it_{2m}} du \qquad m = 2,3,5,8 \qquad (9.31)$$

Equations (9.30) and (9.31) are now easy to facilitate numerical integration. Similar formulations can be derived for (9.18). Care is also advised when handling the logarithmic singularity in the integrals of (9.14) ~ (9.20) as for the steady flow problem in Chapter 6. For the cases of $\gamma = 0$ or $\delta = 0$, which means at the boundary of the pressure patch ($y = \eta + b$ or $y = \eta - b$), one can leave those terms whose $s_m(\theta)$ are the same and their contributions counteract each other, the same procedure can be applied.

The escape area of a rectangular pressure patch is defined as the area under the free surface elevation at the stern side of the pressure patch:

$$\alpha_p(\sigma) = \int_{-b}^{b} \varsigma_p(-a, y, \sigma) dy \qquad (9.32)$$

The escape volume is defined as the volume of the free surface elevation over the pressure patch:

$$v_p(\sigma) = \int_{-a}^{a}\int_{-b}^{b} \varsigma_p(x, y, \sigma) dx dy \qquad (9.33)$$

A number of convergence studies have been carried out in order to find the proper numerical scheme for the free surface elevations generated by the moving and oscillating pressure patch. A rectangular pressure patch is selected for validation of the numerical scheme outlined above. The length-beam ratio of the pressure patch is $a/b = 1$, and the patch length Froude number is $fn = 0.5$. The free surface elevations of the rectangular pressure patch at reduced frequencies of $\tau = 0.2375$ and 0.275 (below and above the critical value of $\tau = 0.25$) are compared with an existing results. Due to the phase effect, there are real (Re) and imaginary (Im) parts for the free surface elevation. Wave cuts at $y = b$ and the escape area at the stern ($x = -a$) were compared with those of Doctors (1975), who used a different numerical scheme.

The comparisons of the wave cut are shown in Figure 9.1 and 9.2. The agreements are very satisfactory. Comparison of the escape area against the reduced frequency is shown in Figure 9.3 for the same pressure patch. Both real and imaginary parts agree well with those of Doctors prediction. The calculated escape volume of a rectangular pressure patch with $b/a = 0.156$ at $Fn = 0.72$ is compared with those of Nakos et al. (1991). The agreement is also satisfactory. The non-dimensional free surface elevation, escape area and escape volume per unit pressure are defined as

$$\tilde{\varsigma}_p = \rho g \varsigma_p \tag{9.34}$$

$$\tilde{\alpha}_p = \frac{\rho g \alpha_p}{L} \tag{9.35}$$

$$\tilde{v}_p = \frac{\rho g v_p}{L^2} \tag{9.36}$$

Respectively, where $L(=2a)$ is length of the pressure patch.

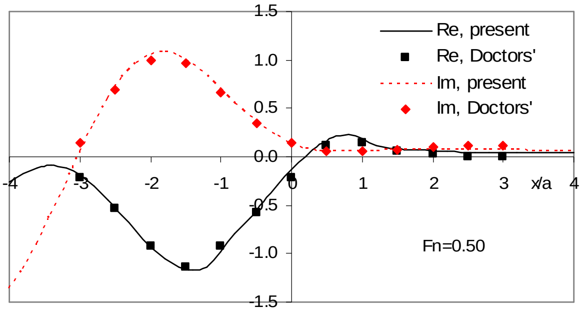

Figure 9.1 Non-dimensional free surface elevation at $y = 0$ for a rectangular pressure patch $b/a = 1, \tau = 0.2375$

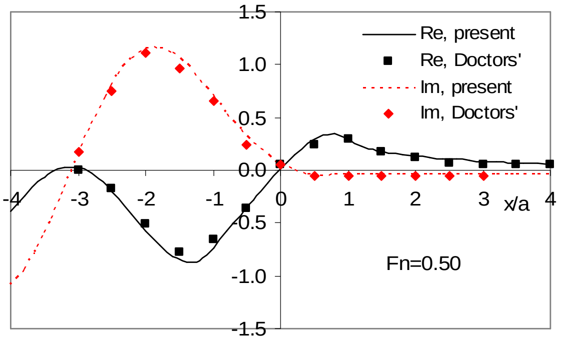

Figure 9.2 Non-dimensional free surface elevation at $y = b$ for a rectangular pressure patch $b/a = 1, \tau = 0.275$

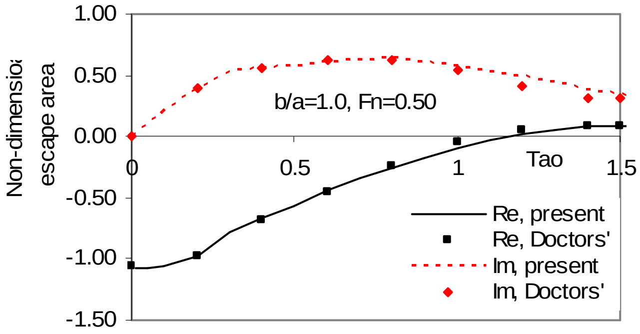

Figure 9.3 Non-dimensional escape area at $x = -a$ for a rectangular pressure patch $b/a = 1, Fn = 0.5$

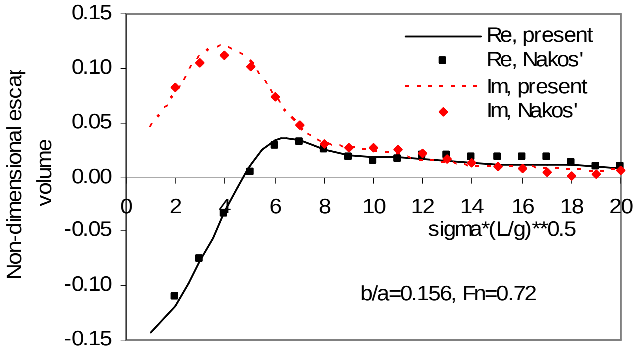

Figure 9.4 Non-dimensional escape volume at $x = -a$ for a rectangular pressure patch $b/a = 0.156, Fn = 0.72$

9.3 Equation of Motions

In Chapter 5, equations of motions for the ASV have been derived, see equation (5.68). The unknown cushion pressure(s) is included in those equations. In order to make the problem complete, an additional equation for the cushion pressure is needed. It is assumed that amplitudes of the incident wave and motions of the vessel are small. The external forces/moments acting on the vessel are the pressure force in the cushion chamber and the hydrodynamic force on the wetted rigid hull due to the incident wave, diffraction and radiation waves. There is also a hydrostatic restoring force. The hydrodynamic force can be calculated by a method for a conventional ship. If the wetted rigid side hulls are slender bodies, a strip theory may be used (Salvesen, Tuck and Faltinsen, 1970). For a more general hull design, a rational 3D diffraction/radiation approach will be needed (see for example, Sclavounos et al., 2003, Xie et al., 2012).

We will also focus our attention on heave, pitch and roll motions to simplify the analysis. Normally, these are the main motion modes for the vessel in waves which cause comfort and operational problems. The equation of motions of the ASV can be written as

$$[\mathbf{M}][\ddot{\mathbf{q}}] = [\mathbf{F_h}] + [\mathbf{F_p}] \tag{9.37}$$

where $\mathbf{M}$ is the mass/inertia matrix, $\mathbf{q}$ is motion vector of the vessel, $\mathbf{F_h}$ is the external hydrodynamic force/moment, $\mathbf{F_p}$ is the external force due to the excess pressure in the cushions.

$$F_{h,j} = \iint_{S_0} p_w n_j ds \tag{9.38}$$

$$F_{p,j} = \iint_{\Omega_0} p_c n_j ds \tag{9.39}$$

where p_w is the hydrodynamic pressure on the hull surface, $p_c \ (= P_0 + P)$ is the excess air pressure in the cushion chambers. The hydrodynamic pressure on the wetted part of the rigid hull will be calculated by a diffraction/radiation approach. The hydrodynamic force/moments are

$$F_{h,j} = -\sum_{i=1}^{6} [A_{ji}\ddot{q}_i + B_{ji}\dot{q}_i + C_{ji}q_i] + F_{w,j} \qquad j = 1, 2, ..., 6 \tag{9.40}$$

where $[A_{ji}]$, $[B_{ji}]$ and $[C_{ji}]$ are matrix of the added mass, damping coefficients and restoring coefficients; $F_{w,j}$ is the wave exciting forces/moments.

The cushion excess pressure inside the chambers consists of two components:

$$p_{c,l} = P_0 + P_l(t) = P_0 + \mathrm{Re}\{\tilde{P}_l \ e^{i\sigma t}\} \tag{9.41}$$

where l represents index of cushions of the vessel. For the air dynamic pressure part, the following assumptions are made:

1. The deformation of the free surface under the oscillatory pressure patch in uniform translation is used to display the way in which the motion of the water surface participates in evaluation of the pressure variations in the plenum air;

2. Pressure and volume changes are assumed to occur sufficiently rapidly so that the adiabatic law governs the basic thermodynamic variations in the air cushion;

3. The cushion pressure is spatially homogeneous;

4. The leakage of the air takes place only at the fan and stern apertures;

5. The perturbed pressure and air volume have the same order of magnitudes as the vessel motions.

The adiabatic gas law is applied to the air in the cushion chambers:

$$\frac{P_l(t) + p_a + P_0}{\rho_l^{\gamma}} = \text{constant} \tag{9.42}$$

where $P_l(t)$ is the time-varying part of the cushion pressure (or perturbed pressure); p_a is atmospheric pressure; P_0 is the cushion excess pressure at the equilibrium condition (on-cushion mode); ρ_l is air density inside the cushion and γ is the ratio of specific heat for gas.

On the other hand, the continuity equation for the air in the cushion chambers states

$$V_l \frac{d\rho_l}{dt} + \rho_l \frac{\partial V_l}{\partial t} = \rho_a [Q_{in,l} - Q_{out,l}] \tag{9.43}$$

where $Q_{in,l}$ is the inflow rate of the fan system; $Q_{out,l}$ is the out flow rate; V_l is the cushion volume determined by the vessel motion attitude, the incident wave and the cushion pressure. Substituting (9.42) into (9.43)

$$\frac{V_l \rho_l}{\gamma (P_l + p_a + P_0)} \frac{dP_l}{dt} + \rho_l \frac{\partial V_l}{\partial t} = \rho_a [Q_{in,l}(t) - Q_{out,l}(t)] \tag{9.44}$$

The outflow rate can be expressed as (Kim and Taskonas, 1981, Faltinsen, 2005), omitting cushion chamber index:

$$Q_{out} = c_n A_L \sqrt{\frac{2(P + P_0)}{\rho_a}} \tag{9.45}$$

where $c_n(\approx 0.6 \sim 0.8)$ is the flow coefficient and A_L is the air escape area of the flow opening at the cushion stern boundary. The free surface elevation of the incident wave, $\varsigma_w(x,y,t)$, is:

$$\varsigma_w(x,y,t) = \mathrm{Re}\left\{\varsigma_a e^{-ik(x\cos\beta - y\sin\beta)} e^{i\sigma t}\right\} \tag{9.46}$$

where ς_a is amplitude of the incident wave. Volume of each cushion chamber is

$$V(t) = V_0 + \iint_{S_c} [q_3 + yq_4 - xq_5 - \varsigma_p(x,y,t)p - \varsigma_w(x,y,t)]dxdy \tag{9.47}$$

where V_0 is the cushion volume at the equilibrium condition; $\varsigma_p(x,y,t)$ is the free surface elevation due to cushion pressure. The diffraction and radiation waves inside the cushion chamber due to the rigid side hull are neglected. q_3, q_4 and q_5 are heave, roll and pitch of the vessel, respectively. (9.47) can be further written as:

$$V(t) = V_0 + S_{00}q_3 + S_{01}q_4 - S_{10}q_5 - v_p(t)p - v_w(t) \tag{9.48}$$

where

$$S_{jk} = \iint_{S_c} x^j y^k dxdy \qquad j,k = 0,1 \tag{9.49}$$

are moments of the cushion area; $v_p(t)$ is the cushion escape volume; and v_w is the cushion pumping volume due to the incident wave:

$$v_p(t) = \iint_{S_c} \varsigma_p(x,y,t)dxdy \tag{9.50}$$

$$v_w(t) = \iint_{S_c} \varsigma_w(x,y,t)dxdy \tag{9.51}$$

Physically, the cushion escape volume is volume of the free surface elevation due to cushion pressure inside the cushion chamber of the ASV. The area of the air flow opening at the cushion stern boundary, A_L, is calculated by

$$A_L = A_{L0} + B_T q_3 + y_c B_T q_4 - x_T B_T q_5 - \alpha_p p - \alpha_w \tag{9.52}$$

where A_{L0} is area of the outflow opening at stern of the cushion at equilibrium condition; B_T is the cushion width at stern, x_T is the longitudinal coordinate of the cushion stern aperture, (x_c, y_c) is the cushion area centre; α_p is the escape area per unit pressure

$$\alpha_p(t) = \int_{y_a}^{y_b} \varsigma_p(x_T, y, t)dy \tag{9.53}$$

α_w is the cushion stern escape area due to the incident waves:

$$\alpha_w(t) = \int_{y_a}^{y_b} \varsigma_w(x_T, y, t)dy \tag{9.54}$$

The fan inflow is also expanded in the equilibrium condition:

$$Q_{in,l} = n_f \; Q_{in0,l} + n_f \; \left|\frac{\partial Q_{in,l}}{\partial p}\right| P_l \tag{9.55}$$

$\partial Q_{in} / \partial p$ is the discharge by fan per unit pressure per pair fan, the absolute is taken due to the air flow direction, n_f is number of inflow fans. Substituting (9.48), (9.52), (9.53) and (9.55) into (9.44), and is expanded about the equilibrium position, the linearised cushion pressure equation can be written as (omitting the cushion index l):

$$b_{pp}\dot{P} + c_{pp}P + b_{p3}\dot{q}_3 + c_{p3}q_3 + b_{p5}\dot{q}_5 + c_{p5}q_5 + b_{p4}\dot{q}_4 + c_{p4}q_4 = F_{wp} \tag{9.56}$$

where expression of the coefficients can be found in Appendix A. The equations for heave, pitch and roll of the ASV can be written as:

$$\begin{cases} (m + A_{33})\ddot{q}_3 + B_{33}\dot{q}_3 + C_{33}q_3 + A_{35}\ddot{q}_5 + B_{35}\dot{q}_5 + C_{53}q_5 - S_{00}(P_1 + P_2) = F_{w3} \\ A_{53}\ddot{q}_3 + B_{53}\dot{q}_3 + C_{53}q_3 + (I_{55} + A_{55})\ddot{q}_5 + B_{55}\dot{q}_5 + c_{55}q_5 + S_{10}(P_1 + P_2) = F_{w5} \\ \qquad\qquad (I_{44} + A_{44})\ddot{q}_4 + B_{44}\dot{q}_4 + c_{44}q_4 - S_{01}(P_1 - P_2) = F_{w4} \end{cases} \tag{9.57}$$

where F_{wj} is the wave exciting force/moment, c_{44}, c_{55} are the restoring coefficients for roll and pitch, in which the effect of the cushion pressure is taken into account, see Appendix B for details. The hydrodynamic coefficients and the wave exciting force/moments on the thin rigid side-hull of each cushion can be calculated by a diffraction/radiation method. During the calculations, the vessel is treated as a multi-hull with the same displacement volume as the ASV at on-cushion mode. Solution of (9.56) and (9.57) are the transfer functions for heave, pitch, roll motion of the vessel and the dynamic pressure in the cushion chambers in regular waves:

$$q_j = \mathrm{Re}\left\{\tilde{q}_j e^{i\sigma t}\right\} \qquad j = 3,4,5 \tag{9.58}$$

$$P_l = \mathrm{Re}\left\{\tilde{P}_l e^{i\sigma t}\right\} \tag{9.59}$$

For ship motions in irregular waves, the root mean square (RMS) values are calculated as:

$$RMS_j(\beta) = [\int_0^\infty (\left|\tilde{q}_j(\sigma, \beta)\right| / \varsigma_a)^2 S_\varsigma(\omega)ds]^{1/2} \qquad j = 3,4,5 \tag{9.60}$$

where ω is wave frequency and β is the heading angle. The ITTC wave spectrum is used in the present study:

$$S_\varsigma(\omega) = A\omega^{-5}\exp\left(-B/\omega^4\right) \tag{9.61}$$

where $A = 173.18H_{1/3}^2/T_{01}^4$ and $B = 692.73/T_{01}^4$ with $H_{1/3}$ significant wave height (m) and T_{01} average wave period (s).

9.4 A Case Study for Simplified Model

The equations of motion for an ASV have been derived in the previous section in 3 degrees of freedom including the effect of the rigid side-hulls as well as multiple air chambers. In this section, a simplified version of these equations will be re-derived from the first principles. Heave is the only degree of freedom of motion considered, the effect of the side-hulls is ignored and the excess pressure in the cushion is assumed uniform in space. Despite its limitations, the proposed simplified model captures many important aspects of the response of ASVs in waves, without requiring excessive computational effort

The ASV has one air cushion, and is actually a SES. The vessel has a rectangular cushion with length of L and beam of B. The vessel is travelling in head regular wave with forward speed of U. Equations (9.56) and (9.57) become:

$$b_{pp}\dot{P} + c_{pp}P + b_{p3}\dot{q}_3 + c_{p3}q_3 = F_{wp} \tag{9.62}$$

$$m\ddot{q}_3 = S_{00}P \tag{9.63}$$

where $S_{00} = LB$ is the cushion area, representations of b_{pp}, c_{pp}, b_{p3} and c_{p3} can be found in Appendix A, and

$$F_{wp} = \rho_0\dot{v}_w + c_n\rho_a\alpha_w\sqrt{\frac{2P_0}{\rho_a}} \tag{9.64}$$

where

$$v_w = \frac{B\varsigma_a}{k}\sin(kL/2)e^{i\omega t} \tag{9.65}$$

$$\alpha_w = Be^{ikL/2}e^{i\omega t} \tag{9.66}$$

Here ς_a is amplitude of the incident wave, $k = \omega^2/g$ is the wave number. The complex amplitude of heave motion transfer function is

$$\frac{\tilde{q}_3}{\varsigma_a} = \frac{\tilde{F}_{wp}}{(i\sigma b_{p3} + c_{p3}) - \sigma^2 P_0 (i\sigma b_{pp} + c_{pp})/g} \qquad (9.67)$$

For an application, the predicted response of XR-5 model (Magnuson et al., 1975) is illustrated in Figure 9.5, compared with available model experimental data and the numerical prediction of Nakos et al. (1991). The pressure cushion of the XR-5 is of length 4.22m, width o.66m and height 0.22m and it sustains 94% of the vessel's 143.5kg weight. Details of the fan system can be found in Magnuson et al. (1975).

The agreement between the present prediction and both the model experimental data and that of Nakos' numerical results is satisfactory. No resonance is predicted by either the numerical models or the experimental data in the considered range of frequencies.

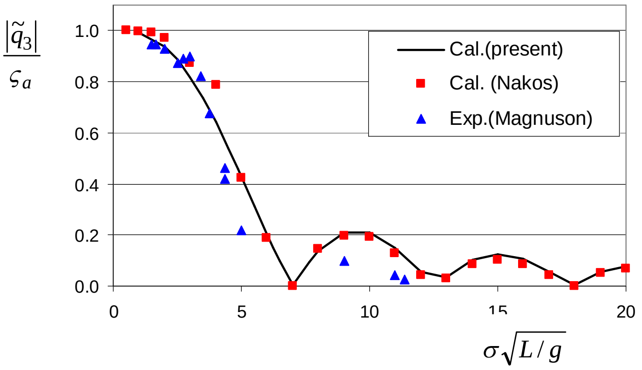

Figure 9.5 Heave amplitude transfer function of a SES (XR-5) in head regular waves at $Fn = 0.72$

9.5 Summary

In this Chapter, a numerical method for evaluation of the free surface elevation generated by a pulsating and moving pressure patch on the free surface is presented. The numerical calculations are humped by the singularities and highly oscillatory behaviour of the integrands. New and reliable numerical schemes are presented for those calculations. The present approach effectively overcame those difficulties. The results obtained by present method are compared with other published data and a good agreement has been found, which shows effectiveness of the present approach.

With the wave surface elevation due to cushion pressure, the coupled equations of motions for the ASV are derived in the frequency domain by utilising the adiabatic gas law in the cushion chamber(s). The hydrodynamic forces/moments can be calculated by a diffraction/radiation approach. These motion equations form the basis for the seakeeping analysis of the ASV in frequency domain in waves. The numerical validation is demonstrated with a case study of a simplified model for one degree of freedom of motion (heave) in regular head waves. The solution of wave surface elevation generated by a moving and pulsating pressure is also essential for the time domain simulation, which involves application of impulse response function technique as described in Chapter 11.

Chapter 10 Case Study – Seakeeping Prediction of the ASV

In this Chapter, the elementary solution of a pulsating and moving pressure patch on the free surface in Chapter 9 is used to predict the seakeeping performance for an ASV, the ALV, E40, in frequency domain. Numerical results are provided and discussed.

10.1 The Air Lifted Vessel, E40

The ALV is an Air Supported Vessel with a relatively higher excess pressure in the cushions and a high design speed. There are two demihulls, each of which contains an air cushion and two fan systems. A forward planing surface ahead of the step creates some limited dynamic lift. The step and the forward planing surface also create the forward sealing of the air cushion chamber, the step being located in a plane close to horizontal (no part of the step is to ventilate before the other). The bow section is slender in order to reduce displacement forces in a seaway, and the bow incorporates a voluminous part above a built-in chine/spray rail to reduce deflection and reserve buoyancy in pitching motion. The side keels of varying height extend from just ahead of the step to the transom. The height of the keels is adjusted to the observed/expected shape of the air cushion. The only purpose of the side keels is to fence in the air cushion. There are spray rails on the outside of the side keels, at a height partly to deflect the water without wetting the rails on the upper sides. The cushion ceiling is at a height to avoid the sea hitting it when the vessel is moving in a seaway. There is a slope of ceiling aft end in order to deflect passing waves in a seaway. A flap or enclosure arrangement in line with the sloped portion of the ceiling is arranged to fence the air cushion chambers in the rear part and to create dynamic lift and motion damping. The air cushion concept of the ALV is patented. Details of the vessel can be found in Allenstrom, Liljenberg and Tudem, (2001, 2003). Figures 10.1 ~ 10.2 are the over views of the craft, and Figure 10.3 shows the body plan. Table 10.1 presents the main particulars of the craft, whilst Table 10.2 summaries the parameters for the air cushion system.

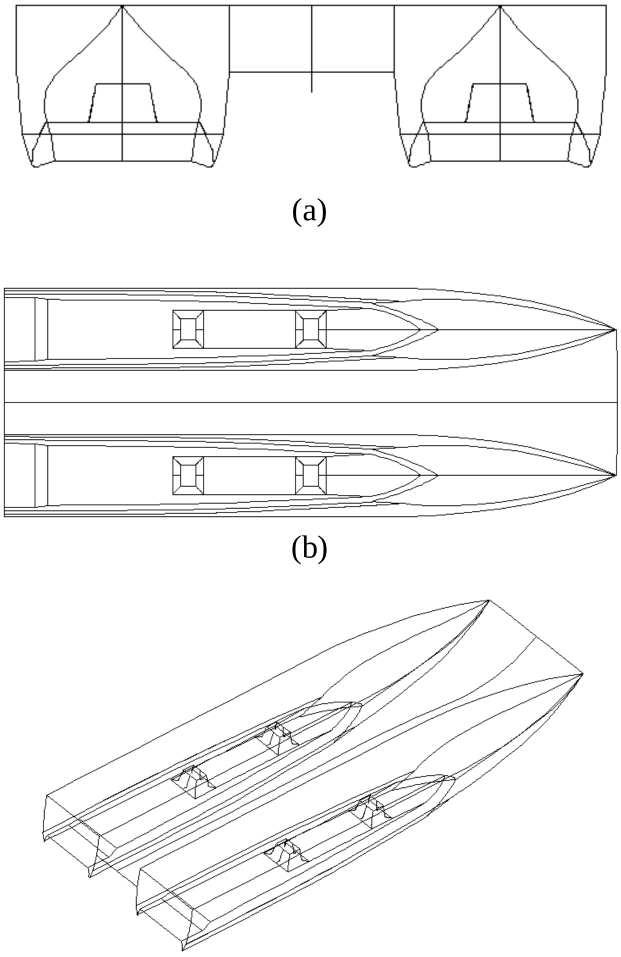

(a)

(b)

c)

Figure 10.1 The Air Lifted Vessel (ALV): a) stern view; b) bottom view; c) bird’s view

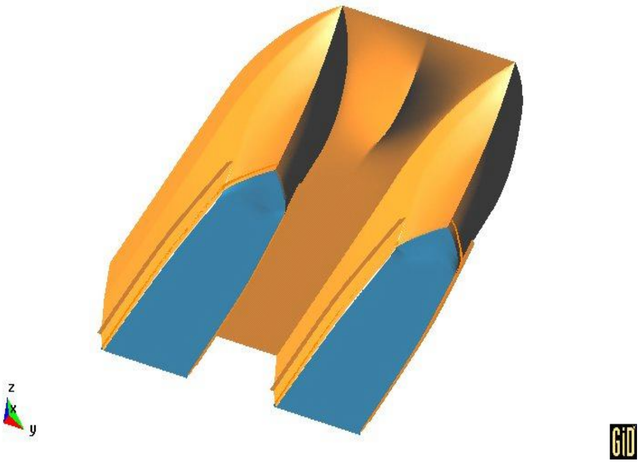

Figure 10.2 The Air Lifted Vessel concept

Table 10.1 Principal particulars of the ALV, E40

length	L_{OA} (m)	40
cushion length	L (m)	25.5
displacement	Δ (ton)	175
breadth	B (m)	15.0
main deck depth	D_m (m)	4.0
draft (off-cushion)	T_{off} (m)	2.0
draft (on-cushion)	T_{on} (m)	1.5
centre of gravity	KG (m)	4.0
separation	S_p (m)	9.60
cushion beam	B_c (m)	3.82
cushion height	H_c (m)	1.0
cushion centre	x_c (m)	-0.03

Table 10.2 Parameters for the air cushion system

Equilibrium cushion pressure	P_0	(N/m^2)	7600
Equilibrium flow rate	Q_{in0}	(m^3/s)	35
Slope of fan inflow rate	$\left\|\partial Q_{in}/\partial p\right\|_0$	$(m^5/N\cdot s)$	0.000591
Cushion area for a demi-hull	A_c	(m^2)	103.7
Static volume for each cushion	V_0	(m^3)	51.85
Number of fans each chamber	n_f	-	2
Flow coefficient	c_n	-	0.61
Ratio of specific heat for gas	γ	-	1.40

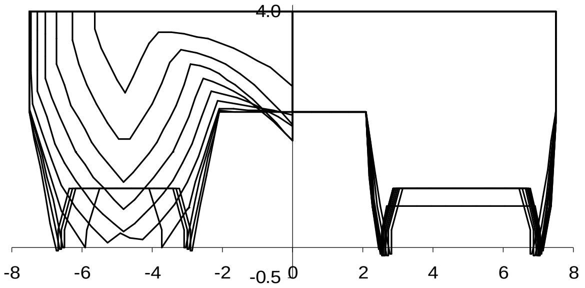

Figure 10.3 Body-plan of the ALV E40

10.2 Seakeeping Analysis of the ALV in Frequency Domain

In this section, a prediction for motion responses of the ALV in waves in frequency domain will be carried out by using the methods developed in Chapter 9. As a case study, the ALV E40 is selected for the calculations. It is a high speed passenger ferry designed by Tudem Ulf Stephen, SES Europe AS, Norway, (2003).

The unsteady wave field generated by the vessel will be similar to that of waves generated by a pulsating and moving pressure patch. When $\tau = U\sigma / g > 1/4$, the propagate wave will confined within a wedge-shaped region behind the vessel; for $\tau = U\sigma / g < 1/4$, there will also be waves travelling up-stream. The unsteady free surface wave can be represented as

$$\varsigma_p(x,y,t) = \mathrm{Re}\{[\varsigma_{pR}(x,y,\tau) + \mathrm{i}\varsigma_{pI}(x,y,\tau)]e^{i\sigma t}\} = \varsigma_{pR}(x,y,\tau)\cos\sigma t - \varsigma_{pI}(x,y,\tau)\sin\sigma t \tag{10.1}$$

where $\varsigma_{pR}(x,y,\tau)$ and $\varsigma_{pI}(x,y,\tau)$ are real and imaginary parts of the transfer function of the free surface elevation, respectively. Figure 10.4 and 10.5 illustrate the perspective views of the unsteady wave fields system for a vessel advancing at $Fn = U/\sqrt{gL} = 0.50, 1.50$ and oscillating at frequencies $\sigma' = \sigma\sqrt{L/g} = 1.0, 5.0$. All the waves are behind the vessel and confined in a wedge-shaped region. The angle of the wedge depends on the oscillating frequency and Froude number. For Froude number $Fn = 0.50$, there are divergent and transverse wave systems at a lower oscillating frequency ($\sigma' = \sigma\sqrt{L/g} = 1.0$); while at a higher oscillating frequency ($\sigma' = 5.0$), only divergent waves exist. For a high Froude number ($Fn = 1.50$), there is no transverse waves in the wave systems for both oscillating frequencies. It is also observed that the angle of the wedge for a lower oscillating frequency is larger than that for a higher oscillating frequency. Also, angles of the wedge are smaller for a high speed

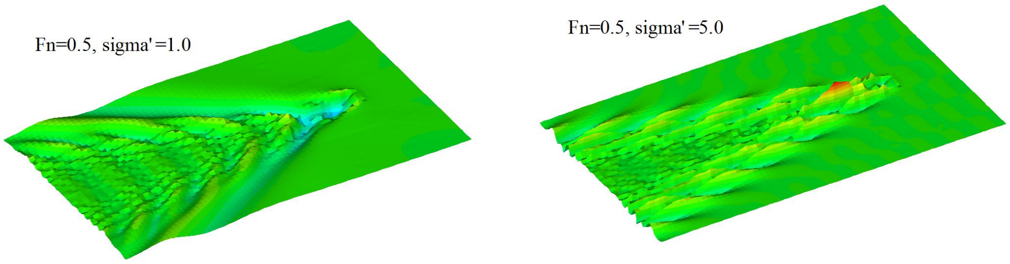

Figure 10.4 Snapshots of the unsteady wave fields for $Fn = 0.50$ at $\sigma' = 1.0$ and $\sigma' = 5.0$

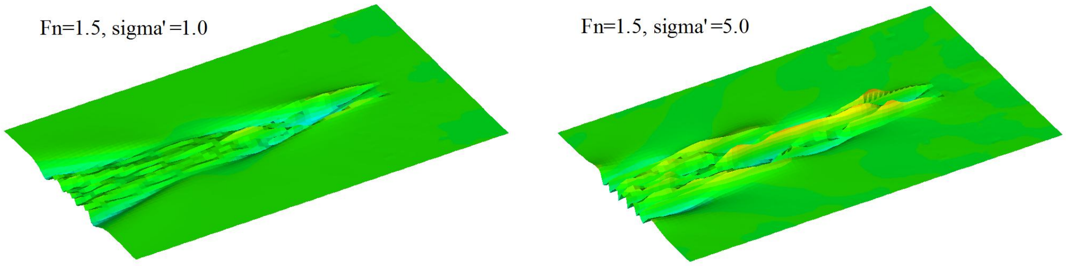

Figure 10.5 Snapshots of the unsteady wave fields for $Fn=1.50$ at $\sigma'=1.0$ and $\sigma'=5.0$

The major part of the computational effort is the numerical calculation of the escape volume in the cushion, equation (9.50), and the escape area at the leakage openings, equation (9.53). When calculating the transfer function of the free surface elevation due to the cushion pressure, the cushion areas are represented by a number of rectangular pressure patches, Figure 10.6.

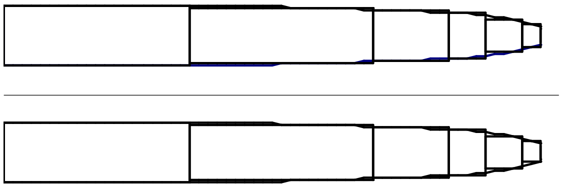

Figure 10.6 Representation of the cushion area of the ALV, E40

Figures 10.7 and 10.8 show real ($\varsigma_{pR}(x,y_b,\tau)$) and imaginary ($\varsigma_{pI}(x,y_b,\tau)$) parts of the non-dimensional free surface elevation against the reduced frequency at the cushion longitudinal outer boundary at Froude number $Fn=0.5$, respectively. It is observed that the free surface elevations have larger response at the lower reduced frequencies. As the reduced frequency increases, the free surface elevation decreases. Figures 10.9 and 10.10 are the non-dimensional free surface elevations at stern boundary ($x=x_T$) of the air cushion of the ALV at Froude number $Fn=1.0$.

It can be seen from these figures that the calculated free surface elevation is smooth both in space and reduced frequency due to proper handling of the singularities and the high oscillating behaviour with the present numerical scheme. Previously published results were either for lower reduced frequencies or lower Froude numbers. It can be also observed that the free surface elevations decrease as the reduced frequency (τ) increases, which means that the free surface elevation responses much less at a high reduced frequency.

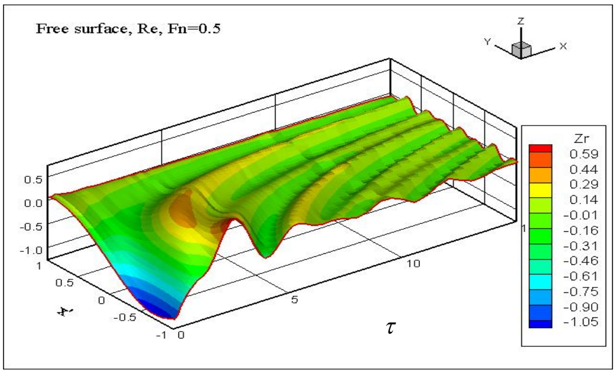

Figure 10.7 Real part of $\tilde{\varsigma}_p$ at the cushion outer boundary of the ALV, E40

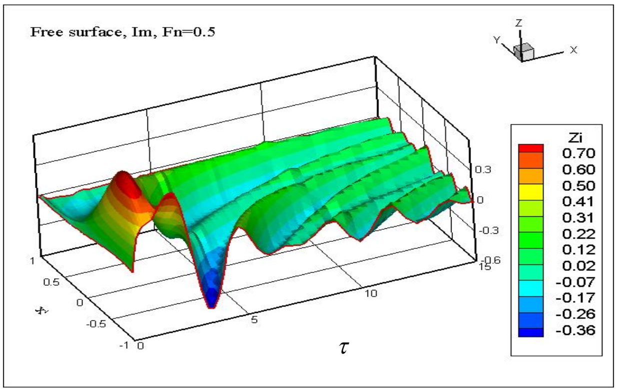

Figure 10.8 Imaginary part of $\tilde{\varsigma}_p$ at the cushion outer boundary of the ALV, E40

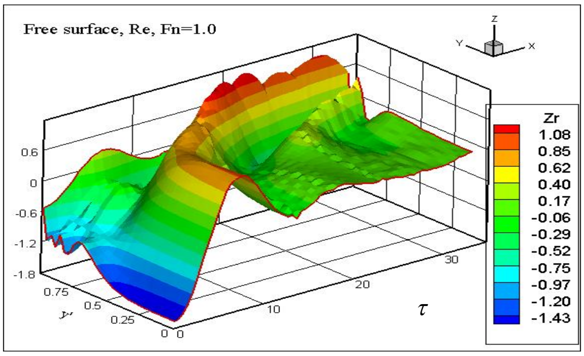

Figure 10.9 Real part of $\tilde{\varsigma}_p$ at cushion stern boundary of the ALV, E40

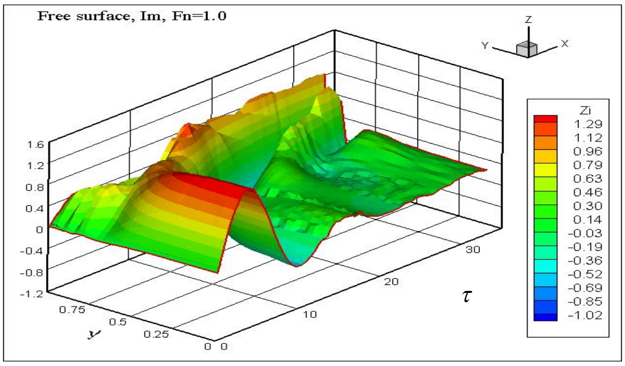

Figure 10.10 Imaginary part of $\tilde{\varsigma}_p$ at cushion stern boundary of the ALV, E40

The calculated non-dimensional escape areas against the non-dimensional encounter frequency at the stern opening of the ALV for Froude numbers $Fn = 0.5,\ 1.0,\ 1.5$ are shown in Figures 10.11 ~ 10.12, respectively. Both results for the demi-hull and the twin-hull are given. In the twin hull calculation cases, the effect of interaction between the demi-hulls on the free surface elevation is taken into consideration. It can be seen that the demi-hulls have some interaction effect on the escape area for $Fn = 0.5$ and at lower encounter frequencies. As the vessel speed increases, this effect become much less and may be neglected. The escape areas decay quickly with increasing encounter frequency. Also the magnitude of the escape area at lower Froude number is larger than those at higher Froude numbers. At very high frequencies, there is nearly no free surface elevation response at all, like a flat surface. Since the craft is normally operating at high speed, this may probably be one of the reasons that the craft has a good seakeeping performance.

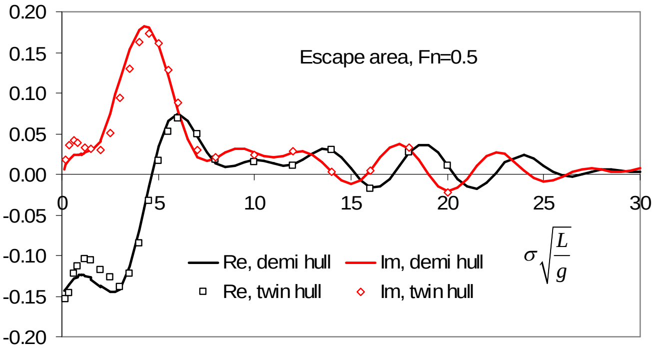

Figure 10.11 Non-dimensional escape area $\tilde{\alpha}_p$ at the stern of the ALV, E40

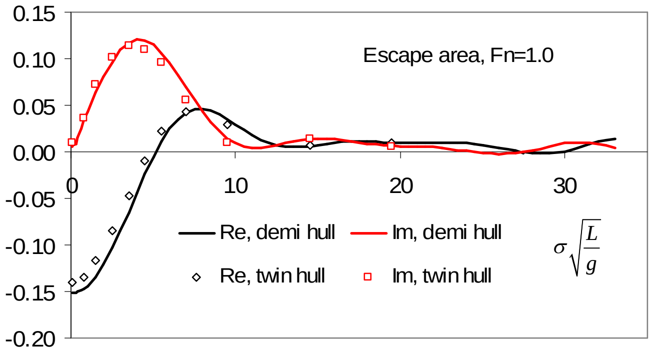

Figure 10.12 Non-dimensional escape area $\tilde{\alpha}_p$ at the stern of the ALV, E40

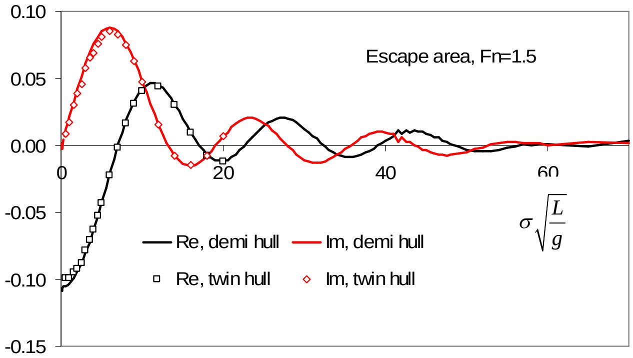

Figure 10.13 Non-dimensional escape area $\tilde{\alpha}_p$ at the stern of the ALV, E40

The cushion escape volumes of the ALV for Froude numbers $Fn = 0.5,\ 1.0,\ 2.0$ are shown in Figures 10.14 ~ 10.15, respectively. The trends are similar to that of the escape area. There will be less free surface disturbance inside the air cushions at higher vessel speeds and high frequencies.

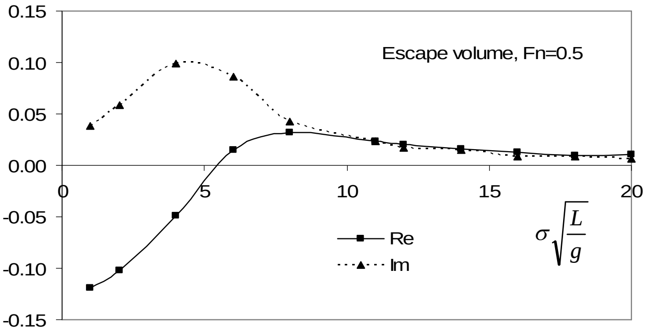

Figure 10.14 Non-dimensional escape volume $\tilde{v}_p$ of the ALV, E40

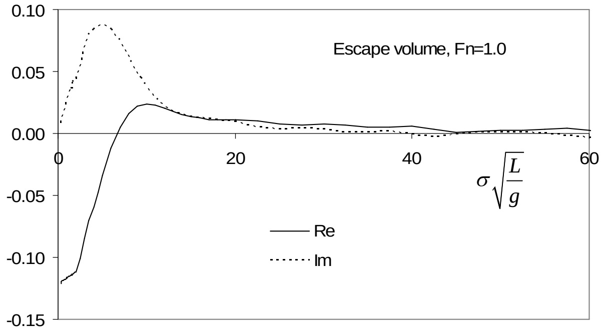

Figure 10.15 Non-dimensional escape volume $\tilde{v}_p$ of the ALV, E40

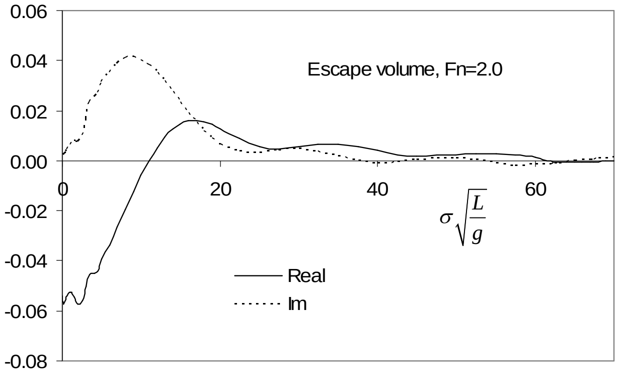

Figure 10.16 Non-dimensional escape volume $\tilde{v}_p$ of the ALV, E40

The hydrodynamic coefficients and the wave excitation force of the rigid side hulls in equation (9.57) are calculated by a 2D strip method (Jasionowski, 2001). This is justified by the fact that the rigid side hulls are slender bodies and the major part of the vessel weight is supported by the air cushion. With the computed escape area and escape volume, motion transfer functions for heave, pitch and roll of the vehicle can be obtained by solving equations (9.56) and (9.57). Responses in irregular waves are calculated by equation (9.60).

There is no model test result available for the motion transfer functions in regular waves for the ALV. Allenstrom et al. (2003) reported a seakeeping model test in irregular head waves in a towing tank. The vertical accelerations at station 16 (bow) were measured during the test. A comparison with the present prediction is made and listed in Table 10.3.

Table 10.3 Vertical acceleration at station 16 (bow) of the ALV E40

U(knot)	$H_{1/3}(m)$	$T_z(s)$	Location	a_z(RMS)(m/s^2) (test)	a_z(RMS)(m/s^2) (cal.)
55	0.88	4.0	station 16	2.80	2.43

The RMS of heave, pitch and vertical acceleration on bow of the ALV at $Fn=1.0$ for a series of wave spectra and all heading angles at interval of 30^0 are plotted in Figure 10.17 ~ 10.19, respectively. The mean wave periods are selected as $T_{01}=4s$, $6s$, $8s$ and $10s$; and the significant wave height is $H_{1/3}=1m$. Generally speaking, there will be less craft responses for shorter waves (smaller mean wave periods). Also, the vehicle has less response in head waves than in following seas, this may be due to the characteristics of the free surface elevation, escape area and escape volume of the air cushion of the ALV. At high values of the reduced frequency, both the escape area and the escape volume tend to zero. In this case, the vessel rides the waves.

Figures 10.20 ~ 10.22 show heave and vertical acceleration at bow of the ALV for $Fn=1.5$, respectively. Again, the vertical acceleration on bow in following waves is much larger than those in head waves. Although there is no experimental result available for validation of the approach at this stage, the obtained results seem reasonable.

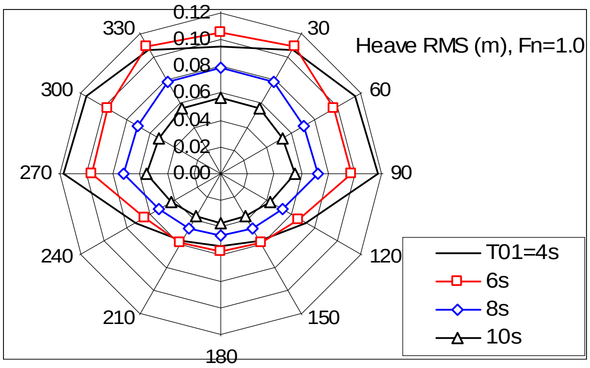

Figure 10.17 RMS of heave motion of the ALV, E40 at $Fn=1.0$ and $H_{1/3}=1m$

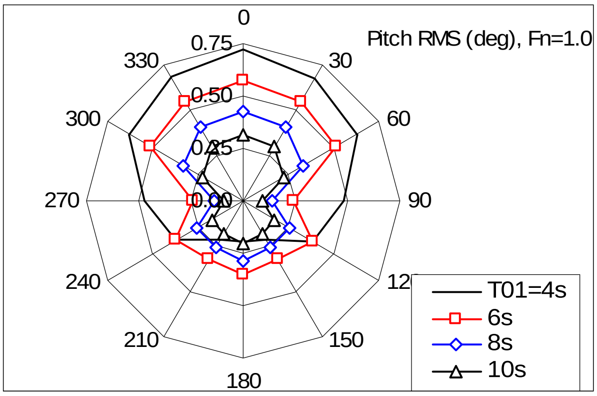

Figure 10.18 RMS of pitch motion of the ALV, E40 at $Fn = 1.0$ and $H_{1/3} = 1m$

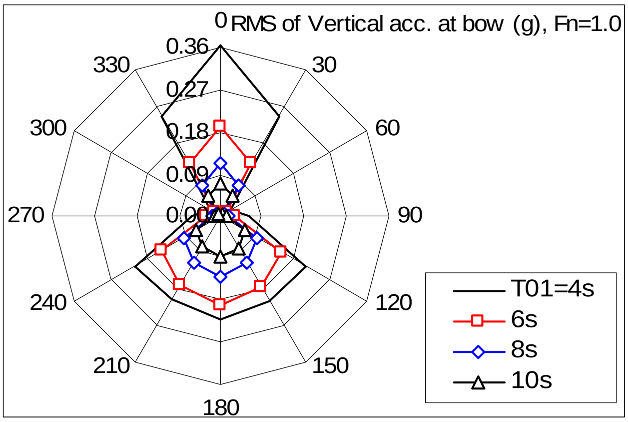

Figure 10.19 RMS of vertical acceleration at bow of the ALV, E40 at $Fn = 1.0$ and $H_{1/3} = 1m$

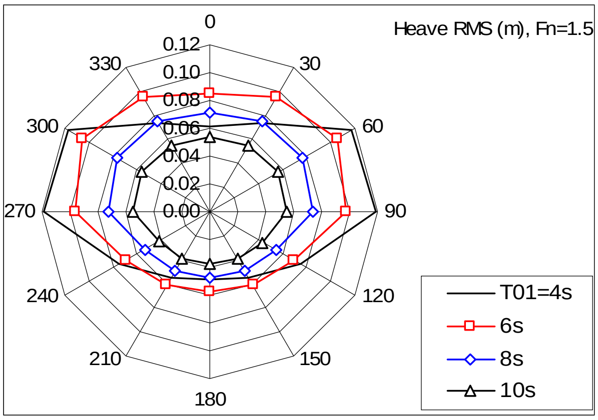

Figure 10.20 RMS of heave motion of the ALV E40 at $Fn = 1.5$ and $H_{1/3} = 1m$

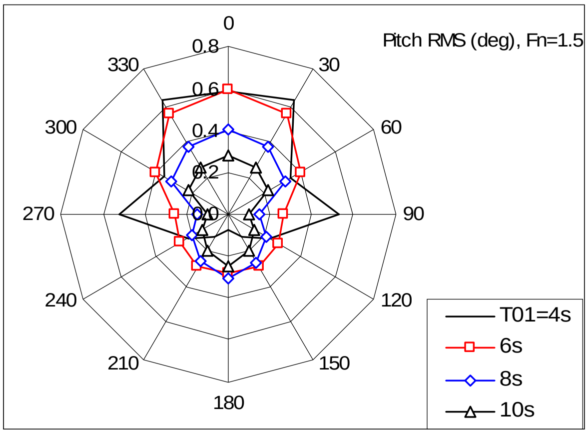

Figure 10.21 RMS of pitch motion of the ALV, E40 at $Fn = 1.5$ and $H_{1/3} = 1m$

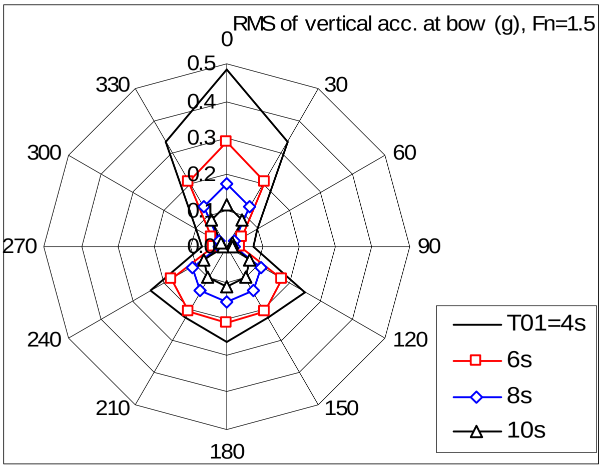

Figure 10.22 RMS of vertical acceleration at bow of the ALV, E40 at $Fn = 1.5$ and $H_{1/3} = 1m$

10.3 Summary

A case study for the seakeeping responses for the ALV, E40, in waves has been carried out in frequency domain. The external forces/moments acting on the hull arise from the hydrodynamic (added mass and damping) loads, the wave excitation – calculated by a strip theory – and the cushion pressure effects. Numerical results for the escape area, escape volume, and for the vessel motions of the ALV are provided and discussed. The present method therefore appears to provide a helpful means of assessing performance at both design and operational stages.

Chapter 11 Stability Analysis

Stability and safety are important issues for an ASV. In this Chapter, a method for the stability analysis in calm water for the ALV will be presented, including the static state transverse stability at zero speed, longitudinal dynamic stability at speed in calm water, the stability in turning and directional stability in calm water. The stability analysis takes into account air compressibility in the cushion chamber. The simulations are carried out in the time domain. Although the analysis is for the ALV, some of it may also be applicable for a general ASV.

11.1 Introduction

The ALV has basically two operational conditions: on-cushion (cushion-borne) mode and off-cushion (hull-borne) mode. Although the major operation of the ALV involves the cushion-borne mode, the hull-borne operation should also be considered. This is necessary as a result of safety and survivability requirements since it is possible that there may be times where a failure occurs in either the lift system or the seals, which would result in the vessel operating in the hull-borne mode. In addition, during very severe sea conditions, it may be necessary for the ALV craft to operate only in the hull-borne mode for survival purposes. Also, there may be certain situations wherein purely hull-borne operation is considered for the vessel, dependent upon the degree of buoyancy initially designed for the sidewalls, for fuel conservation prior to a high-speed on-cushion mode in response to particular commands. In view of all these possibilities, it is necessary to develop appropriate means of analysis and prediction of hull-borne motions in waves. In this case, the method of analysis of hull-borne stability will follow the techniques applied to a conventional displacement ship, see for example, Vassalos et al (2008), and will not be discussed here.

Based on the design features of the vessel, a mathematical model is presented for analysing the longitudinal dynamic stability, the stability in turning and the directional stability of the ALV in calm water. The model takes into account the air compressibility in the cushion (with the adiabatic gas law), and the hydrodynamic forces coupled with the vessel motions. The free surface elevation induced by the excess pressure inside the cushion and at the periphery is represented in the time domain in the form of convolution integrals, whose impulse response functions are calculated by the transfer functions of the moving and pulsating pressure distributions in the frequency domain. The hydrodynamic forces acting on the rigid side-hulls are to be calculated by a diffraction/radiation approach in which the memory effect is also taken into account. The non-linear equations of motion for the vessel are solved using a 4^{th} order Runge-Kutta scheme in time stepping method.

11.2 The Static Transverse Stability

In the steady state condition at speed, the vessel vertical force and moment about the transverse axis that balance the vessel require:

$$\begin{cases} -mg + 2A_cP_0 + \rho g\forall + L_A + L_H = 0 \\ 2x_cA_cP_0 + x_B\rho g\forall + x_{cA}L_A + x_{cH}L_H = 0 \end{cases} \tag{11.1}$$

where m is the mass of the vessel; L_A and L_H are the hydrodynamic lift acting on the hull due to the appendages and hull itself; $\forall$ is the displacement volume; A_c is the cushion area of each demi-hull; P_0 is the mean cushion excess pressure and ρ is water density. x_c, x_B, x_{cA} and x_{cH} are the longitudinal position of the centre of cushion pressure, buoyancy, the appendage lift and the hull lift, respectively.

Model test measurements have shown that the cushion excess pressure decreases with increase of vessel speed, which means that the cushion excess pressure will be lower at higher speed, whilst the dynamic lift force plays a more important role. The two-phase fluid flow around the vessel is complicated and accurate prediction of all those terms is difficult at the present time. Ideally, captive model tests at forward speed should be carried out to measure the dynamic forces and moments acting on the rigid hull, however, this is beyond the scope of the present study. To this end, some empirical formulae are used. The fore body part and the stern flap are assumed to be lifting surfaces with different aspect ratios. The slopes of the lift force coefficients are taken from an aerofoil with finite aspect ratio.

$$L = \frac{\partial C_L}{\partial \alpha} \cdot \alpha \cdot \frac{1}{2} \rho U^2 S_w \tag{11.2}$$

where S_w is the wetted area of the lifting surface; α is the angle of attack; U is the vessel forward speed and C_L is the lifting coefficient. For the stern flap, the vertical and horizontal forces due to the cushion excess pressure are

$$\begin{cases} X_{AP} = P_0 S_{\mathrm{dry}} \cos\gamma \\ Z_{AP} = P_0 S_{\mathrm{dry}} \sin\gamma \end{cases} \tag{11.3}$$

where S_{dry} is the dry area of the flap towards to the cushion, γ is the flap orientation angle. The hydrodynamic force acting on the flap due to the immersed part is calculated with equation (11.2).

The static transverse stability considerations at zero speed, whilst not accurately representative of stability at speed, provide an essential starting point in understanding the stability behaviour of the ALVs. In order to gain some basic understanding of the transverse stability of the ALV, the transverse matecentric height of the ALV at zero speed is evaluated. The procedure follows that for SES (Blyth 1993, Faltinsen, 2005). The contributions of the restoring moment from hydrostatic buoyancy of side hulls and the excess cushion pressure are taken into account. For an ALV with side hulls of approximately constant section and wall-sided body surface at the free surface, the initial transverse matecentric height will be:

$$\overline{GM} = \frac{1}{mg}\left[-A_c P_0 h_0 - mgz_g + \rho g S_{yy} + \rho g \forall z_B\right] \tag{11.4}$$

where h_0 is water head of the cushion excess pressure; A_c is cushion area of a demi-hull; S_{yy} is the transverse moment of inertia of water plane area of the ALV at on-cushion condition. The last two terms in the right hand side of (11.4) represent the transverse matecentric height of a normal catamaran. It can be seen that the excess pressure P_0 in the cushion chamber gives a negative contribution to the matecentric height of the ALV. Details of derivation of (11.4) can be found in Appendix B.

11.3 Longitudinal Dynamic Stability Analysis in Calm Water

When an ALV is travelling in calm water at high speed, analysis of the stability for the craft requires a dynamic model, which is presented in this section. The dynamic behaviour of the vessel can be described as

$$[\mathbf{M}][\ddot{\mathbf{q}}] = [\mathbf{F_H}] + [\mathbf{F_R}] + [\mathbf{F_P}] + [\mathbf{F_A}] \tag{11.5}$$

where $\mathbf{M}$ is the matrix of inertia of the craft; $\mathbf{F}_H$, $\mathbf{F_R}$,$\mathbf{F_P}$ and $\mathbf{F_A}$ are the hydrodynamic force, hydrostatic force, cushion pressure force and appendage force, respectively. The hydrodynamic forces/moments acting on the side halls of the vessel are calculated by a diffraction/radiation method. The added mass and damping coefficients of the demi-hulls in the frequency domain are transferred into a time domain representation by the impulse response function method (Cummins, 1962, Ogilvie, 1964):

$$F_{H,j}(t) = -\sum_{i=1}^{6}[A_{ji}(\infty)\ddot{q}_i(t) + \int_0^t h_{ji}(\tau)\dot{q}_i(t-\tau)d\tau] \tag{11.6}$$

where $A_{ji}(\infty)$ are the added mass of the vessel at infinite frequency, $h_{ji}(\tau)$ are the retardation functions (also referred to as impulse response functions) that can be evaluated as:

$$h_{ji}(\tau) = \frac{2}{\pi}\int_0^\infty B_{ji}(\sigma)\cos\sigma\tau d\sigma = \frac{2}{\pi}\int_0^\infty \sigma[a_{ji}(\sigma) - A_{ji}(\infty)]\sin\sigma\tau d\sigma \tag{11.7}$$

The appendage forces are calculated by an empirical formula, in which a quasi-steady-state assumption has been utilised. In order to get the equation for the pressure in the cushion chamber(s), the adiabatic gas law and the continuity equation in each chamber will be used:

$$\begin{cases} \dfrac{P_l + p_a + P_0}{\rho_l^\gamma} = \dfrac{p_a + P_0}{\rho_0^\gamma} \\ \dfrac{d}{dt}\left(\rho_l V_l\right) = \rho_a\left(Q_{in,l} - Q_{out,l}\right) \end{cases} \tag{11.8}$$

where the subscript l stand for index of the cushion chamber(s); $Q_{in,l}$ is the inflow rate of the fan system, $Q_{out,l}$ is the outflow rate of the cushion chamber. V_l is the instantaneous cushion volume, and is a function of the craft motion and the free surface elevation in the cushions, see (9.47). The inflow flux of each fan system is normally a function of the cushion pressure. The out flow rate is given by

$$Q_{out,l}(t) = c_n A_{L,l}(t)\sqrt{\frac{2(P_l(t)+P_0)}{\rho_a}} \tag{11.9}$$

The instantaneous escape area, $A_{L,l}(t)$, at the periphery of the stern ($x = x_T$) is

$$A_{L,l}(t) = \int_{L,l} \left[\left| z_{r,l}(x_T, y, t) \right| + z_{r,l}(x_T, y, t) \right] dl \tag{11.10}$$

where $z_{r,l}$ is the local relative vertical motion between the hull and the free surface, and is given by

$$z_{r,l}(t) = Z_0 + q_3(t) - x_T q_5(t) - \varsigma_p(t) \tag{11.11}$$

where Z_0 is the gap of the stern opening at the equilibrium condition. By using the principal of the impulse response function, the free surface elevation due to cushion excess pressure is expressed as

$$\begin{cases} \varsigma_p(x,y,t) = \int_0^t h_\varsigma(x,y,\tau) P(t-\tau) d\tau \\ h_\varsigma(x,y,\tau) = \frac{2}{\pi}\int_0^\infty H_{\varsigma,r}(x,y,\sigma)\cos(\sigma\tau) d\sigma \end{cases} \tag{11.12}$$

where $h_\varsigma(x,y,\tau)$ is the impulse response function of the free surface elevation due to a unit cushion pressure. $H_{\varsigma,r}(x,y,\sigma)$ is the real part of the free surface elevation transfer function, $H_\varsigma(x,y,\sigma)$. These transfer functions are calculated by the pressure patch distribution method described in Chapter 9, where the cushion area is discretised into a number of rectangular pressure patches, see, Figure 10.6.

Eliminating ρ_l in (11.8), a differential equation for the cushion excess pressure P_l is obtained as:

$$\frac{dP_l}{dt} = -\frac{\gamma(p_a + P_0 + P_l)}{V_l}\frac{dV_l}{dt} + \frac{\gamma\rho_a(p_a + P_0 + P_l)}{\rho_0 V_l}\left(\frac{p_a + P_0}{p_a + P_0 + P_l}\right)^{1/\gamma}\left(Q_{in,l} - Q_{out,l}\right) \tag{11.13}$$

$l = 1, 2$. For the longitudinal motions (heave and pitch), the excess pressure in the cushion is the same for the port and starboard demi-hulls due to symmetry, so equations (11.13) and (11.5) can be written as (omitting cushion index):

$$\frac{dP}{dt} = \Im_1(t, q_3, \dot{q}_3, q_5, \dot{q}_5, P) \tag{11.14}$$

$$\frac{d\dot{q}_3}{dt} = \Im_3(t, q_3, \dot{q}_3, q_5, \dot{q}_5, P) \tag{11.15}$$

$$\frac{d\dot{q}_5}{dt} = \Im_5(t, q_3, \dot{q}_3, q_5, \dot{q}_5, P) \tag{11.16}$$

Given all the terms in the right hand sides of equation (11.14) ~ (11.16), with the initial conditions for the pressure, displacements and velocities for heave and pitch motions, the coupled non-linear equations for vessel motions and the cushion pressure can be solved numerically in the time domain. A Runge-Kutta scheme is employed for the integration of the differential equations.

11.4 Stability in Manoeuvring in Calm Water

The stability of the ALVs at high speed turning in calm water is an important aspect of the stability performance as required by the IMO High Speed Craft Code. The stability criteria for the intact condition require that a multi-hull craft should have sufficient stability in high speed turning. Annex 7 of the IMO HSC Code, Stability of Multihull Craft, states: when calculating the magnitude of the heel due to the effect of high-speed turning, a high-speed turning lever shall be developed using either the following formula or equivalent method specifically developed for the type of craft under consideration, or trials or model test data (IMO, 2000):

$$TL = \frac{1}{g}\frac{U^2}{R}\left(KG - \frac{d}{2}\right) \tag{11.17}$$

where TL =turning lever (m), U =speed of craft in turning (m/s), R =turning radius (m); KG =height of vertical centre of gravity above keel (m) and d =mean draught (m). In the present study, a mathematical model is presented for predicting the turning radius of the vessel.

Extending the description of craft motions to the horizontal plane with four degrees of freedom, attention is paid to the two translatory motion components along x (surge) and y (sway) axes, and to the two angular motions about $x-$(roll) and $z-$(yaw) axes. The equations of motion in the body-fixed coordinate system are expressed as (Wade and Wang, 1977; Kaplan, 1995):

$$\begin{cases} m(\dot{u}-ru)=X \\ m(\dot{v}+ru)=Y \\ I_x\dot{p}=K \\ I_z\dot{r}=N \end{cases} \tag{11.18}$$

where u and v are the linear velocity components of the craft centre of gravity (C.G.) along the body-fixed system; p and r are the angular velocities about $x-$ and $z-$axes, respectively; X,Y,K,N are the external forces/moments applied to the craft. Each component of the force/moment on the vessel in calm water is expressed by a summation of five independent contributions: the cushion pressure force; inviscid/cross flow drag of side-hulls, wind force and the resulting effect of propulsion and control, (Wade and Wang, 1977; Kaplan, 1995), as shown next.

$$\begin{cases} X = X_{invis} + X_{drag} + X_p + X_w + X_\delta \\ Y = Y_{invis} + Y_{drag} + Y_p + Y_w + Y_\delta \\ K = K_{invis} + K_{drag} + K_p + K_w + K_{buoy} + K_\delta \\ N = N_{invis} + N_{drag} + N_p + N_w + N_\delta \end{cases} \tag{11.19}$$

The inviscid hydrodynamic force and moment are calculated as follows. The total apparent velocity at the cross flow plane of rigid side hull is given by

$$V_r = v + \xi r - f(\xi)p \tag{11.20}$$

where $f(\xi)=z_g-d(\xi)/2$ is the vertical distance of the centre of fluid pressure from the body C.G.; the 2-D added mass is $\mu(\xi)$, and the kinetic energy of a unit slice of the fluid

$$T(\xi,t)=\frac{1}{2}\mu(\xi)V_r^2(\xi) \tag{11.21}$$

Neglecting the second order terms, the hydrodynamic forces and moments acting on a unit axial length at ξ are given by

$$\begin{cases} \dfrac{dY}{d\xi} = -\dfrac{d}{dt}\left(\dfrac{\partial T}{\partial v}\right) \\ \dfrac{dK}{d\xi} = -\dfrac{d}{dt}\left(f\dfrac{\partial T}{\partial v}\right) \\ \dfrac{dN}{d\xi} = -\dfrac{d}{dt}\left(\dfrac{\partial T}{\partial r}\right) - u\left(\dfrac{\partial T}{\partial v}\right) \end{cases} \tag{11.22}$$

In which u is the axial velocity of the body. The kinetic energy T at a fixed cross flow plane is a function of ξ and time, t. The total derivate is

$$\frac{d}{dt}=\frac{\partial}{\partial t}+u\frac{\partial}{\partial \xi} \tag{11.23}$$

Substituting (11.21) into (11.22), the forces and moments acting on the side hulls can be obtained by integration over the side hull length.

The cross-flow drag is:

$$Drag = -\frac{1}{2}\rho c_d s |V_r| V_r \tag{11.24}$$

where c_d = drag coefficient; s =project area. A water jet model is used (Wade and Wang, 1977). Wind force is calculated by formulae given by Aage (1971). Substituting all the external forces and moments into equations of motion of the vessel in calm water, the linear and angular velocities can be obtained by solving the equation with a Runge-Kutta scheme, and the velocity components in the body fixed system are transformed to the earth fixed frame by the following:

$$\begin{cases} \dot{x}_* = u\cos\psi - v\cos\varphi\sin\psi \\ \dot{y}_* = u\sin\psi + v\cos\varphi\cos\psi \\ \dot{\varphi} = p \\ \dot{\psi} = r/\cos\varphi \end{cases} \tag{11.25}$$

The solution of (11.25) gives the trajectory of the craft. In the case of steady turning, the deflecting angle of the nozzle of the water jet is

$$\delta(t) = \begin{cases} 0 & 0 < t < t_1 \\ \dfrac{t - t_1}{t_2 - t_1}\delta_0 & t_1 < t < t_2 \\ \delta_0 & t_2 < t \end{cases} \tag{11.26}$$

An ALV may be sensitive to the directional stability due to its design characterises: relatively shallow draught, the transom stern, the air chambers and high operational speed. The equations for analysis of the directional stability are the same as for turning simulations. An autopilot control law is also incorporated in the form

$$\delta = k_1(\psi - \psi_d) + k_2\dot{\psi} \tag{11.27}$$

where k_1 and k_2 are the coefficients of the control law, and ψ_d is the desired vessel direction. During the simulation, an initial yaw angle of the craft, ψ_0, and the desired orientation, ψ_d, were set up. At a particular initial vessel speed (entrance velocity of the vessel), time histories of the vessel motions can be obtained through the simulations, from which the directional stability performance of the vessel can be assessed.

11.5 Summary

In this Chapter, the mathematical models for analysis of the transverse static stability at zero speed, the longitudinal dynamic stability in calm water and the stability in manoeuvring in calm water of the ASV are presented. The non-linear dynamic stability model in calm water taken into account of air compressibility in the cushion chamber(s) and can be numerically solved by a time stepping approach. These models could form the basis for assessing the stability performance of the ASV. It is expected that those tools could be helpful for designers and operators of the craft.

It should be noticed that no validation has been carried out for the present simulations due to lack of the experimental data. The stability analysis reported here is mainly for the craft at on-cushion mode. The stability and survivability of the ALV craft at off-cushion mode (damage case) should be analysed by using other methods/tools.

Chapter 12 Case Study - Dynamic Analysis of the ASV

In this Chapter, implementation of the mathematical models for the stability analysis described in Chapter 11 has been carried out for an ASV, the ALV, E40. Numerical results are provided and discussed.

12.1 Stability of the ALV, E40

Figure 12.1 shows the transverse static right lever of the ALV, E40 at zero speed. The initial transverse matecentric height is calculated by equation (11.4). It can be seen that the matecentric height of the vessel at on-cushion mode is lower than that of off-cushion mode, which means that the cushion pressure has a negative effect on the static stability of the vessel. However, due to its catamaran type of design, the transverse matecentric height of the vessel remains high.

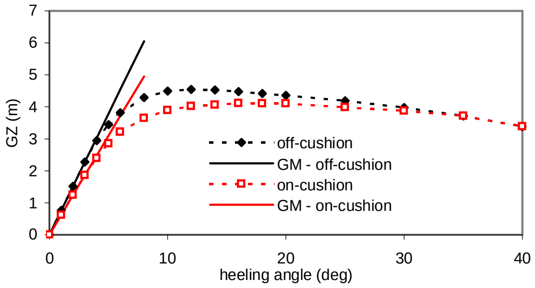

Figure 12.1 Transverse static stability of the ALV E40 at zero speed

The dynamic model derived in Chapter 11 has been used for analysis of the longitudinal stability in calm water. Most of the simulation work is for the numerical calculation of the impulse/transfer response functions of the free surface elevation. The simulation requires transfer function of the free surface elevation covers the whole frequency range and at a relatively high Froude number. The numerical scheme proposed in the present study is able to facilitate these calculations. Previously published works are either for lower frequency range (Doctors, 1977) or for relatively lower speed (Kim and Tsakonas, 1981).

Figures 12.2 ~ 12.4 show samples of the impulse response functions of the free surface elevation on different location at the stern of the ALV, E40. The vessel

Froude number is $Fn = 1.5$. It is observed that the durations of the impulse response functions are relatively short, normally less than 1 second. This means that the memory effect of the cushion pressure on the free surface elevation response lasts a short period of time. This property is particularly useful for calculating the convolution integral for free surface elevation in the time domain in equation (11.12). Figure 12.5 is a sample of the impulse response function for the escape volume for the cushion. The profile of the curve is similar to that of the free surface elevation.

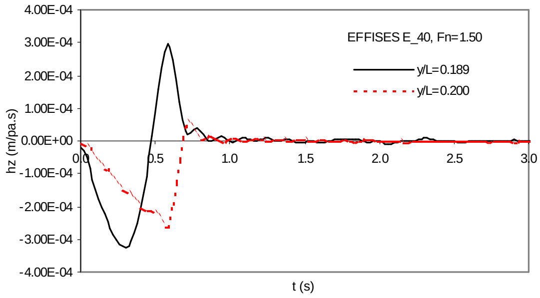

Figure 12.2 Impulse response function of the free surface elevation at stern of the ALV, E40

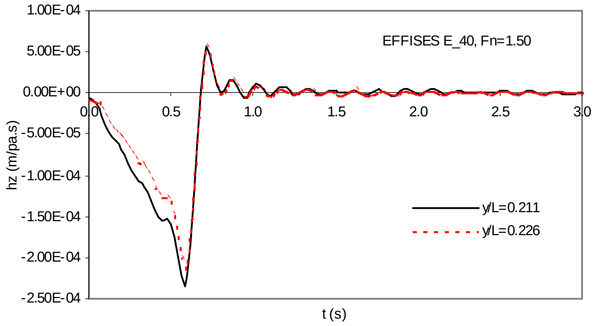

Figure 12.3 Impulse response function of the free surface elevation at stern of the ALV, E40

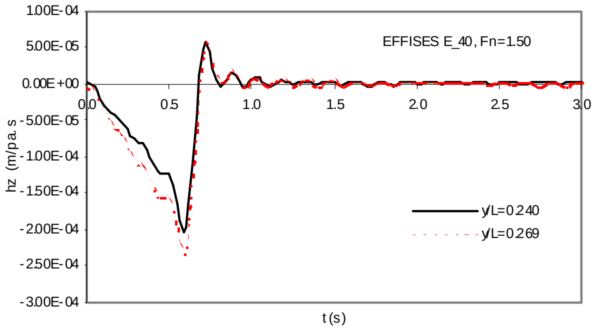

Figure 12.4 Impulse response function of free surface at stern of the ALV, E40

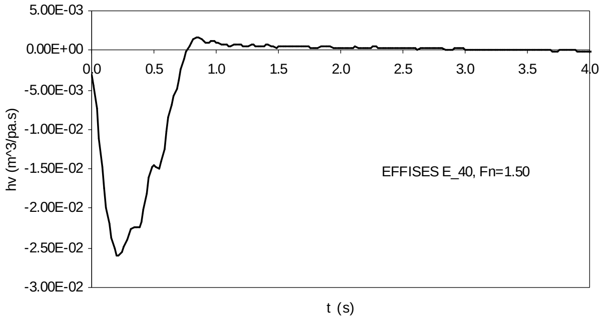

Figure 12.5 Impulse response function of escape volume of the ALV, E40

The longitudinal dynamic stability for heave and pitch motions of the ALV E40, in still water are simulated with the time domain approach. The transient responses will be studied based on the equations of motions of the vessel in (11.14) ~ (11.16). The vessel is undergoing motions subject to an initial condition. This will lead to its equilibrant position in case of a stable condition, see Figure 12.6. However, the vessel motions will not decay in case of unstable conditions, see Figure 12.7.

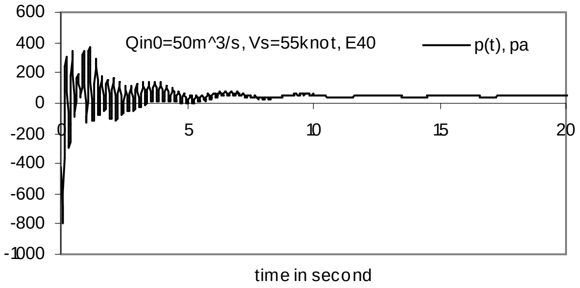

Figure 12.6 Sample of stable solution, cushion pressure, $Q_{in,0}$ is fan inflow rate at the equilibrium condition

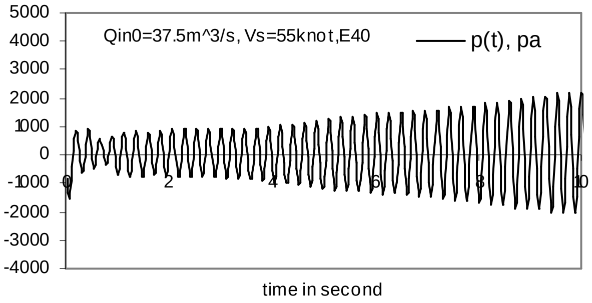

Figure 12.7 Sample of unstable solution, cushion pressure, $Q_{in,0}$ is fan inflow rate at the equilibrium condition

A number of design parameters are chosen for the simulations according to the base design of the ALV E40. These include:

- Cushion height at the equilibrium condition (Z_0);
- Fan inflow rate at the equilibrium condition ($Q_{in,0}$) ;
- Position of centre of gravity of the vessel (x_g, z_g);
- Fan discharge slope characteristics ($\partial Q_{in} / \partial p$);
- Particulars of the stern flap (dimension and orientation).

Figure 12.8 shows some of the simulated results for the ALVs, in which combinations of the craft design parameters are shown for the stable/unstable conditions. In the unstable cases, the simulated cushion pressure is divergent. It is found from the simulated results that: in the case of a craft with this instability, the pressure in the cushions accumulates, the cushion volume and the craft motions increase, the escape of the accumulated air requires a large escape area, the pitch angle increases suddenly, and the cushion pressure collapses like a cavity breaking down. Typically, the craft is stable for the longitudinal position of C.G. within a limited range. A small inflow rate will increase chance of this instability. Also the stern flap angle should be set properly to ensure the craft has a correct trim altitude and restoring moment at speed.

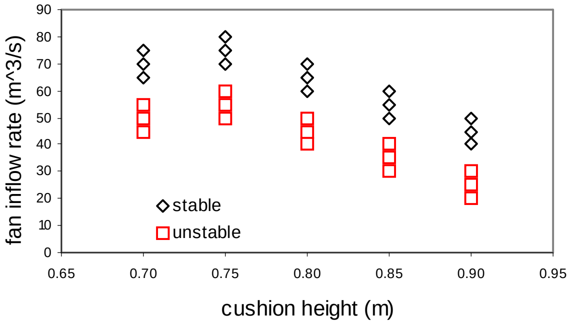

Figure 12.8 Stable/unstable boundary for the longitudinal dynamic stability of the ALV at 55 knots in calm water

12.2 Stability of the ALV in Manoeuvring in Calm Water

The ALV E40 is subjected simulation for its manoeuvring motion in calm water by using the mathematical model derived in Chapter 11. Since details of the water jet parameters for the vessel are not available at the time of the calculation, these parameters are derived from the literatures. The simulation starts with the craft in a straight course with the deflecting angle of the nozzle of the water jet gradually increasing to the desired value, and then kept fixed, thus nozzles of the water jets generating a turning moment.

Figures 12.9 and 12.10 show some of the simulated results of the ALV turning at entering speed of 50 knots. The turning lever can be derived from the simulated time histories and by equation (11.17). The heeling angle is also a part of the output of the simulations. In the HSC Code, it is required that the total heel angle of the craft in the on-cushion mode due to beam wind and due to turning shall be less or equal to 12^0. In the present case, the craft heel angle due to turning is about 1.7^0, which is far less than the limited value. Figure 12.11 shows the heeling angle of the craft in turning at different nozzle deflecting angles. It is found that the heeling angle will increase with increasing deflecting angles. This is not surprising, since a larger nozzle deflecting angle develops larger yaw turning moment and larger turning rate. It is expected that at large deflecting angles, the craft will experience significant heeling and resulting cushion pressure collapse and instability of the craft. Other simulated results (not shown here) indicate that larger nozzle deflecting angle also results higher turning levers that worsen the stability.

The effects of entering speed on turning lever and turning diameter are shown in Figure 12.12. The dependency of turning diameters on nozzle deflecting angle of the water jet is shown in Figures 12.13. It should be mentioned that the present model is based on relatively simple external force models, the hydrodynamic forces are estimates and various parameters are assumed (e.g., water jet). It is expected that further refinement of the model should be made and verified when more accurate forces/parameters are available.

Figures 12.14 and 12.15 are samples of the time history for the directional stability simulation. In this case, the initial yaw angle of the craft is $\psi_0 = 10^0$ and the desired orientation is $\psi_d = 0^0$; initial vessel speed (entrance velocity of the vessel) is 50knots. The control parameters are taken to be $k_1 = 1$ and $k_2 = 2$. The simulated results indicate that the vessel can reach its desired orientation in about 20 seconds. Also in this process, the vessel undergoes roll motion due to the moment generated by the water jet. Numerical tests show that the control parameters k_1 and k_2 have a significant effect on the directional stability of the craft. Again, in order to carry out more realistic simulation for the ALV, actual parameters should be used as the input of the simulator.

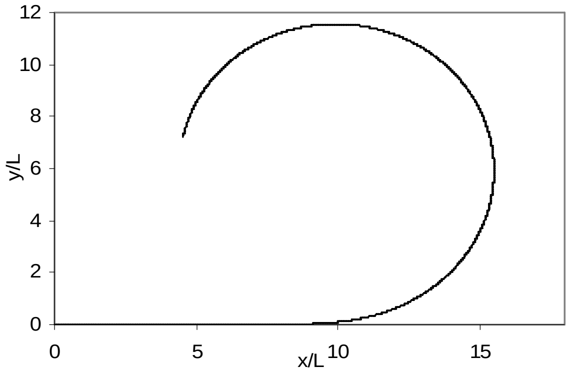

Figure 12.9 Trajectory of the ALV E40 at entering speed of 50 knots

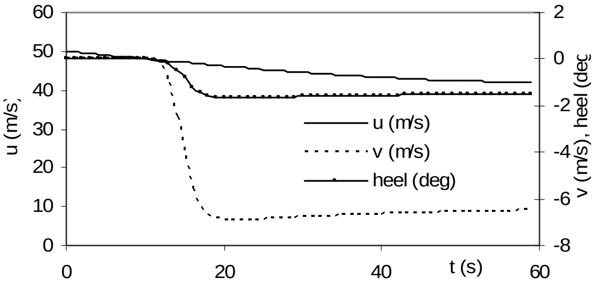

Figure 12.10 Manoeuvring motions of the ALV E40 at entering speed of 50 knots

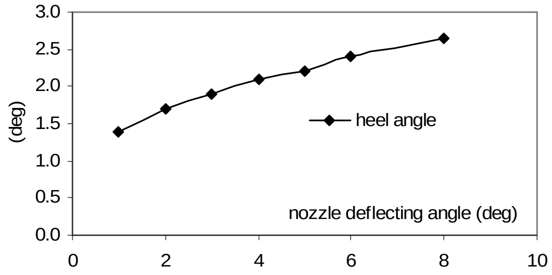

Figure 12.11 Heel angle during turning of the ALV E40 at entering speed of 50knots

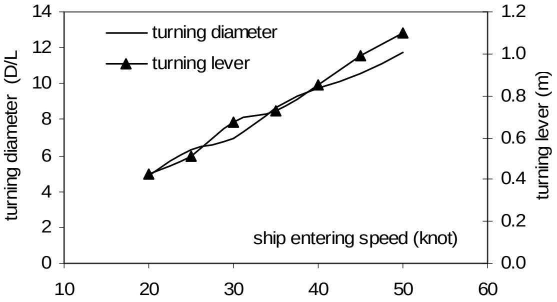

Figure 12.12 Turning diameter of the ALV E40 at nozzle deflecting angle $\delta_0 = 1.6^0$

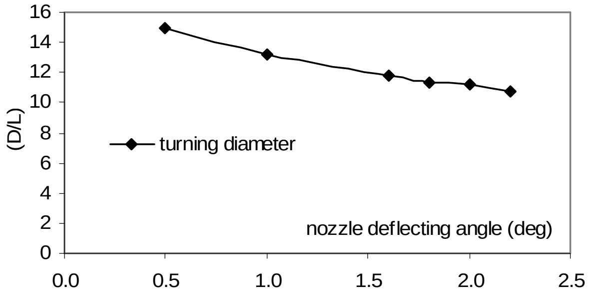

Figure 12.13 Turning diameter of the ALV E40 at entering speed of 50 knots

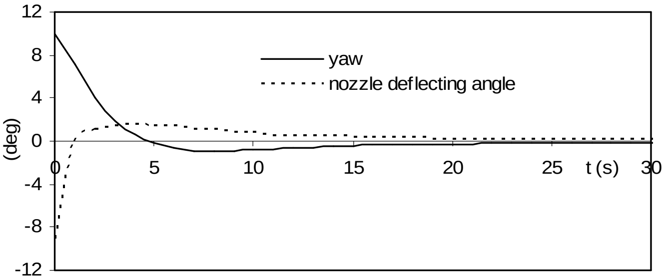

Figure 12.14 Time histories of yaw and nozzle angle for the ALV E40 at entering speed of 50 knots

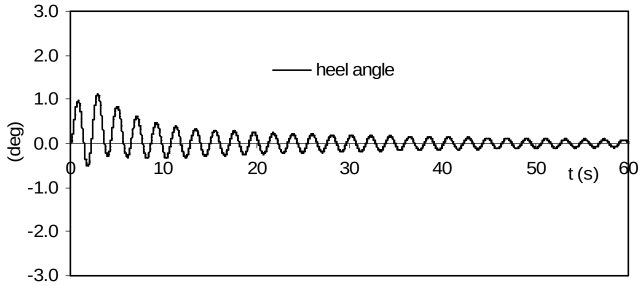

Figure 12.15 Roll time histories for the ALV E40 at entering speed of 50 knots

12.3 Summary

In this Chapter, a case study for the transverse static stability at zero speed, the longitudinal dynamic stability in calm water and the stability for manoeuvring motions in calm water for an ASV, ALV E40, have been carried out. The mathematical models and numerical simulation method are described in Chapter 11. Numerical results for the ALV E40 concept are presented and discussed. The effects of some of the design parameters of the vessel on its stability performance are analysed. The results appear to show applicability and effectiveness of the developed tools at both design and operational stage of these types of high speed crafts.

The stability analysis reported here is mainly for the craft at on-cushion mode. The stability and survivability of the ALV crafts at off-cushion mode (damage case) should be analysed by using other methods/tools. It is realized that some of the coefficients in the numerical simulations are empirical, or borrowed from other SES vessels: this may partially affect the accuracy of the present prediction. It is true that the prediction will be improved when more accurate data made available for the ALVs, and validations by model tests or trials, which are not available at the moment, will help in improving the present numerical models.

Chapter 13 Contributions of the Present Study

13.1 Achievements against the objective

A hydrodynamic analysis for Air Supported Vessel has been carried out in this thesis. The analysis covers performances in the steady forward motion, in the unsteady harmonic motion and the stability. Mathematical models for the steady and the unsteady flows and their numerical calculating methods are presented for this advanced marine vehicle. A number of case studies have been provided to demonstrate the applicability of the approaches presented in the study. The following achievements have been made against the objectives:

1. A numerical method is presented for evaluation of the steady potential flow field and the free surface elevation of a pressure underneath the Air Supported Vessel moving on the free surface. This is applied successfully in the prediction of the wash wave (far-field) and wave-making resistance (near-field) of the vessel. It may be also applied to wave pattern prediction for other high speed craft, such as planing craft, SES, ACV.
2. Numerical methods are proposed for the computation of the potential flow field of the pressure patch for the Air Supported Vessel moving in harmonic motions.
3. A practical mathematical model for the prediction of seakeeping performance in waves for the ASV has been developed. Numerical examples have demonstrated applicability of the model.
4. Non-linear mathematical models have been established for analysis of the longitudinal dynamic stability of the ASV in calm water. A time domain stepping algorithm is developed to solve the problem numerically, and reasonable results have been obtained.

The content covers a wide range of hydrodynamic performances for the ASVs. The case studies carried out in the thesis demonstrated the applicability of those models.

These numerical prediction tools are expected to be helpful at both design and operational stages of this type of vessels.

13.2 Contributions of the Present Study

The contributions of this study are summarised as follows:

1. The numerical method for the steady potential flow of a pressure patch proposed by the present study is efficient and also accurate based on the assumption of the linearization. The numerical instability problem in prediction of the hydrodynamic distribution for the three dimensional planing hulls found in previous studies has been solved. Further discussion about the limitation of the assumption is presented in the next Chapter.
2. A practical and efficient numerical prediction tool for wash wave field of the ASVs has been established.
3. A practical and efficient numerical tool for seakeeping prediction in frequency domain for the ASVs in waves has been established.
4. A numerical prediction tool for the dynamic stability analysis of the ASVs has been established.
5. In terms of publications, five papers have been published in peer reviewed international journals based on the works carried out in the present study.

Chapter 14 Recommendations for the Future Work

As for any numerical approach, a number of assumptions and simplifications were necessary for the present study. This is due to the very complicated flow around the ASV. The fact that there is little experience about the hydrodynamic performances for this type of vessel in numerical calculation, model testing and full scale trials ensures that a single PhD thesis is unable to cover all these topics thoroughly, and further research on the subject is needed. The present study deals with various aspects of the hydrodynamic performances of the ASV: the steady potential flow (wash wave and wave-making resistance), seakeeping and the stability. The importance of these hydrodynamic performances will depend on the ship owner, the designer and the associated policies and regulations for the vessel operations. In no particular order of priority, the following topics are suggested:

1 In calculations of the wash wave and wave-making resistance of the ASV, effect of the rigid hull of the vessel is not taken into account. This may be reasonable for a high-speed ASV, however, for a general ASV design, a source distribution panel method may be used to calculate this part of contribution.

2 In the seakeeping prediction model, the hydrodynamic forces/moments of the rigid hull are calculated by a strip theory. The strip theory is applicable for ships at a lower Froude numbers and slender body. Although contribution of hydrodynamic forces/moments from the side-hulls is believed to be small in the case of an ALV, a more rational 3D method will certainly improve accuracy of the prediction for a general ASV design. A time domain non-linear approach to solve the unsteady free surface flow field will also improve the present frequency domain approach.

3 The hydrodynamic coefficients of the side-hulls used in the manoeuvring and the stability simulations are estimated by some approximation methods. Ideally, these derivatives should be measured from model testing. That will improve the prediction further.

4 More validations (tank model testing or full scale trails) are needed. This will improve the accuracy of the prediction and refine the mathematical models.

5 Methods for estimation of total resistance and powering of the ASVs are needed;

6 In the longer term, as the computer technology and numerical technique developing, a full 3D volume method (including viscous effect) to resolve the detailed flow around an ASV sailing in the real seaways should be carried out. This will remain as a challenge for hydrodynamic community in the future.

7 Methods for hull form optimisation considering the hydrodynamic performances for the ASVs also need to be developed.

References

Abramowitz, M., Stegun, I. A., 1970, Handbook of mathematical functions, Dover Publications, Inc., New York.

Aelbrecht, D., Dern, J. C., Doutreleau, Y., 2000, A design tool for high speed ferries washes, Proceedings of 23rd Symposium on Naval Hydrodynamics.

Aage, C., 1971, Wind coefficients for nine ship models, Hydro-or Aerodynamisk Laboratorium, Report No. A-3.

Allenstrom, B., Liljenberg, H., Tudem, U., 2001, An Air Lifted Catamaran – hydrodynamical aspects, Proceedings of FAST'2001, Southampton, U.K.

Allenstrom, B., Liljenberg, H., Tudem, U., 2003, Concept development and model testing – new generation air assisted vessels (AAV) with water jet propulsion, Proceedings of FAST'2003, Ischia, Italy.

Andersen, M. L., Clason, P., Ottosson, P., Andreasson, H., Svensson, U., 2000, Wash waves – problems and solutions, *SNAME Transactions*, Vol. 108.

Beck, R., 2001, Modern seakeeping computations for ships, Proceedings of 23rd Symposium on Naval Ship Hydrodynamics.

Bertram, V., 1999, Rankine panel methods for seakeeping problems, 31st WEGEMT school, Hamburg.

Bhushan, S., Xing, T., Carrica, P., Stern, F., 2009, Model- and full scale URANS simulations of Athena resistance, powering, seakeeping, and 5415 manoeuvring, Journal of Ship Research, 53(4).

Blount, D. L., Codega, L. T., 1992, Dynamic stability of planing boats, Marine Technology, 29(1).

Blyth, A.G., 1993, The roll stability of Surface Effect Ships, Transactions of The Royal Institution of Naval Architects, London.

Barratt, M.J., 1965, The wave drag of a hovercraft, Journal of Fluid Mechanics, 22, 39-47.

Brizzolara, S., Federici, A., 2010, CFD modelling of planing hulls with partially ventilated bottom", William Froude conference: advances in theoretical and applied hydrodynamics – past and future, RINA, Portsmouth, U.K.

Butler, E. A., 1985, The Surface Effect Ship, Naval Engineers Journal.

Chen, H.H., 1977, On a rectangular pressure distribution of oscillating strength moving over a free surface", Journal of Ship Research, 21 (1).

Chen, X. B., Diebold, L., 1999, Analytic expressions of unsteady ship wave pattern, 14th IWWWFB.

Chen, X. B., Wu, G. X., 2001, On singular and highly oscillatory properties of the Green function for ship motions, Journal of Fluid Mechanics, Vol. 45.

Cheng, H. X., Ni, Q. J., Xing, S. D., He, S. L., 2011, An experimental study on artifical bubble ship hydrodynamic characteristics, Journal of Ship Mechanics, 15 (11).

Cheng, X. M., Wellicome, J. F., 1994, Study of planing hydrodynamics using strips of transversely variable pressure. Journal of Ship Research, 38 (1).

Cheng, X. M., Wellicome, J. F., 1999, Numerical prediction of forces on planing flat catamaran hulls and prismatic hulls, International Shipbuilding Progress, 46 (488).

Choi, J. K., Hsiao, C. T., Chahine, G. L., 2005, Design trade-off analysis for high performance ship hull with air plenums, Proceedings of 2nd Symposium on seawater drag reduction, Busan, Korea, 23-26 May 2005.

Clement, E. P., Blount, D. L., 1963, Resistance tests of a systematic series of planing hull forms, Transactions of Naval Architects and Marine Engineers, 71, 491 – 579.

Cohen, S., Blount, D., 1986, Research plan for the investigation of dynamic instability of small high-speed craft, *Trans. SNAME*, **94**.

Cummins, W. E., 1962, The impulse response function and ship motions, *Schiffstechnik*, **9** (47).

Day, A. H., Doctors, L. J., 2001, Wave-wake criteria and low-wash hull form design, Transactions of the Royal Institute of Naval Architects.

Doctors, L. J., 1972, The forces on an air-cushion vehicle executing an unsteady motion, Proceedings of 9th Symposium on Naval Hydrodynamics, Paris, France, 35-97.

Doctors, L. J., 1974, The hydrodynamic influence on the non-linear motion of an ACV over waves, Proceedings of 10th Symposium on Naval Hydrodynamics, Cambridge, MA, 389-420.

Doctors, L. J., 1975, Representation of three dimensional planing surface by finite elements, Proceedings of the First Conference on Numerical Ship Hydrodynamics.

Doctors, L. J., 1977, The effect of air compressibility on the non-linear motion of an air-cushion vehicle over waves, Proceedings of 11th Symposium on Naval Hydrodynamics, London.

Doctors, L. J., 1985, Hydrodynamics of high-speed small craft, Department of Naval Architecture and Marine Engineering, The University of Michigan, Ann Arbor, MI, Report No. 292.

Doctors, L.J., McKensson, C. B., 2006, The resistance components of a surface-effect ship, Proceedings of Twenty-sixth Symposium on Naval Hydrodynamics, Roma, Italy.

Doctors, L.J., Sharma, S. D., 1970, The wave resistance of an air-cushion vehicle in accelerated motion", University of Michigan.

Dong, W. C., Ou, Y. P., 2011, Experimental study on resistance and longitudinal motion of high-speed air cavity craft in regular waves, Journal of Ship Mechanics, 15 (9).

EFFISES Project, 2001-2004, Energy Efficient Safe Innovative Ships & Vehicle, European Commission CEC Contract no. GRD1-2000-25847, coordinated by SES Europe.

Faltinsen, O. M., 2005, Hydrodynamics of high-speed marine vehicles, Cambridge University Press, Cambridge.

Fukuda, K., Tokunaga, J., Nobunaga, T., Nakatani, T., Iwasaki, T., Kunitake, Y., 2000, Frictional drag reduction with air lubricant over a super-water-repellent surface, Journal of Marine Science and Technology, 5.

Ghassemi, H., Ghiasi, M., 2008, A combined method for the hydrodynamic characteristics of planing craft, Ocean Engineering, 35(3-4).

Gokcay, S., Insel, M., Odabasi, A. Y., 2004, Revisiting artificial air cavity concept for high speed craft, Ocean Engineering, 31.

Gonzalez, M. J., 2002, State of the art report in design techniques and tools oriented to virtual testing, EFFISES project report.

Graham, T. A., Sullivan, P. A., 2002, Pitch-heave dynamics of a segmented skirt air cushion, Journal of Ship Research, 46(2).

Harley, H. D., 1996, Surface effect vessel hull, US Patent 5570650.

Hartman Associates, Inc., 1990, Impacts of the passenger-only fast-ferry wake – rich passage to Bremerton, Report prepared for Washington State Ferry in association with Science Applications International Corporation, Merit Systems, Inc., Parametrix, Inc., and Dalton, Olmsted, and Fuglevand, Inc.

Huang, T. T., Wong, K. K., 1970, Disturbance induced by a pressure moving over a free surface", Journal of Ship research, 14(3).

IMO, 2000, HSC Code 2000, Annex 7, Stability of multihull craft, Halstan & Co. Ltd, Amersham, U.K.

Janson, C. E., Andersen, M. L., Larsson, L., 2003, Calculation of deep-water wash waves using combined Rankine/Kelvin source method, Journal of Ship Research, 47(4).

Jasionowski, A, 2001, PROTEUS3 users manual, University of Strathclyde, Glasgow.

Kaplan, P., 1995, Manoeuvring and stability of SES and catamaran ships, Transactions of The Royal Institution Naval Architects.

Kaplan, P., Bentson, J. and Davis, S., 1981, Dynamics and hydrodynamics of surface effect ships, Trans. SNAME, **89**, 211-247.

Kapryan, W. J., Boyd, G. M., 1955, Hydrodynamic pressure distributions obtained during a planing inverstigation of five related prismatic surface, NACA technical note, No. 3477.

Katayama, T., Hayashita, K., Suzuki, K., Ikeda, Y., 2002, Development of resistance test for high-speed planing craft using very small model-scale effects on drag force, Proceedings of Asia Pacific Workshop on Hydrodynamics, 7-14.

Kim, C. H., Tsakonas. S., 1981, An analysis of heave added mass and damping of a surface effect ship, Journal of Ship Research, 25(1).

Kohansal, A. R., Ghassemi, H., 2010, A numerical modelling of hydrodynamic characteristics on various planing hull forms, Ocean Engineering, 37(5-6).

Lai, C., Troesch, A. W., 1996, A vortex lattice method for high speed planing, International Journal for Numerical Methods in Engineering, 22, 495 -513.

Larsson, L, Stern, F, Visonneau, M,: CFD in ship hydrodynamics – results of the Gothenburg 2010 workshop. Proceedings, MARINE 2011, Computational methods in marine engineering IV, ISBN/ISSN: 978-84-89925-31-1.

Latorre, R., 1982, Study of the flow surrounding a prismatic planing model, International Shipbuilding Progress, 29(11).

Lavis, D. R., 1979, The development of stability standards for dynamically supported craft, a progress report, High Speed Craft Conference.

Lunde, J. K., 1951, On the linearized theory of wave resistance for a pressure distribution moving at constant speed of advance on the surface of deep or shallow water, Skipsmodelltanken, Norges Tekniske Hogskole, Trondheim, No. 8.

Macfarlane, G. J., Renilson, M. R., 2000, When is low wash? – an investigation using a wave wake database", Proceedings of International Conference on Hydrodynamics of High Speed Craft Wake Wash & Motions Control, London.

Magnuson, A. H., Wolff, K. K., 1975, Seakeeping characteristics of the XR-5, a high length/beam ratio manned surface effect testcraft: 1. XR-5 model response in regular head waves, David Taylor Naval Ship Research and Development Center, SPD-616-01, Bethesda, MD, USA.

Maruo, H., 1951, Two dimensional theory of the hydroplane. Proceedings of the First Japan National Congress for Applied Mechanics.

Maruo, H., 1967, High and low aspect ratio approximation of planing surface, Schiffstechnik, 72.

Masson, E., DeBayser, O., Martin, D., 1991, Evaluation de la resistance de vagues d'un sous-marin en immersion totale, Proceedings, 3emes Journees de l'Hydrodynamique Grenoble, France.

Matsumura, K., Kataui, T., 1999, Variational principle for determining the unknown wetted surface of a planing ship, Journal of Marine Science and Technology, 4, 180 – 186.

Matveev, K. I., 2003, Air-cavity ships are ready for a wider market, Speed at Sea.

Matveev, K. I., 2007, Three dimensional wave patterns in long air cavities on a horizontal plane, Ocean Engineering, 34.

Matveev, K. I., Burnett, T. J., Ockfen, A. E., 2009, Study of air-ventilated cavity under hull on water surface, Ocean Engineering, 36.

Matveev, K. I., Ockfen, A. E., 2009, Modeling of hard-chine hulls in transitional and early planing regimes by hydrodynamic point sources, International Shipbuilding Progress, 56(1).

Milewski, B., Connell, B., Wilson, J., Kring, D., 2007, Dynamics of air cushion vehicles operating in a seaway, Proceedings of 9th International Conference on Numerical Ship Hydrodynamics, Michigan.

Muller-Graf, B., 1997, Dynamic stability of high speed small craft, 25th WEGEMT School, Athens, Greece.

Nakos, D., Nestegard, A., Ulstein, T., Sclavounos, P., D., 1992, Seakeeping analysis of Surface Effect Ships, Proceedings of FAST'91 Conference, Trondheim, Norway.

Newman, J. N., 1978, Marine hydrodynamics, MIT press, Cambridge, MA.

Newman, J. N., 1987, Evaluation of the wave resistance Green function: part 1 – the double integral, Journal of Ship Research, 31, 79 – 90.

Newman, J. N., Poole, F. A. P., 1962, The wave resistance of a moving pressure distribution in a canal, Schiffstechnik, 9, 21-26.

Nickolson, K., 1974, Some parametric model experiments to inverstigate broaching-to, International Symposium on Dynamics of Marine Vehicles and Structures in Waves, ed. R. E. D. Bishop, W. G. Price, London, Mechanical Engineering Publications Ltd.

Noblesse, F., 1978, On the fundamental function in the theory of steady motion of ships, Journal of Ship Research, 22, 212-215.

Noblesse, F., 1981, Alternative integral representations for the Green function of the theory of ship wave resistance, Journal of Engineering Mathematics, 15, 241-265.

Noblesse, F., Delhommeau, G., Yang, C., 2009, Practical evaluation of steady flow resulting from a free-surface pressure patch. Journal of Ship Research, 53(3).

NS – ISO 2631-31, November 1985.

Ogilvie, T. F., 1964, Recent progress towards the understanding and prediction of ship motions, Proceedings of 5th Symposium on Naval Hydrodynamics, Washington, D.C..

Okita, N., Sahin, I., Hyman, M. C., 2001, Disturbance during steady and unsteady motions of a two-dimensional pressure distribution, Journal of Ship Research, 45(3).

Papanikolaou, A. D., 2002, Developments and potential of advanced marine vehicles concepts, Bulletin of the Kansai Society of Naval Architects, 55.

Papanikolaou, A. D., 2010, Holistic ship design optimization, Computer-Aided Design, 42, 1028-1044.

Papanikolaou, A. D., Georgantzi, N., Karayannis, T., 2002, Adaptation of stability rules and tools to SES, Project EFFISES, Report of National Technical University of Athens.

Pedersen, R., Werenskiold, P., 1997, Dynamic roll instability for high speed mono hull craft, Proceedings of the International Conference SURV IV, Surveillance, Pilot & Rescue Craft for 21st Century, Gothenburg, Sweden.

Ponizy, B., Noblesse, F., Ba, M., Guilbaud, M., 1994, Numerical evaluation of free-surface Green function, Journal of Ship Research, 38, 193-202.

Raven, H. C., 1996, A solution method for the nonlinear ship wave resistance problem, Ph. D. thesis, Delft University of Technology, Netherland.

Salvesen, N., Tuck, E. O., Faltinsen, O. M., 1970, Ship motions and sea loads, Trans. SNAME, 78.

Savitsky, D., 1964, Hydrodynamic design of planing hulls, Marine Technology, 1(1).

Scullen, D. C., Tuck, E. O.: 2011, Free surface elevation due to moving pressure distribution in three dimensions, Journal of Engineering Mathematics, 70, 29-42.

Sclavounos, P., Nakos, D., Huang, Y., 1993, Seakeeping and wave induced loads on ships with flare by a Rankine panel method, 6th International Conference on Numerical Ship Hydrodynamics, Iowa City.

Sclavounos, P., Purvin, S., Ulusoy, T., Kim, S., 2003, Simulation based resistance and seakeeping performance of high speed monohull vessels equipped with motion control lifting appendages, Proceedings of FAST'03, Ischia,Italy.

Shen, Y.T., Ogilvie, T. F., 1972, Non-linear hydrodynamic theory for finite span planing surfaces", Journal of Ship Research, 16(1).

Scottorf, W. F., 1932, Experiments with planing surface, NACA TM No.661.

Scullen, D. C., Tuck, E. O., 2011, Free-surface elevation due to moving pressure distributions in three dimensions, Journal of Engineering Mathematics, 70, 29-42.

Shen. Y. T., Ogilvie, T. F., 1972, Non-linear hydrodynamic theory for finite span planing surfaces, Journal of Ship Research, 16(1).

Shoemaker, J. M., 1934, Tank tests of flat and vee-bottom planing surface, NACA TN, No. 509.

Sorenson, A. J., Egeland, O., 1995, Design of ride control system for surface effect ships using dissipative control, Automatics, 31(2), 183-199.

Subramanian, V. A., Subramanyam, P. V., Ali, N. S., 2007, Pressure and drag influence due to tunnels in high-speed planing craft, International Shipbuilding Progress, 54(1).

Savander, B. R., Scorpio, S. M., Taylor, R. K., 2002, Steady hydrodynamic of planing surface, Journal of Ship Research, 46(4), 248 – 279.

Tatinclaux, J. C., 1975, On the wave resistance of Surface Effect Ships, Transactions of SNAME.

Taravella, B. M., Vorus, W. S., 2011, A General solution to low-aspect-ratio flat-ship theory, Journal of Engineering Mathematics, 71, 171 - 184.

Telste, J. G., Noblesse, F., 1989, The nonoscillatory near-field term in the Green function for steady flow about a ship, Proceedings of 17th Symposium on Naval Hydrodynamics, The Hague, 39-52.

Tong, J., 1989, A finite element approach to planing problem, Ph. D. Thesis, University of Southampton.

Thill, C., Toxopeus, S., Walree, F., 2005, Project energy-saving air-lubricated ships (PELS), Proceedings of 2nd International Symposium on Seawater Drag Reduction, Busan, Korea.

Tuck, E.O., 1975, Low aspect ratio flat ship theory. Journal of Hydronautics, 9(1).

Tuck, E. O., Scullen, D. C., Lazauskas, L., 2002, Wave patterns and minimum wave resistance for high speed vessels, Proceedings of 24th Symposium on Naval Hydrodynamics, Japan.

Tudem, U. S., 2002, The challenge of introducing innovative air lifted vessels to the commercial market, Proceedings of the 18th Fast Ferry Conference, Nice, France.

Ulstein, T., 1995, Nonlinear effects of a flexible stern seal bag by cobblestone oscillations of an SES, Dr. ing. thesis, Dept. of Marine Hydrodynamics, NTNU, Trondheim.

Vassalos, D., 1995, Intact and damage stability and survivability of AMVs", WEGEMT Short course on Design of Advanced Fast Marine Vehicles, University of Glasgow.

Vassalos, D., Hamamoto, M., Papanikolaou, D, Molyneux, D., 2000, Contemporary ideas on ship stability, Oxford, Elsevier Science Ltd.

Vassalos, D., Konovessis, D., 2008, The thematic network SAFER EURORO: an integrated approach to safe European roro ferry design, Marine Technology, Vol. 45, No.1.

Vassalos, D., Xie, N., Jansionoski, A., Konovessis, D., 2008, Stability and safety analysis of the air lifted catamaran, Jpurnal of Ships and Offshore Structures, 3(2).

Wahab, R., Swaan, W. A., 1964, Course keeping and broaching in following waves, Journal of Ship Research, **7** (4).

Wang, D. P., Rispin, P., 1971, Three dimensional planing at high Froude number, Journal of Ship Research, 15(3).

Wade, R. B. and Wang, S., 1977, Some aspects of side-hull hydrodynamics and manoeuvring in the design of Surface Effect Ships", Proceedings of 11th Symposium on Naval Hydrodynamics, London.

Wang, X. L., Day, A. H., 2007, Numerical instability in linearized planing problems, International Journal for Numerical Methods in Engineering, 70.

Wehausen, J. V., Laitone, E. V., 1960, Surface waves, Handbuck Der Physik, Band IX, Hydrodynamics III, 592-603.

Wellicome, J. F., Jahangeer, Y. M., 1978, The prediction of pressure loads on planing hulls in calm water. Royal Institution of Naval Architects.

Xie, N., Jasionowski, A., Vassalos, D., 2004, A numerical method for predicting wash waves of SES", Journal of Ship Mechanics, 8(6).

Xie, N., Jasionowski, A., Vassalos, D., 2004, Evaluation of wash waves of the Air Lifted Catamaran, Proceedings of the 9th International Conference on Practical Design of Ships and Offshore Floating Structures, Germany, 2.

Xie, N., Paton, I., Vassalos, D., 2011, A study of hull form improvement for a fishing trawler, Proceedings of International Conference on Technologies, Operations, Logistics and Modelling for Low Carbon Shipping, Glasgow, U.K.

Xie, N., Vassalos, D., 2007, Performance analysis of 3D hydrofoil under free surface, Ocean Engineering, 34(8-9).

Xie, N., Vassalos, D., 2012, A three-dimensional numerical study for ship motion in waves with forward speed, to appear.

Xie, N., Vassalos, D., Jasionowski, A., 2005, A study of hydrodynamics of three-dimensional planing surface, Ocean Engineering, 32(13).

Xie, N., Vassalos, D. and Jasionowski, A., Sayer, P., 2008, A seakeeping analysis method for the Air Lifted Vessel", Ocean Engineering, 35(14-15).

Xie, N., Vassalos, D., Lee, B. S., 2007, Numerical prediction of roll hydrodynamics of cylinders fitted with bilge keels with RANSE, Journal of Ship Mechanics, 11(6).

Xie, N., Vassalos, D., Sayer, P., 2007, The effect of lift on the wave-making resistance of multi-hull craft, International Shipbuilding Progress, 54(2-3).

Xie, N., Vassalos, D., 2011, A study of hydrodynamics of planing flat catamaran and prismatic hulls, International Shipbuilding Progress, 58(2-3).

Yun, L., Bliault, A., 2005, Theory and design of air cushion craft, Elsevier Butterworth-Heinemann.

Zaraphonitis, G., Papanikolaou, A., Mourkoyannis, D., 2002, Hull-form optimization of high speed vessels with respect to wash and powering, Project FLOWMART, Report of National Technical University of Athens, School of Naval Architecture and Marine Engineering, Ship Design Laboratory. Also, Proceedings of IMDC'2003, Athens, Greece.

Zhao, L. E., Xie, Y. H., 2009, The Principle and design of high performance ships, National Defense Industry Press, China.

Zhao, R., Faltinsen, O. M., Haslum, H. A., 1997, A simplified nonlinear analysis of a high-speed planing craft in calm water, Proceedings of 4th International Conference on Fast Sea Transportation, Sydney, 431 – 438.

Zilman, G., 2006, Forces exerted on a hovercraft by a moving pressure distribution: robustness of mathematical models, Journal of Ship Research, 50(1).

Appendix A Coefficients for the Cushion Pressure Equation

The equation for the cushion pressure in Chapter 9 is

$$b_{pp}\dot{P} + c_{pp}P + b_{p3}\dot{q}_3 + c_{p3}q_3 + b_{p5}\dot{q}_5 + c_{p5}q_5 + b_{p4}\dot{q}_4 + c_{p4}q_4 = F_{wp} \tag{9.56}$$

where

$$b_{pp} = \frac{V_0\rho_0}{\gamma(P_0 + p_a)} - \rho_0 v_p \tag{A-1}$$

$$c_{pp} = -n_f\rho_a\left|\frac{\partial Q_{in}}{\partial p}\right|_0 - \rho_a c_n \alpha_p\sqrt{\frac{2P_0}{\rho_a}} + \rho_a c_n\frac{A_{L0}}{\sqrt{2P_0\rho_a}} \tag{A-2}$$

$$b_{p3} = \rho_0 S_{00} \tag{A-3}$$

$$c_{p3} = c_n\rho_a B_T\sqrt{\frac{2P_0}{\rho_a}} \tag{A-4}$$

$$b_{p5} = -\rho_0 S_{10} \tag{A-5}$$

$$c_{p5} = -c_n\rho_a x_T B_T\sqrt{\frac{2P_0}{\rho_a}} \tag{A-6}$$

$$b_{p4} = \rho_0 S_{01} \tag{A-7}$$

$$c_{p4} = c_n\rho_a y_c B_T\sqrt{\frac{2P_0}{\rho_a}} \tag{A-8}$$

$$F_{wp} = \rho_0\dot{v}_w + c_n\rho_a\alpha_w\sqrt{\frac{2P_0}{\rho_a}} \tag{A-9}$$

In the above, ρ_0 is the cushion air density at the equilibrium condition, V_0 is cushion chamber volume at the equilibrium condition.

Appendix B Matecentric height of the ALV

Two coordinate systems are selected: the body fixed right-handed system $o-x'y'z'$ with the origin located on the intersection of the free surface $z'=0$ and central plane of the vessel. Its vertical axes oz' is positive upward and through centre of gravity of the vessel. The origin of the second system $o-xyz$ is the same as that of system $o-x'y'z'$. When the vessel has no motion, the two systems overlap, see Figure B-1.

The analysis is for a special case of ALV with side hulls of approximately constant section and wall-sided body surface at the free surface. The stern flaps are vertically placed at the stern of each demi-hull. The initial matecentric height will be derived for the case of the vessel at zero speed and with zero degree of trim angle.

The initial excess pressure in both port and starboard cushion chambers is P_0, which is equal to water head difference between the free surfaces outside and inside the cushion:

$$P_0 = \rho g h_0 \tag{B-1}$$

where h_0 is the water surface depression inside the cushion chambers. The vessel is heeling with a small roll angle, φ. Draft at the port and starboard of the craft will change, while the excess cushion pressure in both chambers is assumed to be unchanged. Due to the pressure balance between inside and outside of the cushion chamber, the water level depression at the centre of the cushion chambers will be

$$\begin{cases} h_1 = h_0 - S_p\varphi/2 \\ h_2 = h_0 + S_p\varphi/2 \end{cases} \tag{B-2}$$

respectively, where S_p is the lateral distance between the cushion central planes of the demi-hulls, see Figure B-1.

The roll moments about origin due to excess cushion pressure on the four vertical walls:

$$\begin{cases} F_{41} = 2(\varphi \times B_c / 2) l_c P_0 h_1 \\ F_{42} = 2(\varphi \times B_c / 2) l_c P_0 h_2 \end{cases} \tag{B-3}$$

where l_c and B_c are the cushion length and width, respectively. Substituting (B-2) into (B-3), the moment due to the horizontal pressure force:

$$F_{41} + F_{42} = 2 A_c P_0 h_0 \varphi \tag{B-4}$$

where $A_c = l_c B_c$ is cushion area of a demi-hull. The restoring moment from the hydrostatic pressure is calculated as follows. Firstly it is assumed the water level is the same inside and outside the cushion. This is a similar expression for that of a conventional catamaran.

$$F_{43} = -\rho g \varphi \iint_{S_c} y^2 dxdy - \rho g \varphi \forall z_B \tag{B-5}$$

where $\forall$ is displacement volume of the rigid side hulls of the ALV. A correction should be made because the water level is lower inside the cushion. We can write this correction term for roll moments as

$$F_{4HC} = -\rho g \iint_{\Sigma} z n'_4 \, ds = -\rho g \iint_{\Sigma} z \left(y' n'_3 - z' n'_2 \right) ds \tag{B-6}$$

where Σ is the hull surface that we have wrongly included by assuming the water level is the same inside and outside of the ALV. Further $\vec{n}' = (n'_1, n'_2, n'_3)$ is the hull surface normal component in the body fixed coordinate system. Positive normal direction is outwards from the hull. In the case of wall-sided body surface at the free surface, then $n'_3 = 0$ and $n'_2 = \mp 1$ for all side walls, respectively.

$$z = z' + y' \varphi \tag{B-7}$$

Substituting (B-7) into (B-6),

$$F_{4HC} = \rho g \left(\iint_{\Sigma_1} + \iint_{\Sigma_2} + \iint_{\Sigma_3} + \iint_{\Sigma_4} \right) (z' + y' \varphi) y' n'_2 ds \tag{B-8}$$

where $\Sigma_i, i = 1, 2, 3, 4$ are the four side-walls for the demi-hull. On these side walls,

$$y' = \pm 0.5 S_p \pm 0.5 B_c \tag{B-9}$$

therefore,

$$F_{4HC} = A_c P_0 h_0 \varphi \tag{B-10}$$

Now the total roll moment acting on the vessel due to roll angle, φ, is

$$F_4 = -\left[-A_c P_0 h_0 - mgz_g + \rho g \iint_{S_c} y^2 ds + \rho g z_B \forall \right] \varphi \tag{B-11}$$

where z_B is the vertical coordinate of the centre of buoyancy at the body fixed coordinate system, $\forall$ is the volume of the under water hull part of the ALV.

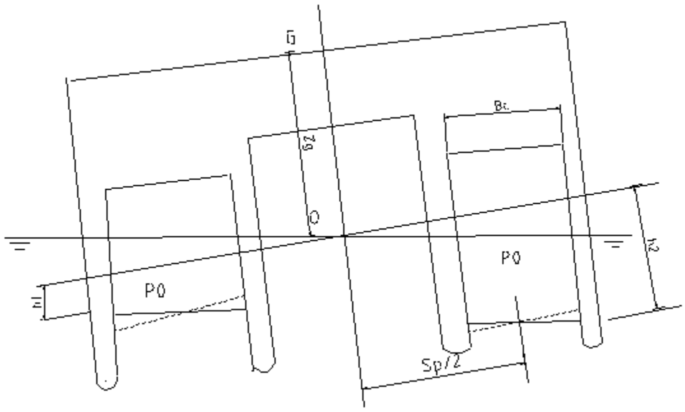

Figure B-1 Calculation of metacentric height of the ALV

The matecentric height of the ALV is

$$\overline{GM} = \frac{1}{mg}\left[-A_c P_0 h_0 - mgz_g) + \rho g S_{yy} + \rho g z_B \forall \right] \tag{B-12}$$

where m is mass of the craft and S_{yy} is the transverse moment of inertia of the water plane area of the ALV at on-cushion condition . The last two terms in the right hand side of (B-12) is the matecentric height of the normal catamaran. It can be seen that the excess pressure P_0 in the cushion gives a negative contribution to the matecentric height of the ALV. For normal (mono-hull) SES, the matecentric height is, see for example Faltinsen [5], Blyth [6]:

$$\overline{GM} = \frac{1}{mg}\left[-2A_c P_0 (0.5h_0 + z_g) + \rho g S_{yy} + \rho g \forall z_B \right] \tag{B-13}$$

which means that the present ALV design has higher matecentric height than the conventional SES, and is safer than the normal SES in the on-cushion mode in this respect.

For the present ALV configurations, the hull form is much more complicate than the above assumed. Therefore, the application of (B-12) to the ALV is limited. The matecentric height of the ALV can be calculated by using a general hydrostatic calculation method, such as the module in PROTEUS (Jasionoski, 2001). The procedures are as follows.

For a given heeling angle of the craft, the water line levels inside and outside cushion can be determined. This is done by an iterative approach. The criterion is that the excess pressure of each cushion chamber should be equal to the local hydrostatic pressure. Weight of the craft should be balanced by buoyancy and force of excess cushion pressure. If one side hull is exposed into the air, then the cushion pressure is equal to the atmosphere pressure, i.e., the excess pressure in that cushion chamber is zero. For each heeling angle, the cushion area will normally change. Once the balanced condition has been found, the restoring moments of cushion pressure and hydrostatic force can be calculated accordingly.

Appendix C Solution of a Pulsating and Moving Pressure Patch

The pulsating pressure distribution of a rectangular shape moving on the calm water surface at speed U, which is a simple harmonic in time, is expressed as

$$p(x,y,0;t)=\begin{cases}\Pi(x,y)e^{i\sigma t} & |x|\le a,|y|\le b\\ 0 & |x|>a,|y|>b\end{cases},t>0 \tag{C-1}$$

The deformation of water due to the foregoing pressure distribution is assumed to be small and is represented by the velocity potential $\varphi(x,y,z;t)$ which is harmonic in space below the free surface; satisfying the differential equation

$$\varphi_{xx}+\varphi_{yy}+\varphi_{zz}=0, \qquad z<0,t>0 \tag{C-2}$$

On the free surface the velocity potential φ and the surface elevation $\varsigma=\varsigma(x,y;t)$ satisfy the linearized kinematical and dynamic boundary condition:

$$-\varsigma_t+U\varsigma_x+\varphi_z=0, \qquad z=0,t>0 \tag{C-3}$$

and

$$\frac{p}{\rho}+g\varsigma+\varphi_t-U\varphi_z=0, \qquad z=0,t>0 \tag{C-4}$$

Eliminating ς from equation (C-3) and (C-4), we have the linearized free surface condition

$$\varphi_{tt}+U^2\varphi_{xx}-2U\varphi_{xt}+g\varphi_z=\frac{1}{\rho}(Up_x-p_t), \qquad z=0,t>0 \tag{C-5}$$

In addition to the foregoing, φ and φ_t satisfy the condition being initially at rest on the free surface

$$\varphi(x,y,0;0)=\varphi_t(x,y,0;0)=0 \tag{C-6}$$

where $\varphi_t=0$ is valid under the assumption $p(x,y,0;0)=0$, and on the bottom

$$\varphi_z=0, \qquad z=-\infty,t>0 \tag{C-7}$$

In the far field, we suppose that φ and its first and second derivates tend to zero for any given time; in fact, they tend to zero in such a way that Fourier transforms exist.

We seek the form of φ which satisfies the foregoing conditions by employing the Fourier transform technique. Define the double Fourier transforms:

$$\bar{\varphi}(w,u,z;t) = \frac{1}{2\pi}\int_{-\infty}^{\infty}\int_{-\infty}^{\infty}\varphi(x,y,z;t)e^{-i(wx+uy)}dxdy \tag{C-8}$$

and the inversion

$$\varphi(x,y,z;t) = \frac{1}{2\pi}\int_{-\infty}^{\infty}\int_{-\infty}^{\infty}\bar{\varphi}(w,u,z;t)e^{i(wx+uy)}dwdu \tag{C-9}$$

Here w and u are the longitudinal and transverse wave numbers and are related to the circular wave number k and the wave angle θ by

$$\begin{aligned} w &= k\cos\theta \\ u &= k\sin\theta \end{aligned} \tag{C-10}$$

The Fourier transform (C-8) applied to (C-2) yields

$$\bar{\varphi}_{zz} - k^2\bar{\varphi} = 0 \tag{C-11}$$

The general solution of the foregoing differential equation is

$$\bar{\varphi} = A(w,u;t)e^{|k|z} + B(w,u;t)e^{-|k|z} \tag{C-12}$$

where A and B are arbitrary constants. By making use of the Fourier transform of the bottom condition (C-7), we obtain $B = 0$. Hence the preceding is reduced to

$$\bar{\varphi} = A(w,u;t)e^{|k|z} \tag{C-13}$$

To determine A, take the Fourier transform of the linearized free surface condition (C-5),

$$\bar{\varphi}_{tt} - U^2w^2\bar{\varphi} - i2Uw\bar{\varphi}_t + g\bar{\varphi}_z = i(Uw-\sigma)\frac{\bar{\Pi}}{\rho}e^{i\sigma t} \tag{C-14}$$

where

$$\bar{\Pi}(w,u) = \frac{1}{2\pi}\int_{-\infty}^{\infty}\int_{-\infty}^{\infty}\Pi(x,y)e^{-i(wx+uy)}dxdy = \frac{1}{2\pi}\int_{-b}^{b}d\eta\int_{-a}^{a}\Pi(\xi,\eta)e^{-i(w\xi+u\eta)}d\xi \tag{C-15}$$

Substituting $\bar{\varphi}$ from (C-13) in (C-14) yields

$$A_{tt} - U^2w^2A - i2UwA_t + g|k|A = i(Uw-\sigma)\frac{\bar{\Pi}}{\rho}e^{i\sigma t} \tag{C-16}$$

which by means of the Laplace transform and utilizing the initial condition

$$A(w,u;0) = A_t(w,u;0) = 0$$

yields the following solution in the transform plane

$$L\{A\} = \frac{(Uw-\sigma)\bar{\Pi}}{2\rho\sqrt{g|k|}}\left(\frac{1}{q-q_1} - \frac{1}{q-q_2}\right)L\{e^{i\sigma t}\}$$

with

$$\begin{aligned} q_1 &= i(Uw + \sqrt{g|k|}) \\ q_2 &= i(Uw - \sqrt{g|k|}) \end{aligned}$$

Inversion of the preceding is given by the convolution integral

$$A=\sum_{l=\pm1}\frac{l\overline{\Pi}(Uw-\sigma)}{2\rho\sqrt{g|k|}}\times\int_0^t e^{i\sigma\tau}e^{i(l\sqrt{g|k|}+Uw)(t-\tau)}d\tau \tag{C-17}$$

(C-17) after integration is substituted in (C-13) and we have

$$\overline{\varphi}=e^{i\sigma t}\sum_{l=\pm1}\frac{il\overline{\Pi}(Uw-\sigma)}{2\rho\sqrt{g|k|}}\cdot e^{|k|z}\frac{[1-e^{i(Uw+l\sqrt{g|k|}-\sigma)t}]}{Uw+l\sqrt{g|k|}-\sigma} \tag{C-18}$$

The inverse transform of (C-18) is given by

$$\varphi=e^{i\sigma t}\frac{i}{8\pi^2\rho}\int_{-b}^{b}d\eta\int_{-a}^{a}d\xi\ \Pi(\xi,\eta)\int_{-\infty}^{\infty}\int_{-\infty}^{\infty}\frac{1}{\sqrt{g|k|}}e^{|k|z+i(wx_0+uy_0)}(Uw-\sigma)\left(\frac{1-e^{i(Uw+\sqrt{g|k|}-\sigma)t}}{Uw+\sqrt{g|k|}-\sigma}-\frac{1-e^{i(Uw-\sqrt{g|k|}-\sigma)t}}{Uw-\sqrt{g|k|}-\sigma}\right)dwdu \tag{C-19}$$

where

$$\begin{aligned}x_0&=x-\xi\\ y_0&=y-\eta\end{aligned} \tag{C-20}$$

Now the variables (w,u) are transformed into (k,θ) by the relation (C-10). Replacing the elementary area:

$$dwdu=kd\theta dk$$

for the intervals $0\le k\le\infty,-\pi\le\theta\le\pi$, we have

$$\begin{aligned}\varphi=&e^{i\sigma t}\frac{i}{8\pi^2\rho}\int_{-b}^{b}d\eta\int_{-a}^{a}d\xi\ \Pi(\xi,\eta)\cdot\\ &\cdot\int_{-\pi}^{\pi}d\theta\int_0^\infty dk\sqrt{\frac{k}{g}}(Uk\cos\theta-\sigma)e^{kz+ik(x_0\cos\theta+y_0\sin\theta)}\left(\frac{1-e^{i(Uk\cos\theta+\sqrt{gk}-\sigma)t}}{Uk\cos\theta+\sqrt{gk}-\sigma}-\frac{1-e^{i(Uk\cos\theta-\sqrt{gk}-\sigma)t}}{Uk\cos\theta-\sqrt{gk}-\sigma}\right)\end{aligned} \tag{C-21}$$

To fold up the integration interval ($-\pi,\pi$) to ($0,\pi/2$), the integral over ($-\pi,\pi$) is subdivided into four quadrants

$$\int_{-\pi}^{\pi}=\int_{-\pi}^{-\pi/2}+\int_{-\pi/2}^{0}+\int_{0}^{\pi/2}+\int_{\pi/2}^{\pi}$$

and each integral is transformed into ($0,\pi/2$), we have the following

$$\begin{aligned}\varphi=&e^{i\sigma t}\frac{i}{8\pi^2\rho}\int_{-b}^{b}d\eta\int_{-a}^{a}d\xi\Pi(\xi,\eta)\int_0^{\pi/2}d\theta\int_0^\infty dk\sqrt{\frac{k}{g}}e^{kz}\cdot\\ &\left\{(Uk\cos\theta-\sigma)(e^{ikr_1}+e^{ikr_2})\left(\frac{1-e^{i\omega_1 t}}{\omega_1}-\frac{1-e^{i\omega_2 t}}{\omega_2}\right)+(Uk\cos\theta+\sigma)(e^{-ikr_1}+e^{-ikr_2})\left(-\frac{1-e^{-i\omega_3 t}}{\omega_3}+\frac{1-e^{-i\omega_4 t}}{\omega_4}\right)\right\}\end{aligned} \tag{C-22}$$

where

$$\begin{aligned}r_1&=(x-\xi)\cos\theta+(y-\eta)\sin\theta\\ r_2&=(x-\xi)\cos\theta-(y-\eta)\sin\theta\end{aligned} \tag{C-23}$$

and

$$\begin{cases}\omega_1 \\ \omega_2\end{cases} = Uk\cos\theta \pm \sqrt{gk} - \sigma$$
$$\begin{cases}\omega_3 \\ \omega_4\end{cases} = Uk\cos\theta \pm \sqrt{gk} + \sigma \tag{C-24}$$

In (C-22), φ is the solution of the unsteady conditions which have been stated at the outset. The next step is to derive the steady-state solution from (C-22) by eliminating the time-dependent terms. This is achieved in the following manner:

a). Determine the wave numbers k_i from $\omega_i = 0$;

b). take the proper indenting paths in the neighbourhood of k_i in the $k-$plane in order to have the exponentials vanish in time as $t \to \infty$.

The integration paths determined as such are therefore not arbitrary but strictly bound to derivation of the steady solution and to the root k_i.

Solving for zeros of ω_i in (C-24), namely, k_i, we have

$$\left.\begin{matrix}k_1 \\ k_2\end{matrix}\right\} = \frac{1}{2}k_0\sec^2\theta[1+2\tau\cos\theta \mp \sqrt{1+4\tau\cos\theta}] \tag{C-25a}$$

$$\left.\begin{matrix}k_3 \\ k_4\end{matrix}\right\} = \frac{1}{2}k_0\sec^2\theta[1-2\tau\cos\theta \mp \sqrt{1-4\tau\cos\theta}] \tag{C-25b}$$

with

$$k_0 = \frac{g}{U^2}, \qquad \tau = \frac{U\sigma}{g} \tag{C-25c}$$

It is seen from (C-25a) that k_1 and k_2 are positive real and $k_1 < k_2$ for interval $0 \le \theta \le \pi/2$. It is seen from (C-25b) that k_3 and k_4 are positive and real and $k_3 < k_4$ if

$$1-4\tau\cos\theta \ge 0$$

and k_3 and k_4 are complex with $\mathrm{Im}(k_3) < 0$ and $\mathrm{Im}(k_4) > 0$ if

$$1-4\tau\cos\theta \le 0$$

In other words, k_3 and k_4 are positive real in

$$\theta_c \le \theta \le \pi/2 \tag{C-26}$$

and complex in the interval

$$0 \le \theta \le \theta_c \tag{C-27}$$

where

$$\theta_c = \cos^{-1}\left(\frac{1}{4\tau}\right) \tag{C-28}$$

Now we consider the integrals with respect to k in the $k-$plane. $\omega_i, i=1,2,3,4$, in (C-24) are expanded at k_i:

$$i\omega_1 = i(Uk\cos\theta + \sqrt{gk} - \sigma) \approx +i(k-k_1)\frac{\sqrt{g}\sqrt{1+4\tau\cos\theta}}{2\sqrt{k_1}} \tag{C-29}$$

$$i\omega_2 = i(Uk\cos\theta - \sqrt{gk} - \sigma) \approx +i(k-k_2)\frac{\sqrt{g}\sqrt{1+4\tau\cos\theta}}{2\sqrt{k_2}} \tag{C-30}$$

$$-i\omega_3 = -i(Uk\cos\theta + \sqrt{gk} + \sigma) \approx +i(k-k_3)\frac{\sqrt{g}\sqrt{1-4\tau\cos\theta}}{2\sqrt{k_3}} \tag{C-31}$$

$$-i\omega_4 = -i(Uk\cos\theta - \sqrt{gk} + \sigma) \approx -i(k-k_4)\frac{\sqrt{g}\sqrt{1-4\tau\cos\theta}}{2\sqrt{k_4}} \tag{C-32}$$

Equation (C-29) shows that, for interval $0 \le \theta \le \pi/2$, the path of integration of the terms containing $e^{i\omega_1 t}$ in (C-22) in the complex $k-$plane should be deformed above the real axis in the neighbourhood of k_1 in order to have the exponentials in t vanish as $t \to \infty$ ($\mathrm{Re}\{i\omega_1\} < 0$). The same is for k_2. Let this deformed path be defined by L_1 (see Figure C-1). When k_3 and k_4 are real (for $\theta_c \le \theta \le \pi/2$), the integral path is L_2 and for case of k_3 and k_4 are complex (for $0 < \theta < \theta_c$), the integration path requires no deformation in order to have the exponentials in t vanish as $t \to \infty$, the integral path is L_3 as shown in Figure C-1.

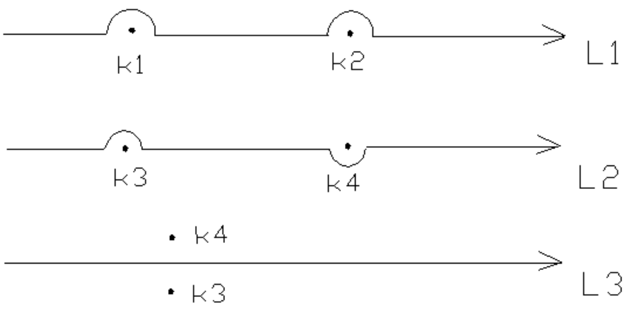

Figure C-1 The integral path

Then the steady-state velocity potential (omitting the time factor $e^{i\sigma t}$) is obtained as

$$\varphi = \frac{i}{4\pi^2\rho U^2}\int_{-b}^{b} d\eta \int_{-a}^{a} d\xi \Pi(\xi,\eta)\left\{-\int_{0}^{\pi/2} d\theta \sec^2\theta \int_{0,L_1}^{\infty} dk \Xi_1(\theta,k) + \int_{\theta_c}^{\pi/2} d\theta \sec^2\theta \int_{0,L_2}^{\infty} dk \Xi_2(\theta,k) + \int_{0}^{\theta_c} d\theta \sec^2\theta \int_{0,L_3}^{\infty} dk \Xi_2(\theta,k)\right\} \tag{C-32}$$

where

$$\begin{aligned}\Xi_1(\theta,k) &= (Uk\cos\theta-\sigma)(e^{k(z+ir_1)}+e^{k(z+ir_2)})\frac{1}{k_1-k_2}\left(\frac{k_1}{k-k_1}-\frac{k_2}{k-k_2}\right)\\ \Xi_2(\theta,k) &= (Uk\cos\theta+\sigma)(e^{k(z-ir_1)}+e^{k(z-ir_2)})\frac{1}{k_3-k_4}\left(\frac{k_3}{k-k_3}-\frac{k_4}{k-k_4}\right)\end{aligned} \qquad \text{(C-33)}$$

The free surface elevation at a point on the calm water surface, $z=0$, is evaluated for a uniform pressure distribution of a rectangular shape by

$$\varsigma = -\frac{\Pi}{\rho g}+\frac{U}{g}\varphi_z-\frac{i\sigma}{g}\varphi \qquad z=0 \qquad \text{(C-34)}$$

where the first term is the static elevation while the reminder represents the elevation due to the dynamic effect, and is expressed as

$$\begin{aligned}\frac{\rho g\varsigma}{\Pi} = -\frac{1}{4\pi^2U^2}&\left\{\int_0^{\pi/2} d\theta\frac{\sec^3\theta}{\sin\theta}\left\{\frac{\sigma^2}{k_1k_2}(\mathrm{I}_1)+\sum_{l=1}^{2}(-1)^{l+1}\frac{(Uk_l\cos\theta-\sigma)^2}{k_l(k_1-k_2)}[\mathrm{I}_2(k_l)]\right\}\right.\\ &+\int_{\theta_c}^{\pi/2} d\theta\frac{\sec^3\theta}{\sin\theta}\left\{\frac{\sigma^2}{k_3k_4}(\mathrm{I}_1^*)+\sum_{l=3}^{4}(-1)^{l+1}\frac{(Uk_l\cos\theta+\sigma)^2}{k_l(k_3-k_4)}[\mathrm{I}_4(k_l)]\right\}\\ &\left.+\int_0^{\theta_c} d\theta\frac{\sec^3\theta}{\sin\theta}\left\{\frac{\sigma^2}{k_3k_4}(\mathrm{I}_1^*)+\sum_{l=3}^{4}(-1)^{l+1}\frac{(Uk_l\cos\theta+\sigma)^2}{k_l(k_3-k_4)}[\mathrm{I}_{2+l}(k_l)]\right\}\right\}\end{aligned} \qquad \text{(C-35)}$$

where $*$ indicates the complex conjugate, and

$$\mathrm{I}_1(s_m)=\int_0^\infty dk\frac{e^{kz}(e^{iks_1}-e^{iks_2}+e^{iks_3}-e^{iks_4}+e^{iks_5}-e^{iks_6}+e^{iks_7}-e^{iks_8})}{k} \qquad \text{(C-36)}$$

$$\mathrm{I}_2(k_j)=\int_{0,\text{above } k_j}^{\infty} dk\frac{e^{kz}(e^{iks_1}-e^{iks_2}+e^{iks_3}-e^{iks_4}+e^{iks_5}-e^{iks_6}+e^{iks_7}-e^{iks_8})}{k-k_j} \qquad j=1,2 \qquad \text{(C-37)}$$

$$\mathrm{I}_4(k_3)=\int_{0,\text{above } k_3}^{\infty} dk\frac{e^{kz}(e^{-iks_1}-e^{-iks_2}+e^{-iks_3}-e^{-iks_4}+e^{-iks_5}-e^{-iks_6}+e^{-iks_7}-e^{-iks_8})}{k-k_3} \qquad k_3 \text{ positive real} \qquad \text{(C-38)}$$

$$\mathrm{I}_4(k_4)=\int_{0,\text{below } k_4}^{\infty} dk\frac{e^{kz}(e^{-iks_1}-e^{-iks_2}+e^{-iks_3}-e^{-iks_4}+e^{-iks_5}-e^{-iks_6}+e^{-iks_7}-e^{-iks_8})}{k-k_4} \qquad k_4 \text{ positive real} \qquad \text{(C-39)}$$

$$\mathrm{I}_5(k_3)=\int_0^\infty dk\frac{e^{kz}(e^{-iks_1}-e^{-iks_2}+e^{-iks_3}-e^{-iks_4}+e^{-iks_5}-e^{-iks_6}+e^{-iks_7}-e^{-iks_8})}{k-k_3} \qquad k_3 \text{ complex} \qquad \text{(C-40)}$$

$$\mathrm{I}_6(k_4)=\int_0^\infty dk\frac{e^{kz}(e^{-iks_1}-e^{-iks_2}+e^{-iks_3}-e^{-iks_4}+e^{-iks_5}-e^{-iks_6}+e^{-iks_7}-e^{-iks_8})}{k-k_4} \qquad k_4 \text{ complex} \qquad \text{(C-41)}$$

Integrals in (C-36) ~ (C-41) can be analysed as follows. First, we consider integral

$$I_1(s_m)=\int_0^\infty\frac{e^{iks_m}}{k}dk \qquad \text{(C-42)}$$

When $s_m>0$, consider an integral for the closed path in the $k-$plane: $L=L_1+L_2+L_3+L_4$, as shown in Figure C-2. L_2 is a quarter of a cycle with radium of R, and L_4 is a quarter of a cycle with radius of ε. Since there is no pole inside the closed path, the integral along this closed path is zero:

$$\int_{L_1} \frac{e^{iks_m}}{k} dk + \int_{L_2} \frac{e^{iks_m}}{k} dk + \int_{L_3} \frac{e^{iks_m}}{k} dk + \int_{L_4} \frac{e^{iks_m}}{k} dk = \oint_{L} \frac{e^{iks_m}}{k} dk = 0 \qquad \text{(C-43)}$$

Then

$$J_1 = \int_{L_1} \frac{e^{iks_m}}{k} dk = \int_{\varepsilon}^{R} \frac{e^{iks_m}}{k} dk = \int_{0}^{\infty} \frac{e^{iks_m}}{k} dk \qquad \text{as } \varepsilon \to 0;\ R \to \infty \qquad \text{(C-44)}$$

$$J_2 = \int_{L_2} \frac{e^{iks_m}}{k} dk \overset{k=Re^{i\theta}}{=} \int_{0}^{\pi/2} \frac{e^{i(R\cos\theta + iR\sin\theta)s_m}}{R\, e^{i\theta}} \cdot i \cdot R \cdot e^{i\theta} d\theta = i \int_{0}^{\pi/2} e^{-Rs_m \sin\theta} \cdot e^{iRs_m \cos\theta} d\theta \qquad \text{(C-45)}$$

therefore

$$\left|J_2\right| \le \int_{0}^{\pi/2} e^{-Rs_m \sin\theta} \left|e^{iRs_m \cos\theta}\right| d\theta \le \int_{0}^{\pi/2} e^{-Rs_m \sin\theta} d\theta \overset{t=\tan(\theta/2)}{=} \int_{0}^{1} e^{-\frac{2Rs_m t}{1+t^2}} \frac{2dt}{1+t^2}$$

$$\le 2\int_{0}^{1} e^{-\frac{2Rs_m t}{1+t^2}} dt \le 2\int_{0}^{1} e^{-2Rs_m t} dt = \frac{1}{R\, s_m}\left(1 - e^{-2Rs_m}\right) \to 0 \qquad \text{as } R \to \infty \qquad \text{(C-46)}$$

thus

$$J_2 \to 0 \qquad \text{as } R \to \infty \qquad \text{(C-47)}$$

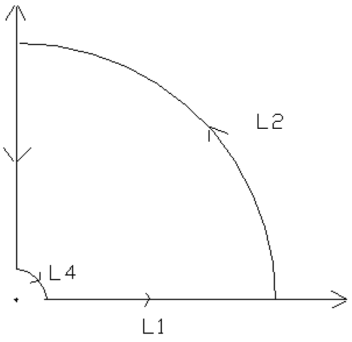

Figure C-2 Integral path for $I_1(s_m)$ in the $k-$plane ($s_m > 0$)

$$J_3 = \int_{L_3} \frac{e^{iks_m}}{k} dk = \int_{\infty}^{\varepsilon} \frac{e^{-ys_m}}{iy} \cdot i \cdot dy = -\int_{\varepsilon}^{\infty} \frac{e^{-ys_m}}{y} dy \qquad \text{(C-48)}$$

$$\frac{dJ_3}{ds_m} = \int_{\varepsilon}^{\infty} e^{-ys_m} dy = -\frac{1}{s_m} e^{-ys_m}\Big|_{\varepsilon}^{\infty} = \frac{e^{-\varepsilon s_m}}{s_m} \qquad \text{(C-49)}$$

So that

$$J_3 = \ln(s_m) \qquad \text{as } \varepsilon \to 0 \qquad \text{(C-50)}$$

On the other hand

$$J_4 = \int_{L_4} \frac{e^{iks_m}}{k} dk \overset{k=\varepsilon e^{i\theta}}{=} \int_{\pi/2}^{0} \frac{e^{iks_m}}{\varepsilon e^{i\theta}} i\varepsilon e^{i\theta} d\theta = i \int_{\pi/2}^{0} e^{iks_m} d\theta$$

$$= i \int_{\pi/2}^{0} \left[1 + iks_m + \frac{(iks_m)^2}{2!} + \ldots \right] d\theta$$

$$= i \int_{\pi/2}^{0} \left[1 + i\varepsilon e^{i\theta} s_m + \frac{(i\varepsilon e^{i\theta} s_m)^2}{2!} + \ldots \right] d\theta$$

$$= -\frac{i\pi}{2} \qquad \text{as } \varepsilon \to 0 \tag{C-51}$$

Substituting (C-47), (C-50) and (C-51) into (C-43), one obtains

$$I_1(s_m) = \int_0^\infty \frac{e^{iks_m}}{k} dk = -J_2 - J_3 - J_4 = -\ln(s_m) + \frac{i\pi}{2} \tag{C-52}$$

For $s_m < 0$, the integral path in the $k-$plane is on the 4th quarter, as shown in Figure C-3.

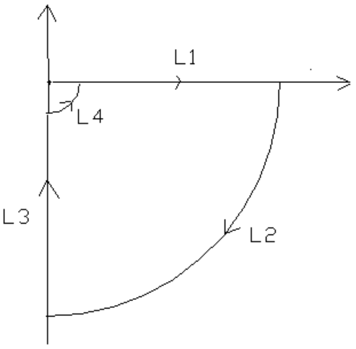

Figure C-3 Integral path for $I_1(s_m)$ in the $k-$plane ($s_m < 0$)

Follow the same procedure as for $s_m > 0$, we obtain

$$I_1(s_m) = \int_0^\infty \frac{e^{iks_m}}{k} dk = -J_2 - J_3 - J_4 = -\ln(|s_m|) - \frac{i\pi}{2} \tag{C-53}$$

or

$$I_1(s_m) = \int_0^\infty \frac{e^{iks_m}}{k} dk = -\ln(|s_m|) + \text{sgn}(s_m)\frac{i\pi}{2} \tag{C-54}$$

We then consider integral

$$I_2(k_j) = \int_0^\infty \frac{e^{iks_m}}{k - k_j} dk \qquad j = 1,2;\ m = 1,2,...,8 \tag{C-55}$$

For $s_m > 0$, we consider integral along the closed path as shown in Figure C-4. Since there is no pole inside the path:

$$\int_{L_1}\frac{e^{iks_m}}{k-k_j}dk+\int_{L_2}\frac{e^{iks_m}}{k-k_j}dk+\int_{L_3}\frac{e^{iks_m}}{k-k_j}dk=\oint_{L}\frac{e^{iks_m}}{k-k_j}dk=0 \tag{C-56}$$

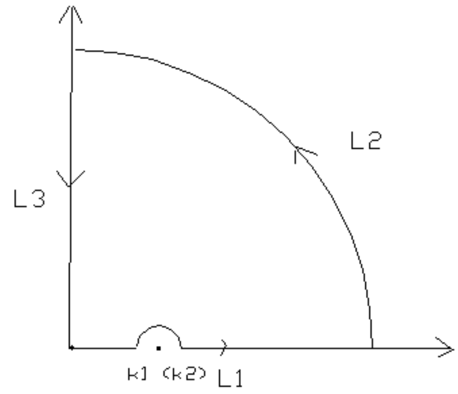

Figure C-4 Integral path for $I_2(k_j), j=1,2$ in the $k-$plane ($s_m>0$)

Integral over L_2 is calculated as follows.

$$J_2=\int_{L_2}\frac{e^{iks_m}}{k-k_j}dk=\int_0^{\pi/2}\frac{e^{-Rs_m\sin\theta}}{R\,e^{i\theta}-k_j}\cdot e^{iRs_m\cos\theta}\cdot i\cdot R\cdot e^{i\theta}d\theta$$

$$|J_2|\le\frac{R}{R-k_j}\int_0^{\pi/2}e^{-Rs_m\sin\theta}d\theta\overset{t=\tan(\theta/2)}{=}\frac{R}{R-k_j}\int_0^1\exp\{-\frac{2tRs_m}{1+t^2}\}\frac{2dt}{1+t^2}$$

$$\le\frac{2R}{R-k_j}\int_0^1 e^{-2tRs_m}dt=\frac{1}{R-k_j}(e^{-2Rs_m}-1)\to 0 \qquad \text{as } R\to\infty \tag{C-57}$$

therefore

$$J_2\to 0 \qquad \text{as } R\to\infty \tag{C-58}$$

On the other hand;

$$J_3=\int_{L_3}\frac{e^{iks_m}}{k-k_j}dk=\int_{\infty}^{0}\frac{e^{-ys_m}}{iy-k_j}\cdot i\cdot dy=-\int_0^{\infty}\frac{e^{-ys_m}}{y+ik_j}dy=-\int_0^{\infty}\frac{e^{-ys_m}}{ys_m+ik_js_m}d(ys_m)$$

$$=-\int_0^{\infty}\frac{e^{-(t+ik_js_m)}\cdot e^{ik_js_m}}{t+ik_js_m}dt=-e^{ik_js_m}E_1(ik_js_m) \tag{C-59}$$

Substituting (C-58) and (C-59) into (C-56), then

$$I_2(k_j)=E_1(ik_js_m)e^{ik_js_m} \tag{C-60}$$

For $s_m<0$, the integral path takes the form as shown in Figure C-5. There is a pole inside the closed path, according to residues theorem,

$$\int_{L_1}\frac{e^{iks_m}}{k-k_j}dk+\int_{L_2}\frac{e^{iks_m}}{k-k_j}dk+\int_{L_3}\frac{e^{iks_m}}{k-k_j}dk=\oint_{L}\frac{e^{iks_m}}{k-k_j}dk=-2\pi i\cdot e^{ik_js_m} \tag{C-61}$$

The procedures for analysing integrals over L_2 and L_3 are similar for these of the case of $s_m > 0$, then we obtain:

$$I_2(k_j) = E_1(ik_j s_m)e^{ik_j s_m} - 2\pi i e^{ik_j s_m} \tag{C-62}$$

or

$$I_2(k_j) = \int_0^{\infty} \frac{e^{iks_m}}{k - k_j} dk = e^{ik_j s_m}[E_1(ik_j s_m) - i\pi(1 - \mathrm{sgn}(s_m))] \qquad j = 1,2 \tag{C-63}$$

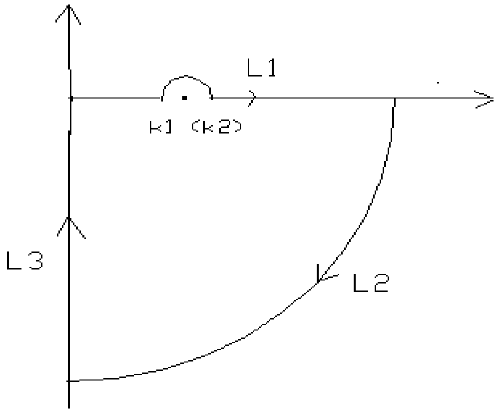

Figure C-5 Integral path for $I_2(k_j), j = 1,2$ in the $k-$plane ($s_m < 0$)

Similarly, one can get the following integrals ($\theta_c < \theta < \pi/2$):

$$I_4(k_3) = \int_0^{\infty} \frac{e^{-iks_m}}{k - k_3} dk = e^{-ik_3 s_m}[E_1(-ik_3 s_m) - i\pi(1 + \mathrm{sgn}(s_m))] \tag{C-64}$$

$$I_4(k_4) = \int_0^{\infty} \frac{e^{-iks_m}}{k - k_4} dk = e^{-ik_4 s_m}[E_1(-ik_4 s_m) + i\pi(1 - \mathrm{sgn}(s_m))] \tag{C-65}$$

When k_3 and k_4 are complex ($0 < \theta < \theta_c$),

$$I_5(k_3) = \int_0^{\infty} \frac{e^{-iks_m}}{k - k_3} dk = e^{-ik_3 s_m}[E_1(-ik_3 s_m) - 0.5\pi i(1 + \mathrm{sgn}(s_m))(1 + \mathrm{sgn}(\mathrm{Re}(k_3)))] \tag{C-66}$$

$$I_6(k_4) = \int_0^{\infty} \frac{e^{-iks_m}}{k - k_4} dk = e^{-ik_4 s_m}[E_1(-ik_4 s_m) + 0.5\pi i(1 - \mathrm{sgn}(s_m))(1 + \mathrm{sgn}(\mathrm{Re}(k_4)))] \tag{C-67}$$

With all the individual integrals, the following can be obtained:

$$\mathrm{I}_1 = \sum_{m=1}^{8} (-1)^m \left[\ln|s_m| - 0.5\pi\,\mathrm{sgn}(s_m)\right] \tag{C-68}$$

$$\mathrm{I}_2(k_l) = \sum_{m=1}^{8} (-1)^{m+1} e^{ik_l s_m} \left[E_1(ik_l s_m) - i\pi(1 - \mathrm{sgn}(s_m))\right] \qquad l = 1,2 \tag{C-69}$$

$$\mathrm{I}_4(k_3) = \sum_{m=1}^{8} (-1)^{m+1} e^{-ik_3 s_m} \left[E_1(-ik_3 s_m) - i\pi(1 + \mathrm{sgn}(s_m))\right] \tag{C-70}$$

$$\mathrm{I}_4(k_4)=\sum_{m=1}^{8}(-1)^{m+1}e^{-ik_4s_m}\left[E_1(-ik_4s_m)+i\pi(1-\operatorname{sgn}(s_m))\right] \tag{C-71}$$

$$\mathrm{I}_5(k_3)=\begin{cases}\displaystyle\sum_{m=1}^{8}(-1)^{m+1}e^{-ik_3s_m}\left[E_1(-ik_3s_m)-i\pi(1+\operatorname{sgn}(s_m))\right] & \mathrm{Re}(k_3)>0\\ \displaystyle\sum_{m=1}^{8}(-1)^{m+1}e^{-ik_3s_m}\left[E_1(-ik_3s_m)\right] & \mathrm{Re}(k_3)<0\end{cases} \tag{C-72}$$

$$\mathrm{I}_6(k_4)=\begin{cases}\displaystyle\sum_{m=1}^{8}(-1)^{m+1}e^{-ik_4s_m}\left[E_1(-ik_4s_m)+i\pi(1-\operatorname{sgn}(s_m))\right] & \mathrm{Re}(k_4)>0\\ \displaystyle\sum_{m=1}^{8}(-1)^{m+1}e^{-ik_4s_m}\left[E_1(-ik_4s_m)\right] & \mathrm{Re}(k_4)<0\end{cases} \tag{C-73}$$

Substituting (C-68) ~ (C-73) into (C-35), we obtain

$$\frac{\rho g\varsigma}{\Pi}=-\frac{1}{4\pi^2}\sum_{m=1}^{8}(-1)^m\left(J_{0m}+J_{1m}+J_{2m}+J_{3m}+J_{4m}+J_{5m}+J_{6m}\right) \tag{C-74}$$

where $J_{l,m}, l=0,1,...,6; m=1,2,...,8$, are shown in equations (9.14) ~ (9.20) in Chapter 9.

As a special case, consider the wave elevation due to a uniformly moving non-oscillatory pressure distribution. Then according to (C-25), we have

$$\begin{aligned}&\tau=0,\quad k_1=k_3=0\\&k_2=k_4=k_0\sec^2\theta\end{aligned} \tag{C-75}$$

The free surface elevation (C-35) is reduced to

$$\frac{\rho g\varsigma_s}{\Pi}=-\frac{1}{2\pi^2}\sum_{m=1}^{8}(-1)^{m+1}\,\mathrm{Re}\left\{\int_0^{\pi/2}\frac{\exp[ik_0\sec^2\theta s_m]}{\sin\theta\cos\theta}[E_1(ik_0\sec^2\theta s_m)-i\pi(1-\operatorname{sgn}(s_m))]\right\} \tag{C-76}$$

which is equation (6.9) in Chapter 6.